

## ABSTRACT

TRANSPORTATION ANALYSIS AND RELATED DESIGN OPTIMIZATION OF THE  
FERMILAB HIGH-BETA 650 MHZ CRYOMODULE

Joshua F. Helsper, M.S.  
Department of Mechanical Engineering  
Northern Illinois University, 2020  
Dr. Iman Salehinia, Director

The Proton Improvement Plan-II (PIP-II) at Fermi National Accelerator Laboratory (FNAL) will create a new and vastly improved accelerator, which will be the source of high-energy particles for the experiments taking place at FNAL. The new linear accelerator (LINAC) contains several types of cryomodules, which are individual particle accelerators. The last cryomodule in the LINAC will be the High-Beta 650 (HB650), which will operate at 650 MHz. Each module is approximately 15 meters in length and 1.5 meters wide, weighs 13 tonnes, and shares many design features with three of the other cryomodules.

The HB650 consists of two primary sections, the outer vacuum vessel and the components that reside within it, which will be cooled to cryogenic temperatures – the cold mass. Once assembly is complete at FNAL, it will be transported to one of three places: another location at FNAL, another national laboratory within the continental United States, or to a scientific partner in Europe. Any excitation the module experiences, such as going over rough roads when on a semi-trailer, can create high stresses in components and cause failure if severe enough. Additionally, any delicate components with low resonant frequencies that match the excitation spectrum could

achieve resonance, potentially causing a fatigue failure by repeated flexing. To ensure the successful transportation of the HB650, a transport analysis utilizing ANSYS simulation software has been performed on major subassemblies, as well as analysis of the subassemblies as a combined system. The optimization of components, design of support structures, and overall increasing of the lowest resonant frequencies have resulted in a cryomodule that will be better equipped to handle transportation and any large impact loads that come with it.

NORTHERN ILLINOIS UNIVERSITY

DEKALB, ILLINOIS

DECEMBER 2020

TRANSPORTATION ANALYSIS AND RELATED DESIGN OPTIMIZATION OF THE  
FERMILAB HIGH-BETA 650 MHZ CRYOMODULE

BY

JOSHUA F. HELSPER

©2020 Joshua F. Helsper

A THESIS SUBMITTED TO THE GRADUATE SCHOOL  
IN PARTIAL FULFILLMENT OF THE REQUIREMENTS  
FOR THE DEGREE  
MASTER OF SCIENCE

DEPARTMENT OF MECHANICAL ENGINEERING

Thesis Director:

Iman Salehinia

## **ACKNOWLEDGEMENTS**

I would like to thank Fermilab National Accelerator Laboratory for partnering with Northern Illinois University on the design of the HB650 cryomodule, specifically Dr. Genfa Wu and Dr. Iman Salehinia, who worked out the agreement. Several engineers at Fermilab have made a significant impact on me, and it was their guidance that has allowed me to progress as an engineer and learn more than any class has taught me. Vincent Roger, Dr. Sergey Cheban, and Dr. Jeremiah Holzbauer, I consider you each a mentor, and I am grateful to each of you for the different skills you have taught me. Fellow NIU students Gerald Smith, Ryan Lewis, and Jason Ostenburg, your input on my thesis has been quite valuable. To my grandparents, Gerald and Susan Helsper, I thank you for your financial support during the pursuit of my advanced degree. And finally, I would like to thank Dr. Iman Salehinia, my advisor, and Dr. Nicholas Pohlman and Dr. Sachit Butail, who served on the committee. As my advisor, Dr. Salehinia has taught me to question everything and that the underlying mechanisms of a problem can only be understood through intense scrutiny. To everyone who has helped me along this journey, thank you.

# TABLE OF CONTENTS

	Page
LIST OF TABLES .....	v
LIST OF FIGURES .....	vi
LIST OF APPENDICES .....	xiii
DEPARTMENT OF ENERGY ACKNOWLEDGEMENT, COPYRIGHT STATEMENT, AND DISCLAIMER .....	xiv
1. INTRODUCTION .....	1
1.1 PIP-II Project.....	2
1.2 The HB650 Cryomodule .....	3
1.3 Problem Statement .....	6
1.4 Background .....	6
1.4.1 Previous Transportation Studies .....	6
1.4.2 Previous Transportation Analysis .....	10
1.4.3 Transportation Plan and Configuration.....	14
1.4.4 HB650 Subassemblies Design Overview .....	16
1.5 Design Requirements .....	32
1.6 Thesis Objectives .....	32
2. METHODS .....	34
2.1 Analysis Procedure.....	35
2.1.1 Geometry Inspection.....	35
2.1.2 Analytical Calculations .....	36
2.1.3 Geometry Simplification.....	39
2.1.4 Analysis and Design Revision .....	40
2.1.5 Combined Analysis.....	41
2.2 FEA Techniques.....	42
2.2.1 Mesh Generation.....	43

	Page
2.2.2 Connections.....	45
2.2.3 Modal Analysis.....	46
3. SUBSYSTEM ANALYSIS AND RESULTS .....	47
3.1 Coupler.....	47
3.2 Tuner .....	51
3.3 B90 Cavity.....	54
3.4 B92 Cavity.....	56
3.5 Cavity Supports.....	58
3.6 Two-Phase Pipe.....	66
3.7 Heat Exchanger .....	72
3.8 Cryogenic Lines .....	76
3.9 Pumping Line Support .....	81
3.10 Thermal Shield .....	84
3.11 Magnetic Shields .....	88
3.12 Strongback.....	92
3.13 Strongback Supports.....	94
3.14 Vessel.....	100
4. COMBINED SYSTEM RESULTS AND DISCUSSION.....	103
4.1 B90 Cavity String Section.....	103
4.2 B92 Cavity String Section.....	112
4.3 Cavity String .....	113
4.4 Vessel and Strongback .....	117
4.5 Full Cryomodule .....	119
5. RESULTS SUMMARY AND FUTURE WORK .....	123
REFERENCES .....	126
APPENDICES .....	129

## **LIST OF TABLES**

	Page
Table 1-1: Maximum Shocks at Internal Frame During Previous Cryomodule Transportations...	9
Table 1-2: Material Properties .....	17
Table 3-1: Needle Support Results Comparison.....	65
Table 3-2: Strongback Support Analytical Calculations Summary .....	95
Table 3-3: Simplified and Detailed Strongback Support Results Comparison.....	99
Table 4-1: Cryomodule Bellows Results .....	122
Table 5-1: Summary of Results .....	124

# LIST OF FIGURES

	Page
Figure 1.1: Diagram of Beamlines at Fermilab .....	1
Figure 1.2: SRF Cavity Proton Acceleration .....	2
Figure 1.3: Cryomodules in the LINAC .....	3
Figure 1.4: HB650 Cryomodule Exterior .....	4
Figure 1.5: HB650 Cross-Section View .....	5
Figure 1.6: DESY Transport Frame and Cryomodule .....	7
Figure 1.7: Example Transport Excitation Spectrum .....	8
Figure 1.8: Left: LCLS-II Transport Frame   Right: LCLS-II Cracked Bellows .....	10
Figure 1.9: EXFEL Coupler   Left: Modal Analysis   Right: Shaker Table Test .....	12
Figure 1.10: EXFEL   Left: Predicted Response   Right: Actual Response .....	12
Figure 1.11: SSR1 Cryomodule Analysis .....	13
Figure 1.12: HB650 Preliminary FE Model .....	14
Figure 1.13: HB650 Preliminary 5G Deformation Results .....	14
Figure 1.14: Transportation Frame .....	15
Figure 1.15: Intercavity Bellow .....	18
Figure 1.16: B90 Cavity Components .....	19
Figure 1.17: Cavity Jacket Mounting Interfaces.....	19
Figure 1.18: Section View of Cavity End.....	20
Figure 1.19: B92 Cavity Components .....	20
Figure 1.20: Tuner Components .....	21
Figure 1.21: Slow Tuner Mechanism.....	22
Figure 1.22: Coupler Components.....	23
Figure 1.23: Cavity Support Components .....	24
Figure 1.24: Needle Support Components.....	24

	Page
Figure 1.25: Cooling Lines   Yellow 50K   Blue 5 K   Red 2K.....	25
Figure 1.26: Pumping Line Support.....	26
Figure 1.27: Two-Phase Pipe Components.....	27
Figure 1.28: Heat Exchanger .....	27
Figure 1.29: Thermal Shield .....	28
Figure 1.30: Global and Local Magnetic Shields .....	29
Figure 1.31: Strongback.....	30
Figure 1.32: Cold Mass.....	30
Figure 1.33: Strongback Supports.....	30
Figure 1.34: Vacuum Vessel Components.....	31
Figure 2.1: Analysis Methods Pictural Representation.....	34
Figure 2.2: Methodology Flowchart .....	35
Figure 2.3: Cavity Lug Support   Left: Transverse Section View   Right: Axial Section View ...	36
Figure 2.4: Detailed Support Model   Left: Transverse Section View   Right: Axial Section View .....	40
Figure 2.5: Simplified Support Model   Left: Joint Connection   Right: Torsional Spring .....	40
Figure 2.6: Workbench™ Model Combination Methods .....	42
Figure 2.7: Final Bellows Mesh.....	44
Figure 2.8: Bellows Mesh Convergence Comparison .....	44
Figure 2.9: Solid-Shell Contact Comparison   Top: MPC   Bottom: Automatic .....	45
Figure 2.10: Left: Cooling Line Support   Right: Support Location.....	46
Figure 3.1: Coupler Mesh .....	47
Figure 3.2: Coupler Boundary Conditions.....	48
Figure 3.3: Coupler Mode Shape 37 Hz .....	49
Figure 3.4: Coupler 5G Stress.....	49
Figure 3.5: Connector Stress vs Axial Displacement .....	50
Figure 3.6: Coupler Simplified Mesh .....	51
Figure 3.7: Tuner Model   Left: Mesh   Right: Boundary Conditions .....	52
Figure 3.8: Tuner Mode Shapes   Left: 80 Hz Top View   Right: 117 Hz Side View .....	52

Figure 3.9: Tuner Structural Results   Left: Stress   Right: Total Deformation .....	53
Figure 3.10: Simplified Tuner Mesh.....	53
Figure 3.11: B90 Model   Left: Mesh   Center: Fixed Constraint   Right: Tuner Springs .....	54
Figure 3.12: B90 Mode Shapes, Section View from Above  Left: 73 Hz  Right: 121 Hz.....	55
Figure 3.13: B90 Cavity Structural Results  Left: Bellows Transverse Displacement 3G   Right: Niobium Cells Stress 5G.....	56
Figure 3.14: B92 Cavity Mesh Section View .....	56
Figure 3.15: B92 Mode Shapes, Section View  Left: 52 Hz  Right: 115Hz .....	57
Figure 3.16: B92 Cavity Structural Results   Left: Bellows Transverse Displacement 3G   Right: Niobium Cells Stress 3G.....	58
Figure 3.17: Cavity Support   Left: Mesh   Right: Boundary Conditions .....	59
Figure 3.18: Cavity Lug Support   Left: Transverse Section View   Right: Axial Section View .	60
Figure 3.19: Cavity Support 1.5G Slip Scenario .....	61
Figure 3.20: Detailed Needle Support Section Views and Contacts .....	62
Figure 3.21: Cavity Support Mode Shapes   Left: 20 Hz   Right: 21 Hz .....	63
Figure 3.22: Cavity Support 1.5G Stress   Left: No Sliding   Right: Sliding.....	63
Figure 3.23: Needle Support   Top: Unit Rotation   Bottom Left: Centered Lug   Bottom Right: Offset Lug .....	64
Figure 3.24: Simplified Support Model with Spring About X Axis.....	65
Figure 3.25: Needle Support 5G Stress Comparison .....	66
Figure 3.26: Two-Phase Pipe Mesh and Boundary Conditions.....	67
Figure 3.27: Two-Phase Pipe End Section Mesh.....	67
Figure 3.28: Helium Level Sensor   Left: Potential Failure Mode   Center: Contextual View   Right: Mode Shape .....	68
Figure 3.29: End Section Modes   Left: Downstream 13 Hz   Right: Upstream 16 Hz.....	69
Figure 3.30: End Section 3G Total Deformation.....	70
Figure 3.31: Center Section 3G Total Deformation.....	70
Figure 3.32: Helium Level Sensor Guide .....	71
Figure 3.33: Improved Design – End Section - 3G Total Deformation.....	72
Figure 3.34: Installation Tooling Used Before Invar Rods Can Support Bellows .....	72

Figure 3.35: Heat Exchanger Boundary Conditions and Mesh .....	73
Figure 3.36: Heat Exchanger   Left: 1.5G Stress   Center: 8 Hz Mode   Right: 12 Hz Mode.....	74
Figure 3.37: Heat Exchanger Support Components .....	75
Figure 3.38: Support Thermal Results   Left: Collar   Right: Standoff.....	75
Figure 3.39: Heat Exchanger Updated First Mode Shape .....	76
Figure 3.40: 2K Line Boundary Conditions .....	77
Figure 3.41: 2K Line   Left: Mesh   Right: Reference Image of CAD Model .....	77
Figure 3.42: 2K Line First Mode Shape 22 Hz.....	78
Figure 3.43: 2K Line 3G Results   Left: Fill Line Stress   Right: Total Deformation .....	78
Figure 3.44: 5K Line Boundary Conditions .....	79
Figure 3.45: 5K Line   Left: Mesh   Right: Reference Image Transport Supports .....	80
Figure 3.46: 5K Line 14 Hz Mode Shape .....	80
Figure 3.47: 5K Line 5G Results   Left: Deformation   Right: Stress.....	81
Figure 3.48: Pumping Line Support Mesh and Boundary Conditions.....	82
Figure 3.49: Pumping Line Support Results   Left: Mode Shape 27 Hz   Right: 5G Deformation .....	83
Figure 3.50: Pumping Line Support 5G Stress   Left: Rods Eq. Stress   Right: G10 Prin. Stress	84
Figure 3.51: Thermal Shield   Left: Mesh   Right: Frictionless Supports .....	84
Figure 3.52: Thermal Shield Boundary Conditions   Left: Cavity Support Conditions   Right: Transport Support .....	85
Figure 3.53: Thermal Shield Boundary Conditions   Left: Shield Guide Section View   Right: Distributed Mass .....	86
Figure 3.54: Left: Previous Attachment to the Support Post   Right: Updated Design .....	87
Figure 3.55: Thermal Shield First Mode Shape 23 Hz .....	87
Figure 3.56: Thermal Shield 3G Deformation.....	88
Figure 3.57: Thermal Shield Structural Results   Left: 3G Stress   Right: 5G Deformation .....	88
Figure 3.58: Global Magnetic Shield Center Section Mesh and Boundary Conditions .....	89
Figure 3.59: Global Magnetic Shield End Section Mesh and Boundary Conditions .....	90
Figure 3.60: Central Section First Mode Shape 33 Hz .....	90

Figure 3.61: Global Shield End Section | Left: 10 Hz Mode | Center: 5G Def. | Right: 5G Stress ..... 91

Figure 3.62: End Section Revised Design and 5G Results ..... 91

Figure 3.63: Strongback Mesh ..... 92

Figure 3.64: Strongback Boundary Conditions ..... 92

Figure 3.65: Strongback Modes | Left: 32Hz |Right: 71Hz ..... 93

Figure 3.66: Strongback 3G Stress ..... 94

Figure 3.67: Strongback 3G Total Deformation ..... 94

Figure 3.68: Strongback Support Connections ..... 95

Figure 3.69: Strongback Support Mesh and Boundary Conditions ..... 97

Figure 3.70: Strongback Support Modes | Left: Free RDOF 9 Hz | Right: Fixed RDOF 20 Hz.. 97

Figure 3.71: Strongback Support, 5G Load, Free RDOF | Left: Deformation | Right: Stress ..... 98

Figure 3.72: Strongback Support Simplified Mesh ..... 99

Figure 3.73: Vessel Mesh ..... 100

Figure 3.74: Vessel Boundary Conditions ..... 100

Figure 3.75: Vessel Modes | Left: 32 Hz |Center: 36 Hz | Right: 45 Hz ..... 101

Figure 3.76: Vessel Structural Results | Left: 1.5G Stress | Right: 5G Stress ..... 102

Figure 3.77: Vessel 5G Total Deformation..... 102

Figure 3.78: Transport Mount Submodel | Left: Boundary Conditions | Right: Stress ..... 102

Figure 4.1: B90 Cavity String Section Mesh and B.C.'s ..... 104

Figure 4.2: B90 Cavity Assembly Modes | Left: 19 Hz Transverse | Right: 23 Hz Axial..... 105

Figure 4.3: B90 Cavity Assembly Modes | Left: 30 Hz Twist | Right: 34 Hz Coupler ..... 106

Figure 4.4: Coupler 3G Results | Left: Stress | Right: Deformation ..... 107

Figure 4.5: Cavity Support 5G Stress | Left: Assembly Results | Right: Subassembly Results . 107

Figure 4.6: 1.5G Sliding Load Distribution ..... 108

Figure 4.7: Acceleration Event Diagram ..... 109

Figure 4.8: Applied Separation Forces ..... 110

Figure 4.9: 1.5G Sliding Worst Case Deflections | Left: Lug Separation | Right: Cells Position ..... 110

	Page
Figure 4.10: Cavity Support   Left: Previous Design   Right: Stiffer Design .....	111
Figure 4.11: Updated Design Worst Case   Left: Lug Separation   Right: Cells Position .....	111
Figure 4.12: B92 Cavity String Section Mesh.....	112
Figure 4.13: Cavity String Mesh.....	113
Figure 4.14: Cavity String Mesh Detailed View and Boundary Conditions .....	114
Figure 4.15: Cavity String Modes   Left: 21 Hz   Right: 23 Hz.....	115
Figure 4.16: Axial Mode Shape 30 Hz .....	115
Figure 4.17: Transverse Alternating Mode Shape 27 Hz .....	116
Figure 4.18: 5G Stress at Two-Phase Bellows.....	117
Figure 4.19: Bellows Deflection Comparison   Left: Previous   Right: With Guide .....	117
Figure 4.20: Vessel and Strongback Boundary Conditions .....	118
Figure 4.21: Vessel and Strongback Mesh .....	118
Figure 4.22: Strongback Transverse Mode 23 Hz .....	119
Figure 4.23: Cryomodule Mesh .....	120
Figure 4.24: Cryomodule Results   Left: 18 Hz Mode   Right: 1.5G Deformation Shape.....	121
Figure A.0.1: Coupler Antenna Terminology.....	130
Figure A.0.2: Cavity Support M10 Bolts.....	132
Figure A.0.3: Needle Block Lower Bolts .....	133
Figure A.0.4: Needle Bearing Shear Area .....	133
Figure A.0.5: Needle Block Support  Left: Transverse Section View   Right: Axial Section View .....	134
Figure A.0.6: Original Thermal Shield Design.....	138
Figure A.0.7: Strongback Support Connections .....	140
Figure A.0.8: Load Sharing between Needle Supports.....	144
Figure A.0.9: Load Sharing of Tuner Side .....	144
Figure A.0.10: Hypothetical Acceleration Event.....	145
Figure A.0.11: Free Body Diagrams During Acceleration Event.....	145
Figure A.0.12: Free Body Diagram Event A .....	146
Figure A.0.13: Free Body Diagram Event B .....	146

	Page
Figure A.14: Free Body Diagram Event C .....	147
Figure B.0.1: Coupler Previous Analysis Model and 5G Deformaiton .....	149
Figure B.0.2Coupler Previous Analysis 5G Stress Results .....	149
Figure B.0.3Coupler Previous Analysis Mode Shapes .....	150
Figure B.0.4: B90 Previous Analysis Results .....	151
Figure B.0.5: B90 Previous Analysis First Mode .....	151
Figure B.0.6: B90 Previous Analysis Second Mode .....	152
Figure B.0.7: B92 Previous Analysis 3G Stress .....	153
Figure B.0.8: B92 Previous Analysis 3G Deformation .....	153
Figure B.0.9: B92 Previous Analysis Modal Results .....	154
Figure B.0.10: Strongback Previous Analysis 5G Results .....	155
Figure B.0.11: Strongback Previous Analysis 3G Results .....	155
Figure B.0.12: Strongback Previous Analysis Modal Results .....	156
Figure B.0.13: Vessel Previous Analysis 5G Stress .....	157
Figure B.0.14: Vessel Previous Analysis 5G Stress Mount .....	157

## **LIST OF APPENDICES**

	Page
APPENDIX A: ANALYTICAL VALIDATION OF SIMPLIFIED COMPONENTS.....	129
APPENDIX B: PREVIOUS ANALYSIS FOR REFERENCE AND COMPARISON.....	148

# **DEPARTMENT OF ENERGY ACKNOWLEDGEMENT, COPYRIGHT STATEMENT, AND DISCLAIMER**

Work supported by the Fermi National Accelerator Laboratory, managed and operated by Fermi Research Alliance, LLC under Contract No. DE-AC02-07CH11359 with the U.S. Department of Energy.

The U.S. Government retains and the publisher, by accepting the article for publication, acknowledges that the U.S. Government retains a non-exclusive, paid-up, irrevocable, world-wide license to publish or reproduce the published form of this manuscript, or allow others to do so, for U.S. Government purposes.

Neither the United States nor the United States Department of Energy, nor any of their employees, makes any warranty, express or implied, or assumes any legal liability or responsibility for the accuracy, completeness, or usefulness of any data, apparatus, product, or process disclosed, or represents that its use would not infringe privately owned rights.

# 1. INTRODUCTION

Chapter 1 will lay the foundation for this thesis. The following topics are discussed: project background, problem statement, previous studies, detailed cryomodule description, design criteria, and thesis objectives.

Fermilab National Accelerator Laboratory (FNAL) focuses its research on the study of subatomic particles and how they interact with their environment. The experiments conducted require a variety of high-energy particles, all of which start as protons. At the beginning of the “production line,” protons are accelerated in a linear accelerator (LINAC) until they are traveling at 70 % the speed of light with 400 mega electron-volts (MeV) of energy [1]. Once the protons reach the end of the LINAC they travel into the booster where they are further energized, and then onto the different experiments, as shown in *Figure 1.1*.

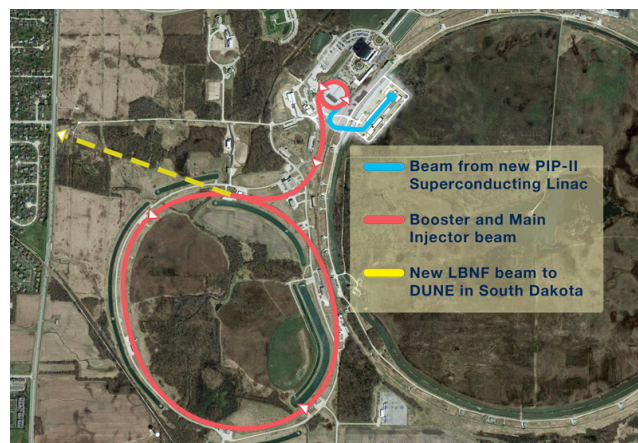


*Figure 1.1: Diagram of Beamlines at Fermilab [2]*

### 1.1 PIP-II Project

As part of the Proton Improvement Plan-II (PIP-II) project, the LINAC is being replaced to increase the beam intensity to 800 MeV. The new LINAC will use superconducting radio-frequency technology (SRF), which uses oscillating high-intensity electric fields to push and pull bunches of charged particles as they travel. Carefully designed niobium cavities are at the heart of the project, as they are directly responsible for creating the acceleration gradient, and one such cavity is shown in Figure 1.2. Once cooled below 9 Kelvin (K) [3], the niobium cavities become superconducting, which allows for negligible heat generation and improved efficiency. To achieve these low temperatures, the cavities are bathed in liquid helium, and a series of cavities are housed along with their support systems in a large vessel known as a cryomodule.

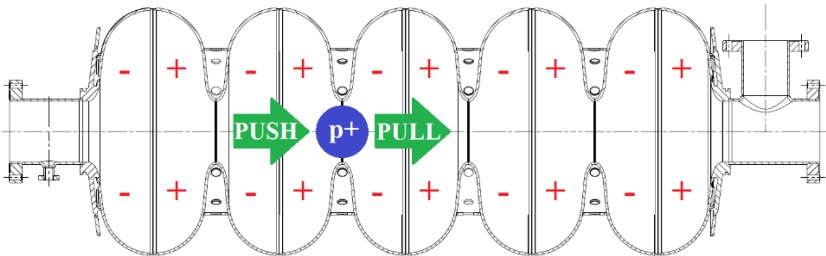


*Figure 1.2: SRF Cavity Proton Acceleration*

Several types of cryomodules are required for the LINAC because, as the protons accelerate, the cavities must have increasingly higher resonant frequencies, which require different geometrical configurations. Figure 1.3 shows a diagram of the different cryomodules in the LINAC, with the beam traveling from right to left as shown. Due to the enormity of the project,

international collaborators from the United Kingdom, France, India, Italy, and Poland will contribute design work, components, and even assembled cryomodules to FNAL.

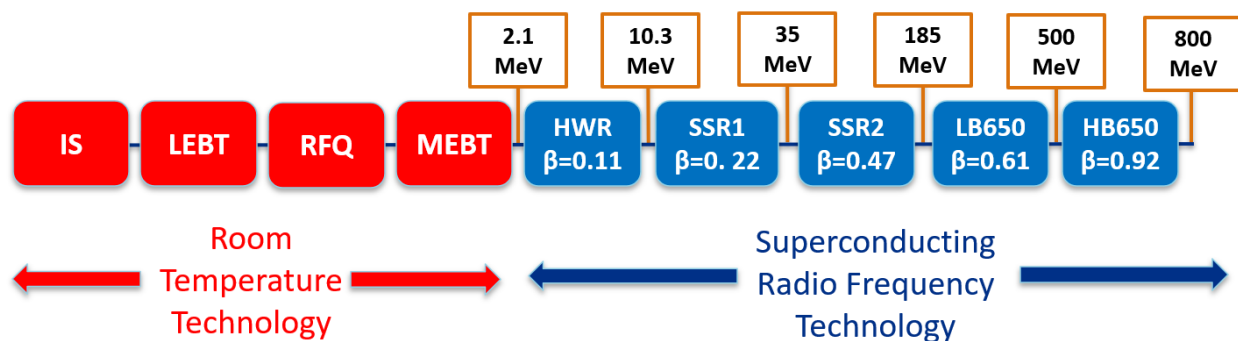
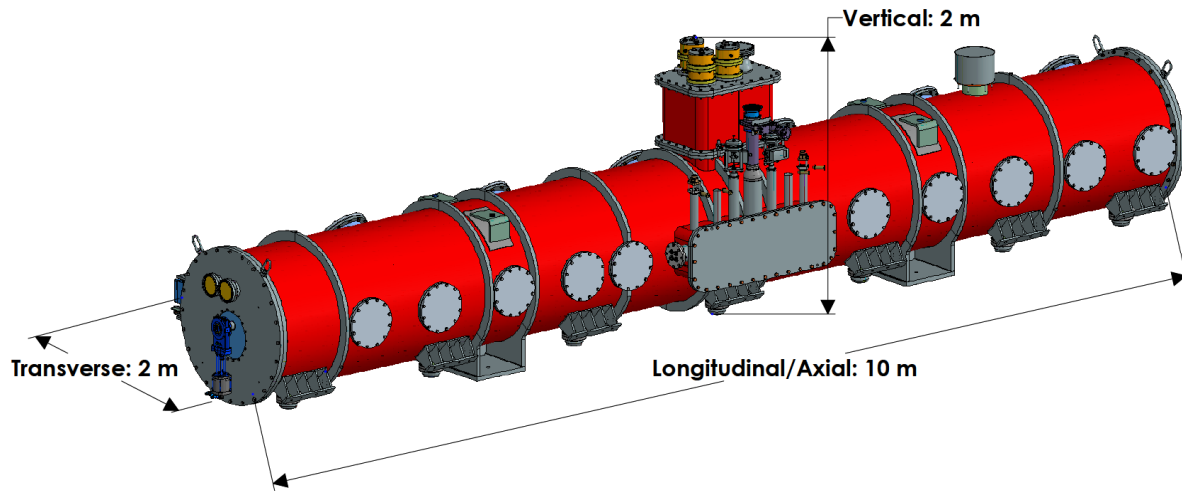


Figure 1.3: Cryomodules in the LINAC [4]

## 1.2 The HB650 Cryomodule

Last in the line of SRF cryomodules is the High-Beta 650 MHz (HB650) cryomodule, as shown in Figure 1.4. In total, four complete HB650 cryomodules will be used in the LINAC. A prototype HB650 will be built at FNAL to validate the design, and if it meets the design criteria, it will be used in the LINAC. The Science and Technology Facilities Council (STFC) of the UK will then build three more HB650 cryomodules and ship them to FNAL. The Department of Atomic Energy (DAE) of India will also contribute by sending a full set of components for an additional HB650 cryomodule should any of the other four fail to qualify.

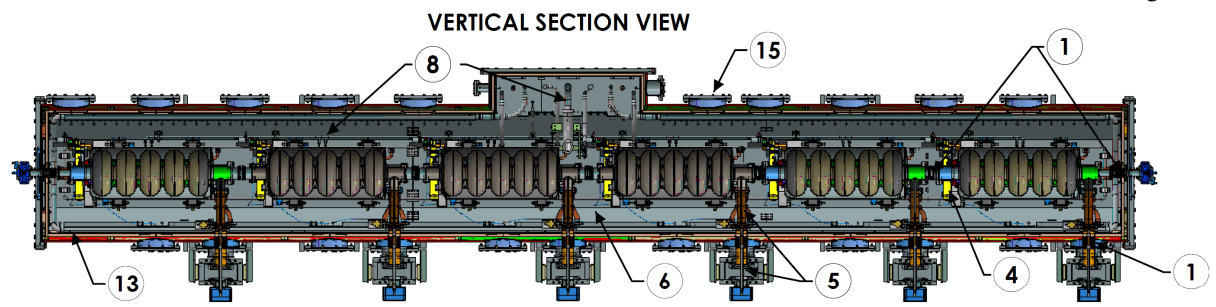
The HB650 is the largest of all the varieties of cryomodules, weighing 13,500 kg, measuring 10 meters in length, 2 meters tall, and 2 meters wide, as shown in Figure 1.4. In all, thousands of components are contained within the outer vacuum vessel, which acts to provide an insulating vacuum.



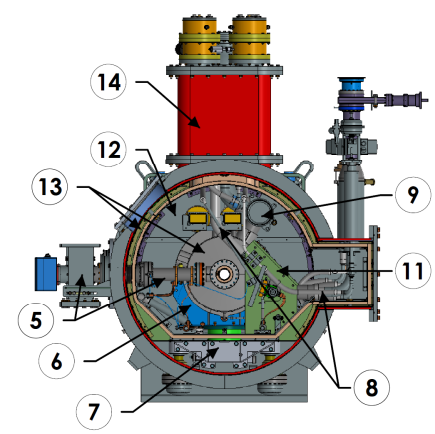
*Figure 1.4: HB650 Cryomodule Exterior*

Shown in *Figure 1.5* are the major subsystems and components of the HB650. In total six cavities are mounted to a strongback which is attached to the vacuum vessel. Each cavity has two supports, a coupler, a tuner, and connects to a shared liquid helium cooling system via the two-phase pipe. Flexible metal bellows are used to connect sections of piping which allows for misalignment and thermal contraction. A thermal shield and multilayer insulation (MLI) limit radiation from the vessel to the so-called “cold mass” within. A global magnetic shield is located just within the vessel walls, and supplemental magnetic shields surround each cavity.

Before delving into further detail about the HB650 components, the problem at hand must be addressed to provide context for the objective of this thesis.



**AXIAL SECTION VIEW**



Number	Component	Number	Component
1	Bellows	9	Two-Phase Pipe
2	B90 Cavity	10	Heat Exchanger
3	B92 Cavity	11	Pumping Line Support
4	Tuner	12	Thermal Shield
5	Coupler	13	Magnetic Shield
6	Cavity Support	14	Vacuum Vessel
7	Strongback	15	Vessel Access Ports
8	Cryogenic Lines	16	

**TRANSVERSE SECTION VIEW**

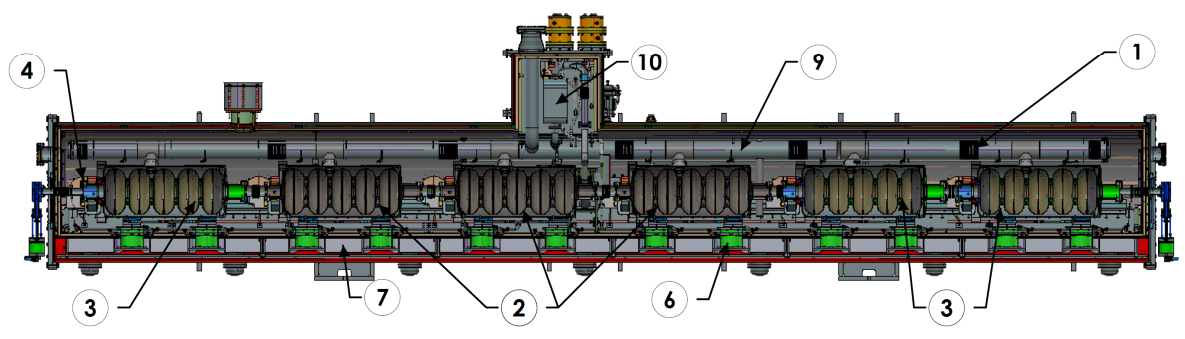


*Figure 1.5: HB650 Cross-Section View*

### **1.3 Problem Statement**

While the prototype HB650 cryomodule will be built at FNAL, it will be transported to STFC and back to validate the design is sufficient to withstand the rigors of transportation. Given the complexity of the cryomodule, this poses significant risk to the internal components which will be subjected to extended periods of vibration and potentially high-magnitude shocks. Previous cryomodule transportations have seen failures occur, and so this is a valid concern. Unfortunately, the majority of the HB650 was not originally designed with transportation loads under consideration. Given all of this, it is important to validate the cryomodule design against possible loading conditions seen during transportation. To do so will require extensive background on the expected loading scenarios and the components to be analyzed.

### **1.4 Background**

#### **1.4.1 Previous Transportation Studies**

The use of SRF technology in cryomodules has been commonplace for over a decade [5], and as such, previous transportation studies can serve as a baseline of expected loading conditions, potential failure modes, and best practices. A two-part transport frame has become the standard with an inner frame mounting directly to the cryomodule and an outer frame attaching to the transport vehicle. Wire rope isolators connect the two and dampen shock and vibration during active transport. This design has been largely successful for cryomodules of varying sizes, and one example is shown in Figure 1.6 and Figure 1.8. Depending on the style of cryomodule used, end caps that limit the movement of the cold mass are installed for shipping, in addition to other

necessary restraints [6]. To minimize shocks to the cryomodules, air-ride trailers and air transport are the preferred methods of transportation [7].

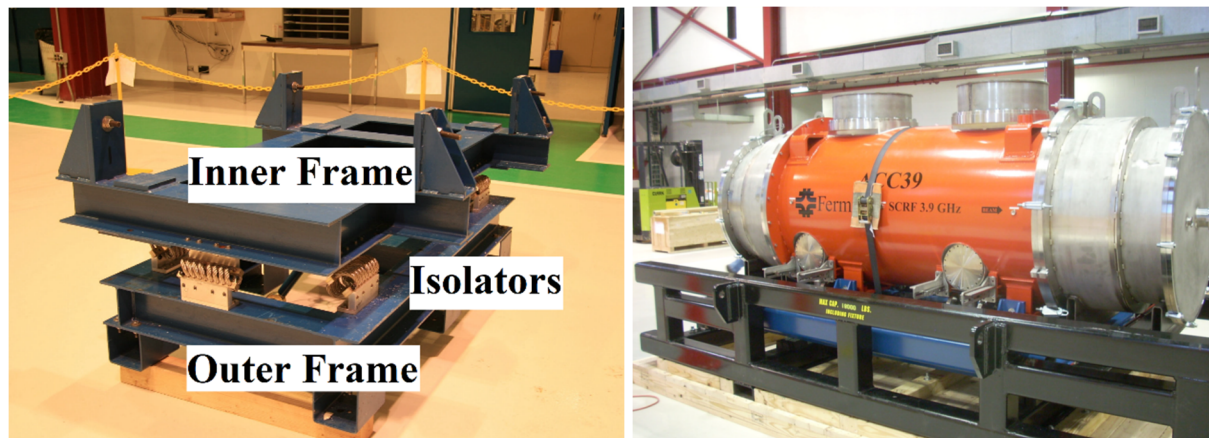


*Figure 1.6: DESY Transport Frame and Cryomodule [5] [8]*

To record the shocks seen during transportation, triaxial accelerometers are mounted to both the inner and outer frames. By processing the data, the power spectral density (PSD), which illustrates at which frequencies the cryomodule experiences the most excitation, can be generated. Generally, below 10 Hz, the transport frame is unable to provide significant isolation and the inner and outer frame move with one another. In this range of 0-10 Hz, excitations include vibration from the air-ride trailer (1.5 - 2 Hz) and rigid body motion of the cryomodule (2 – 6 Hz) [9] [10]. A PSD plot from the HB650 frame analysis is shown in Figure 1.7, which illustrates that above the natural frequency of the cryomodule (roughly 3 Hz), the response drops significantly and the springs dampen input excitations.

In addition to the PSD, the maximum shocks to the cryomodule can be determined. These values will vary based on the method of transport, the route taken, and the specific isolation frame used. Generally, the vertical shocks have the highest magnitudes, followed by transverse and axial

directions. Table 1-1 provides a summary of the shocks recorded by several different experiments which were recorded on the inner frame or internal cryomodule components. The values presented are for the finalized configuration of each isolation frame, and it should be noted that the HB650 will be most similar to LCLS-II, although no previous transport frame has been mounted directly to the cryomodule as will be done for the HB650.

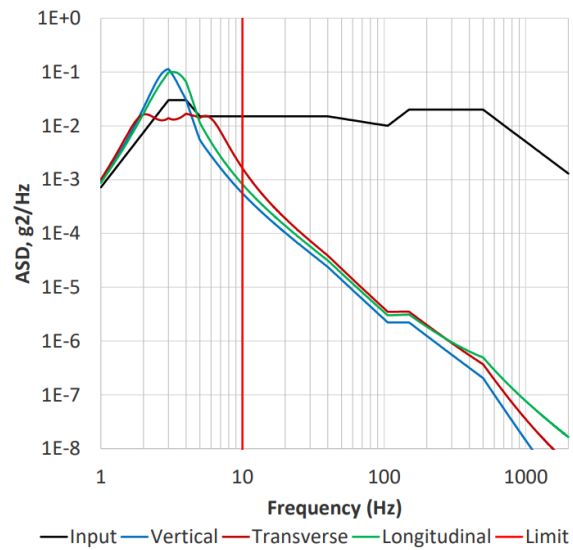


*Figure 1.7: Example Transport Excitation Spectrum [11]*

Validation of an isolation frame's performance before use has not been a consistent requirement across projects. In the case of the Deutsches Elektronen-Synchrotron (DESY) 3.9 GHz cryomodule, significant effort was taken in performing on-site and off-site road tests with a mock cryomodule to understand the expected loads [5]. There were no reported issues with the DESY transportation. In contrast, the European X-Ray Free Electron Laser (XFEL) project did not perform any initial mock tests, and the frame had several problems. The first frame created did not provide adequate isolation, and a second had to be procured. The second frame was then

initially used with a non-air ride trailer and was subsequently installed incorrectly on the trailer, allowing high-magnitude shocks to reach the cryomodule. While none of these issues caused damage to the transported cryomodules [12], similar issues have been catastrophic for other projects, as was the case for the LINAC Coherent Light Source – II (LCLS-II) cryomodules.

*Table 1-1: Maximum Shocks at Internal Frame During Previous Cryomodule Transportations [7] [9] [12] [13] [14]*

Project	Vertical Shock (G)	Transverse Shock (G)	Axial Shock (G)
EXFEL	2.7	2.2	1.3
SNS	1.5	0.75	0.75
DESY	2.2	0.9	1.0
LCLS-II	1.5	1.0	1.0
FLASH	1.5	0.8	0.6

In a partnership with SLAC National Accelerator Laboratory, FNAL assembled and shipped many 1.3 GHz cryomodules from Batavia, IL, to San Francisco, CA. For the first two modules shipped, bellows on the coupler ruptured and spoiled the beamline vacuum. This resulted in significant project delays, along with millions of dollars spent in labor to disassemble and clean the cavity string. Studies determined that the isolation springs were extremely stiff and provided minimal damping from road noise. This high level of excitation, when combined with the flexibility of the coupler, caused the bellows to fail via fatigue due to repeated flexing in the longitudinal direction. Validation of the frame’s isolation performance and FEA of the internal

components did not take place before transportation [6]. The fatigued bellows and the LCLS-II transport frame are shown in Figure 1.8.

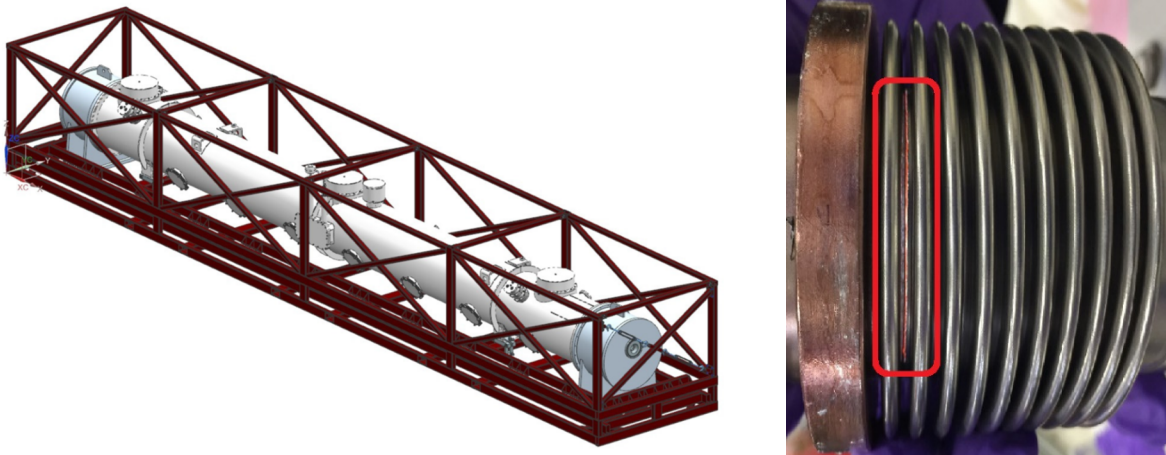


*Figure 1.8: Left: LCLS-II Transport Frame | Right: LCLS-II Cracked Bellows [9]*

#### **1.4.2 Previous Transportation Analysis**

Finite element analysis is a powerful tool for cryomodule transportation analysis, as often the complex components do not lend themselves easily to analytical methods. The extent and methods of analysis performed has varied by project. Primary methods include modal analysis, harmonic response analysis, and structural analysis.

Modal analysis and harmonic analysis are both useful to determine a component's response to vibration, with their primary difference being that modal analysis determines the resonant frequencies and corresponding mode shapes, while harmonic analysis determines the true deformation and stress response to a given cyclic excitation. In the past, both have been used to predict the response of cryomodules to vibration, which can then be validated with data from impact hammer testing or transportation tests [5]. In general, harmonic response analysis has only

been accurately validated for individual components, and the response of larger assemblies does not correlate well to the predicted response [15]. This is largely due to the difficulty in accurately estimating the damping factors of the component, which can have a significant effect on predicted response.

Structural analysis has been used to determine stress induced by shocks, which applies the maximum shock as a static load, inducing the maximum possible deflections and stresses. Transient analysis is not often used for shock analysis as it is computationally expensive, the results are sensitive to material damping factors, and generally the worst case is already captured by a static structural analysis. The SNS project used static structural analysis to check all cryomodule components against their maximum shock criteria [13], and a study for the Large Hadron Collider crab cavity support did as well [16]. The use of static structural analysis to check stress in the event of a shock is commonplace at FNAL and was used previously in the analysis of the initial HB650 design.

Often, modal analysis has not been performed before transportation occurs, or if it is, only for select components. Instead, it is often a reactionary measure to better understand a problem. This was the case for LCLS-II, where modal analysis of the coupler had not been performed beforehand. After the failures occurred, FEA was performed, and the resonant frequency matched that of further transportation tests. Based on the mode shape, mounts were designed to restrain the bellows movement and evaluated on both a shaker table and in the cryomodule [9].

Even though the EXFEL project had shipped over 800 couplers without issue, since they had a very similar coupler design to LCLS-II, they performed FEA analysis and shaker table tests of their coupler design to ensure its validity. Modal, prestressed modal, and harmonic response

analysis were performed, which agreed well with the measured response. After multiple tests, the bellows ultimately failed, and this is still being investigated [17]. A recommendation of the study was to ensure the transport frame effectively damped excitation near the coupler resonance of 18 Hz to minimize the likelihood of this failure. Figure 1.9 shows the first mode shape of the coupler and the experimental setup, and Figure 1.10 compares the predicted and experimental system responses. These results match rather well, which indicates the accurate predictive power of harmonic response analysis for small assemblies. The same peak frequencies were identified using a simple modal analysis as well.

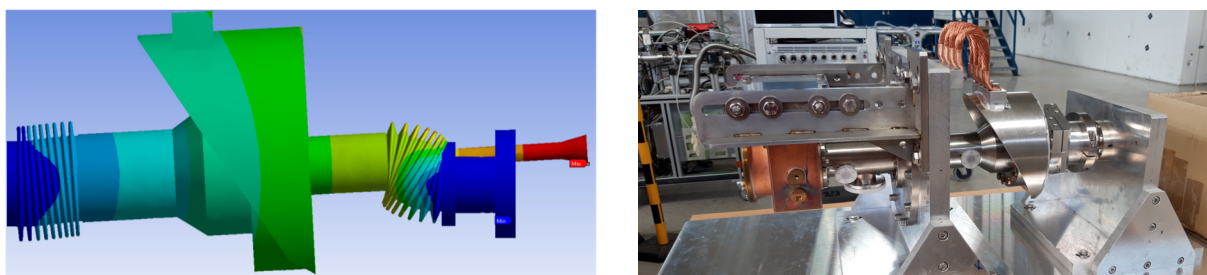


Figure 1.9: EXFEL Coupler | Left: Modal Analysis | Right: Shaker Table Test [17]

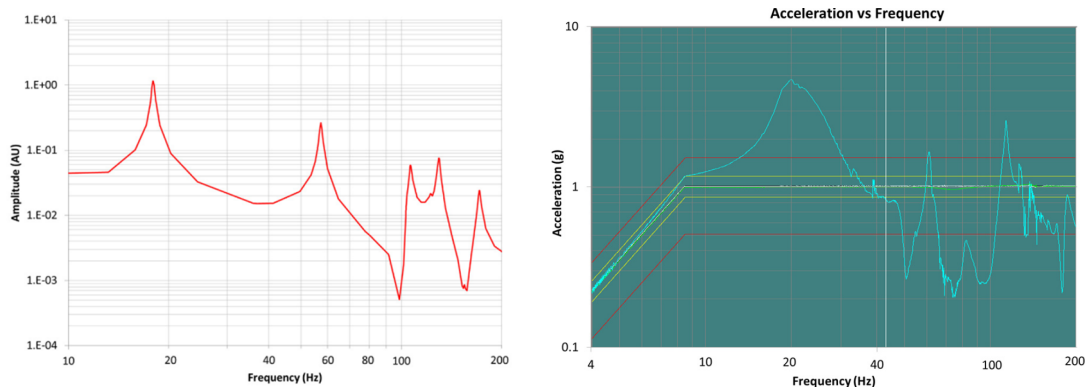
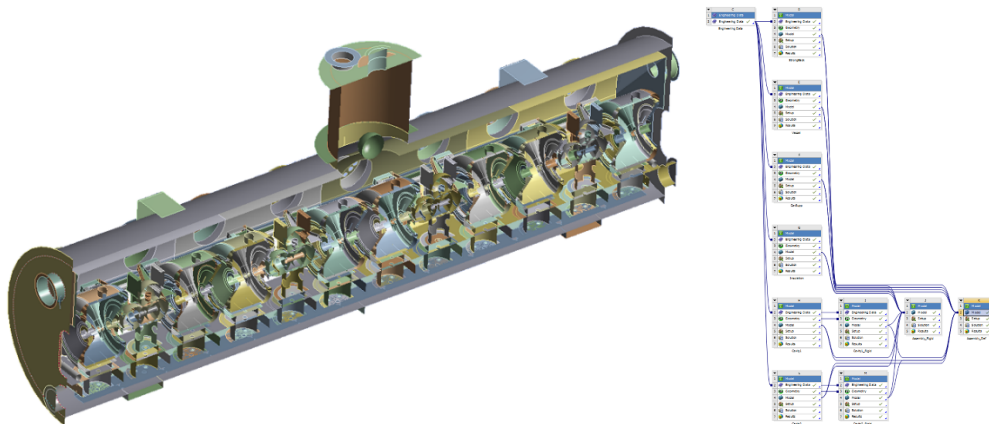


Figure 1.10: EXFEL | Left: Predicted Response | Right: Actual Response [17]

Within the PIP-II project, significantly more transport analysis has taken place because of the LCLS-II issues, with the intent to mitigate failures before they can occur. In a study performed by the University of Pisa, an FE model of the SSR1 cryomodule was created to design and analyze a transportation frame. The major components of the module were first analyzed individually, and then combined to form a full assembly. This was done using ANSYS®, and significant effort was made to only include shell elements and merge nodes to avoid the need for contacts. The model and Workbench™ tree are shown in Figure 1.11. The results of the modal analysis were then used as input to the design of the isolation frame. By understanding the lowest mode frequencies of the cryomodule, they were able to determine what spring stiffness should be used to keep excitation frequencies at the inner frame below any critical component resonances [10].



*Figure 1.11: SSR1 Cryomodule Analysis [10]*

Similar to the SSR1 analysis, Dr. Sergey Cheban of FNAL completed transportation analysis of the HB650 cryomodule for its preliminary design. The FE model included all major components, and the work was performed in ANSYS® Workbench™. In addition to modal analysis, structural analysis was performed separately for the cases of 3G vertical, 5G axial, and

1.5G transverse [18]. Section views of the model are shown in Figure 1.12, and a sample of the results is shown in Figure 1.13. The initial results served as valuable input to the design of the cryomodule. For the bellows, which are critical components, their maximum deflections and stresses were checked to be within the allowable limits. While not available, similar analysis has been performed retroactively for the entire LCLS-II cryomodule to identify other potential areas of failure.

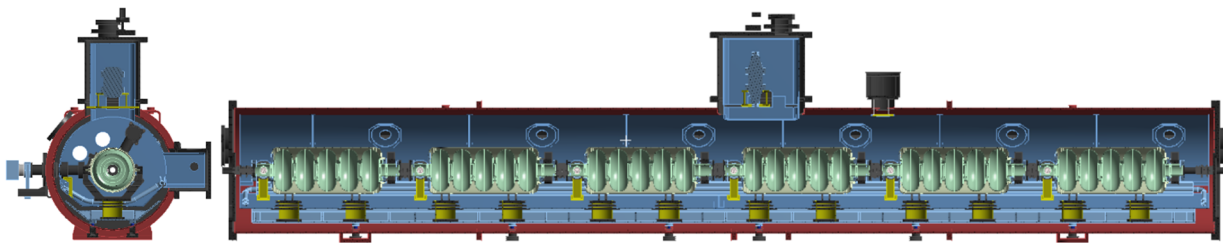


*Figure 1.12: HB650 Preliminary FE Model [18]*

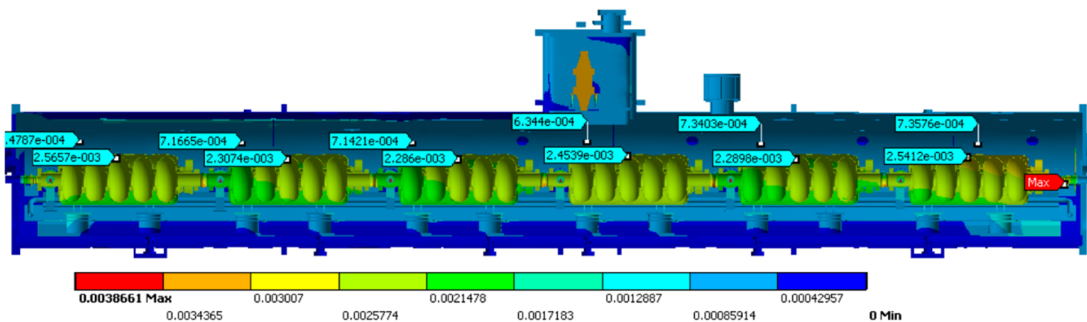


*Figure 1.13: HB650 Preliminary 5G Deformation Results [18]*

### **1.4.3 Transportation Plan and Configuration**

Like previous transportation efforts, air-ride trailers will be used to transport the HB650 to the airport, where it will then make the trans-Atlantic journey. A purpose-built transport frame will

act as an interface at all hand-off points, and it is shown in Figure 1.14. Hook points for an overhead crane are built into the frame, and during road transit, straps and chains will positively secure the frame to the trailer.

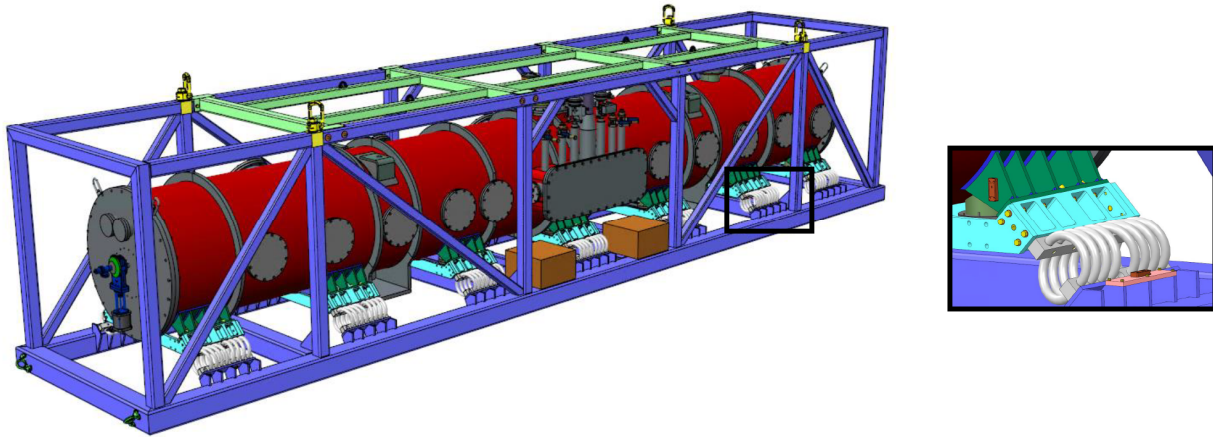


*Figure 1.14: Transportation Frame [11]*

In addition to acting as an external interface, the transport frame will dampen shock and vibration seen by the cryomodule. Fourteen wire rope isolators connect the frame to the vacuum vessel weldment and intermediate cradles. Each isolator is positioned at a  $45^\circ$  angle to provide ideal response in both transverse and vertical directions. Per FNAL specifications, the frame shall limit shock to the HB650 to 3.5G axial, 2.5G vertical, and 1.5G transverse. It shall also provide 80% excitation isolation above frequencies of 10 Hz [11]. Data acquisition (DAQ) modules will be mounted before and after several isolators to record acceleration data, which will be indicative of isolation performance and serve as a record of the excitation seen by the HB650.

To fit within the envelope of the frame, certain components are removed for transportation. This includes the chimney of the vessel, part of the couplers, and certain cryogenic valves. Several restraints are installed to support critical components, which are then removed after transport.

Additionally, the vessel and beamline are pressurized slightly above 1 atm with nitrogen. This ensures that if a leak were to form in the beamline, atmospheric air could not contaminate the clean environment, which would allow for repair without complete disassembly and reprocessing of the SRF cavities. This was a lesson taken from the LCLS-II failures.

For on-site transportation at FNAL, an existing PIP-II frame will be used which does not require the removal of any components for use. Travel will be conducted at very low speeds (<10 MPH) to ensure cryomodule components do not see significant excitation. This configuration is not the express concern of this thesis, although some improvements have been made to the cryomodule design for this case because of the work done for this thesis.

#### **1.4.4 HB650 Subassemblies Design Overview**

The following section provides detailed information for most components comprising the cryomodule. First, an overview of common materials and their properties will be given.

#### **Materials**

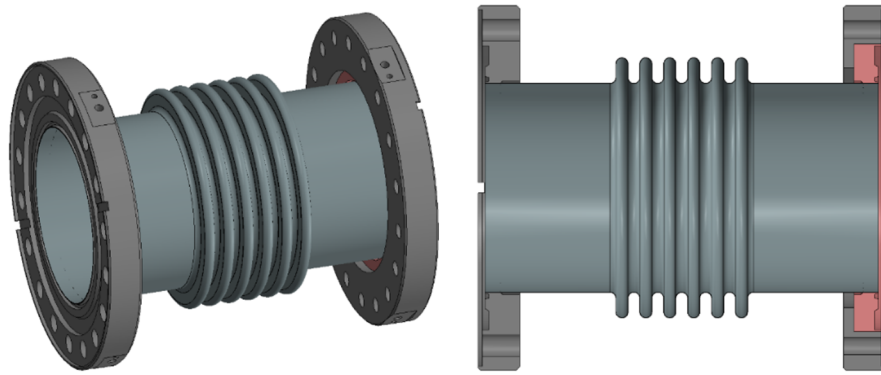
The most common materials used in the HB650 are stainless steel 316L (SS316L), demagnetized A516 steel, 6061 and 1100 aluminum, grade 2 titanium (Ti-2), niobium, niobium-titanium alloy, silicon-bronze, Mu-metal, G-10 fiberglass epoxy, oxygen-free high-conductivity (OFHC) copper, and AlO<sub>2</sub> ceramic. The mechanical properties and best use case of each are shown in Table 1-2, and the reasons for material selection are discussed in each subassembly section. Material properties were primarily sources from the FNAL database.

Table 1-2: Material Properties

Material	Primary Components	Yield Stress (MPa)	Elastic Modulus (GPa)
SS316L	Strongback, Piping, Tuner, Bellows	205	195
SS304L	Vessel Components	215	195
A516 Steel	Vacuum Vessel	262	200
Al 1100-H14	Thermal Shield	60	69
Al 6061-T6	Cooling Lines	96	69
Ti Gr 2	Cavity Supports	275	106
Ti Gr 2 P.V.*	Jacket, Cavity Bellows	99	106
Nb55-Ti45 P.V.*	Transition Spools	156	62
Niobium P.V.*	Cavities and Beamline	30	105
Invar	Two-Phase Pipe Assy.	276	152
Si-Brz	Strongback Supports	340	200
Mu-Metal	Magnetic Shields	160	216
OFHC Copper	Coupler, Thermal Links	50	117
Copper Brazing	Coupler	50	117
Al <sub>2</sub> O <sub>3</sub> Ceramic	Coupler Window	100	375
G-10	Supports	262	17
* As used in a pressure vessel			

## Bellows

Bellows are integral to connections between many components, as their multiple convolutions make them flexible, which allows for misalignment and thermal contraction. Each bellow is designed to specific displacement requirements and has a minimum life of 10,000 cycles when extended to maximum displacement. Over 30 bellows are used in the HB650, with the majority used in the two-phase pipe, cavity string, and coupler subassemblies. Due to previous failures involving bellows, they are a highly scrutinized component for transportation analysis. An example bellow is shown in Figure 1.15.



*Figure 1.15: Intercavity Bellow*

### **B90 Dressed Cavity**

Three of the six cavities in the prototype cryomodule will be of the B90 variety, and a section view of the dressed B90 cavity is shown in Figure 1.16. The niobium cells are encased in a titanium jacket which allows for a bath of liquid helium to cool the cells during operation and acts as a structural interface to the cavity supports and tuner as shown in Figure 1.17. Niobium is used for the cavities due to its superconducting properties, and titanium is used for the surrounding components as it has a higher yield strength and less magnetic interference than SS316L. The two-phase pipe connects all cavities for cooling, and fill lines for the system are at the bottom of the jacket. The two-phase pipe is SS316L since it is far enough away from the beamline that it will not affect SRF performance, and it is more cost effective than Ti-2. Components of 55Ti-45Nb connect the jacket and cells and, since they are an alloy of both Nb and Ti-2, allow for a fully welded connection between the components.

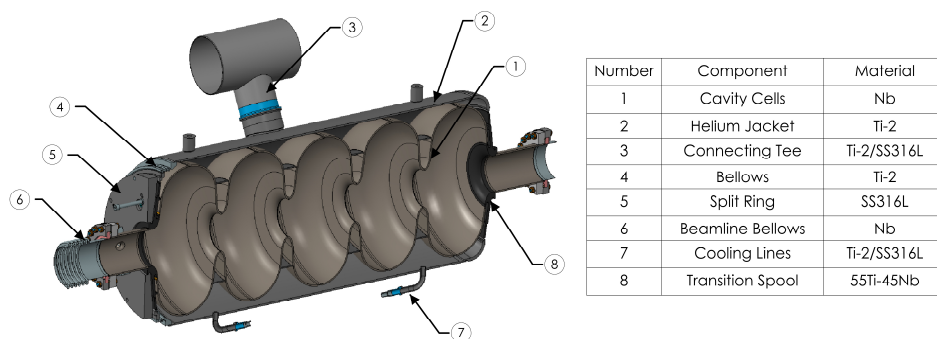


*Figure 1.16: B90 Cavity Components*

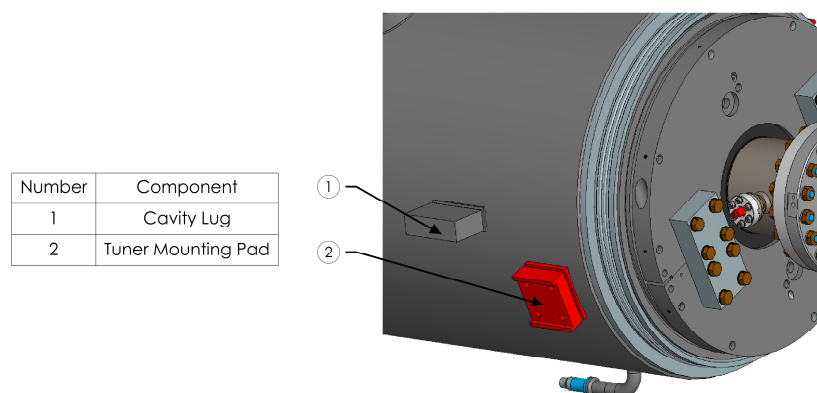


*Figure 1.17: Cavity Jacket Mounting Interfaces*

A bellows at one end of the jacket allows for force applied to the split ring, which attaches to the far end of the cavity, to compress the cavity longitudinally. A section view of this area is shown in Figure 1.18. This is required since the cavity must be tuned to its resonant frequency, which must be held to  $\pm 10$  Hz on the order of 650 MHz. The split ring is made from SS316L instead of Ti-2 since it must be extremely stiff. Flanged bellows connect the cavities in series and allow for separate ultra-high and high vacuum environments within the beamline and the vessel, respectively.

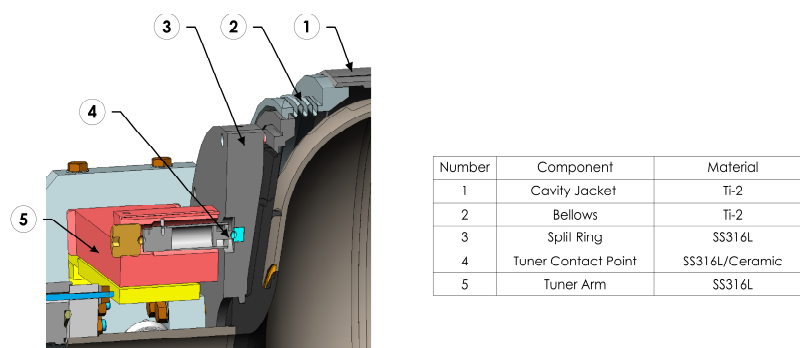


*Figure 1.18: Section View of Cavity End*

## B92 Dressed Cavity

The remaining cavities in the prototype cryomodule will be of the B92 variety, which is an improvement upon the B90 design. For all subsequent HB650 cryommodules, only the B92 cavity will be used. Fundamentally, the design is very similar to the B90, as can be seen in Figure 1.19. The primary difference is the smaller bellows and the lack of a heavy split ring. Instead, the 55Ti-45Nb transition spool is used to apply compressive forces for tuning. Even with this difference, both the B90 and B92 weigh nearly 300 kg when fully assembled with all components such as the tuner, coupler, and magnetic shields.

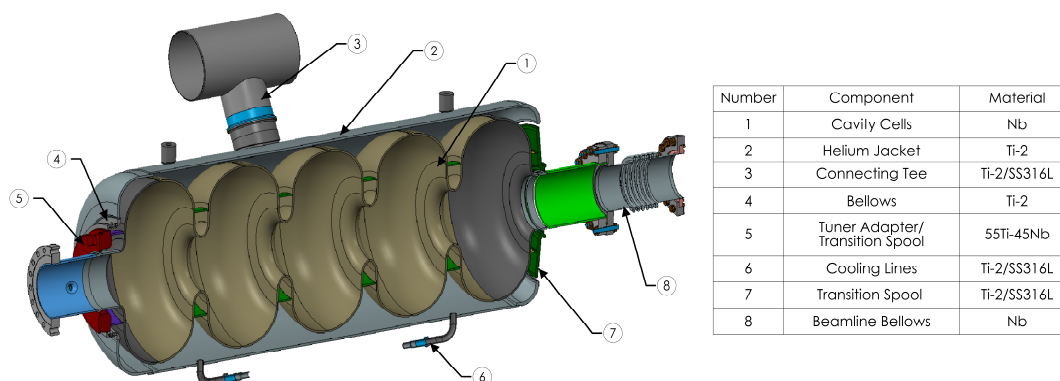


*Figure 1.19: B92 Cavity Components*

## Tuner

The primary function of the tuner is to adjust the resonant frequency of the cavity by mechanically compressing it. As shown in Figure 1.20, the tuner attaches via welded lugs on the cavity jacket. The bellows between the cavity jacket and the split ring, where the force is applied, allows the tuner to compress the cavity. Figure 1.18 shows a section which may aid in understanding this process.

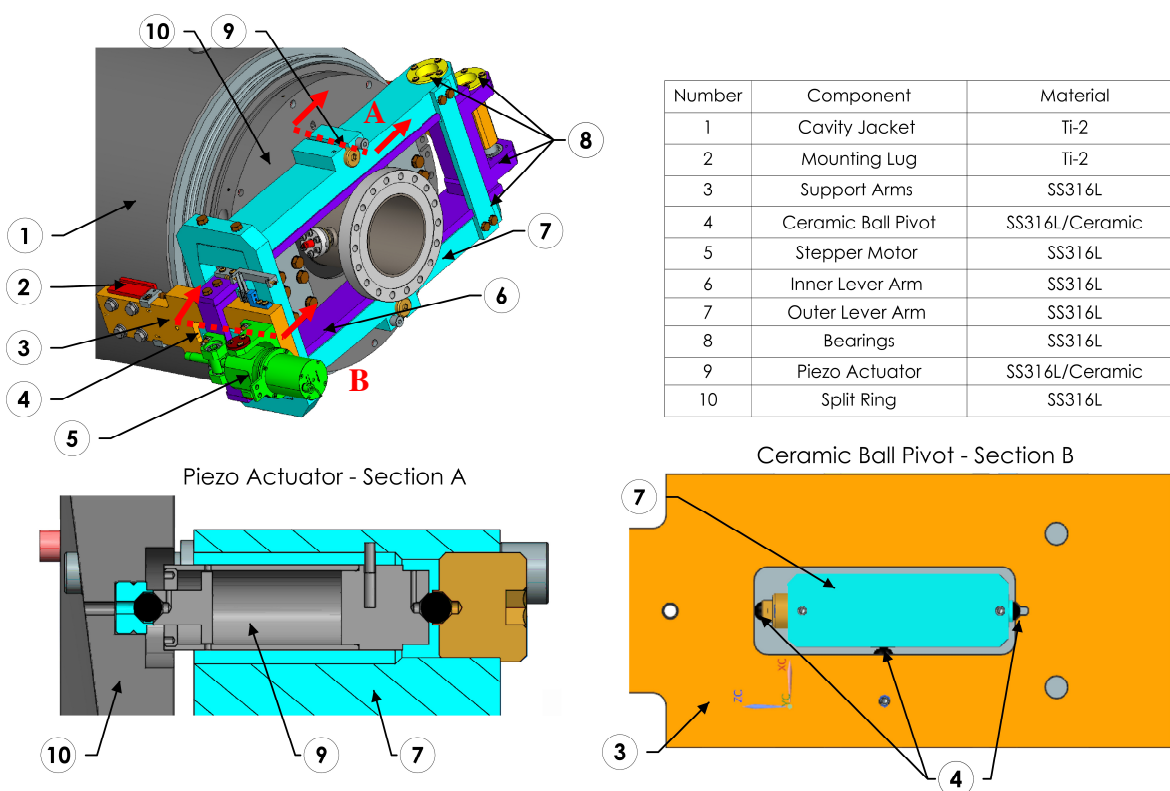
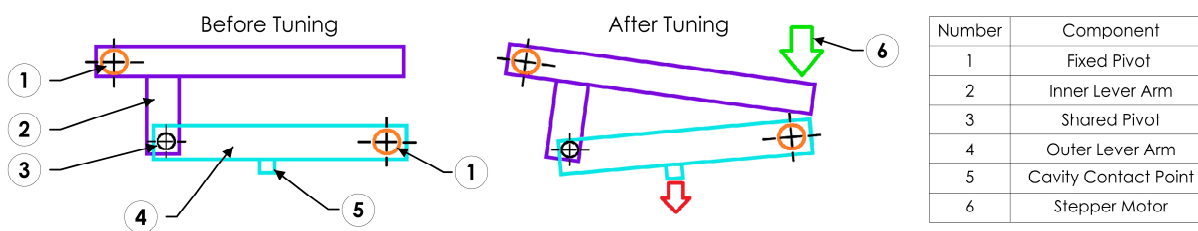


Figure 1.20: Tuner Components

There are two separate tuning mechanisms: the slow tuner and the fast tuner. The slow tuner uses a stepper motor and ball screw to rotate the first lever arm, which in turn moves the

second lever arm at finer resolution than the first and also acts to multiply the force applied to the cavity. An exaggerated depiction of the mechanism is shown in Figure 1.21. This process takes place before the cryomodule is in operation and is only able to roughly adjust the frequency. The fast tuner uses a piezo actuator to make quick, fine adjustments to the cavity length during cryomodule operation to ensure the resonant frequency is actively maintained. This is done by varying the voltage sent to the piezo. Overall, the tuner was designed to be extremely stiff to improve the tuning characteristics of the cavities [19], with a total axial stiffness of 40 kN/mm. This necessitated the use of SS316L over Ti-2 and ceramic balls to accept the high compressive forces. Similar two-part tuner designs have been used successfully in the past for SSR1 cryomodules.



*Figure 1.21: Slow Tuner Mechanism*

## Coupler

The coupler functions to excite the cavity to its resonant frequency during operations, and it consists of two primary sections, warm and cold, which are connected via a bellows. A section view of the coupler is shown in Figure 1.22. The function of the warm coupler is to generate the signal which is then delivered by the cold end. The warm coupler attaches to the vacuum vessel

but is removed for overseas transportation to lessen the risk of damage and to fit within the frame envelope. On the cold coupler, the innermost flange mates with another on the beamline. A copper and stainless steel antenna which affixes to a ceramic window spans the length of the cold coupler and ends just short of the beamline. The ceramic in this case serves to isolate the excitation signals from surrounding conductive components. Brazing is used to connect the copper and ceramic components. Like bellows, the coupler is a highly scrutinized component due to its relative fragility and critical role in cryomodule operations.

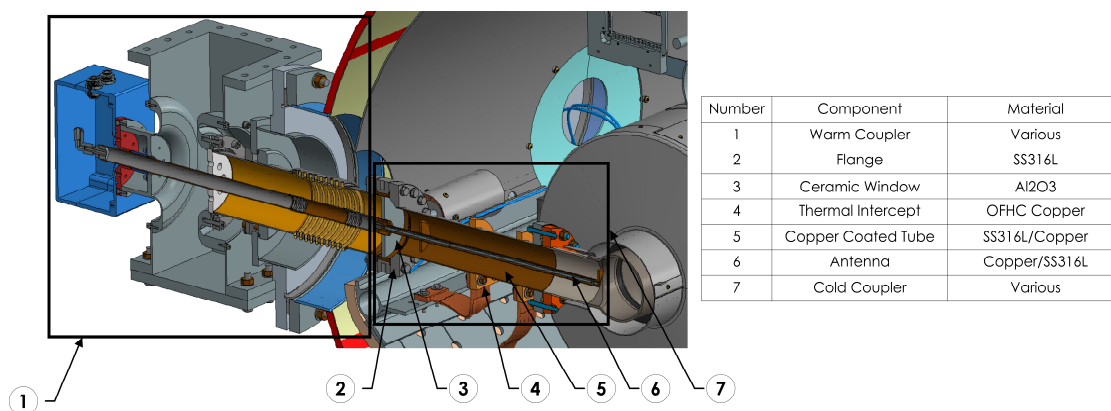


*Figure 1.22: Coupler Components*

## Cavity Supports

The cavity supports have three primary roles: thermal isolation, positioning of the cavities, and support of the thermal shield. As seen in Figure 1.23, a G-10 base separates the 300K strongback from the 2K cavity. The extremely low thermal conductivity of the G-10 base (0.6 W/m-K vs 50 W/m-k for common steel) is aided by two thermal intercepts at 5K on the support and 50K on the thermal shield support plate. The support is primarily made of Ti-2 due to its low magnetic interference, and the thermal shield plate is made from aluminum to better conduct heat.

Needle supports connect to the cavity lugs and allow for alignment corrections to the cavity position as shown in Figure 1.24. The top, bottom, and outer faces of the lug are supported by needle-bearing assemblies that pivot at a single point to allow for some misalignment between the lugs of an individual cavity. Spring jacks – which contact the lugs and are spring loaded using Belleville washers – maintain positive contact during thermal contraction. Locks on the spring jacks are used to prevent movement only during transportation.

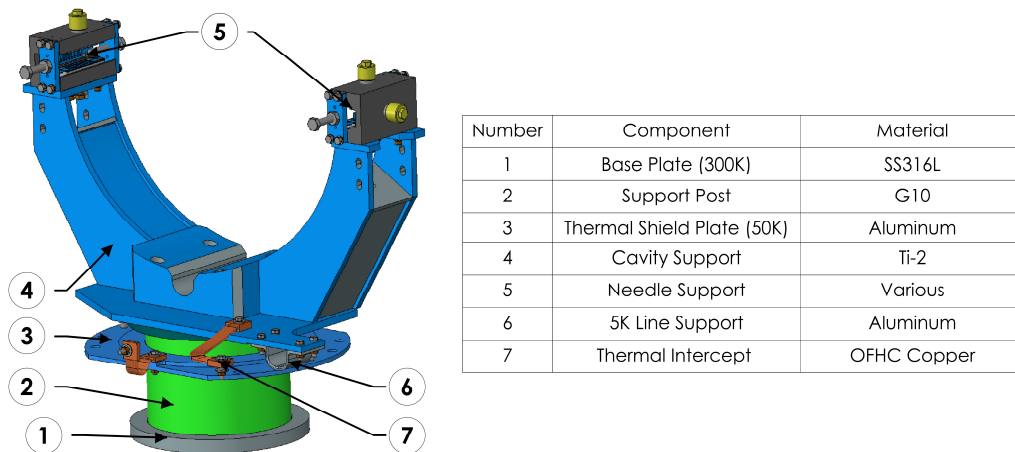


Figure 1.23: Cavity Support Components

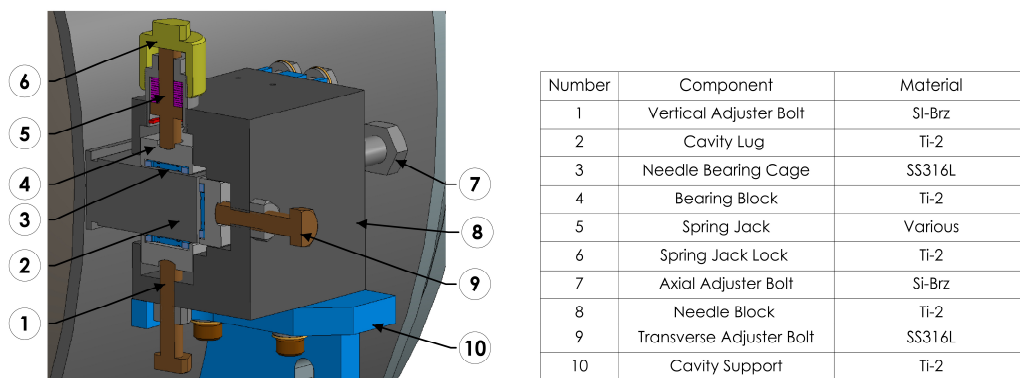
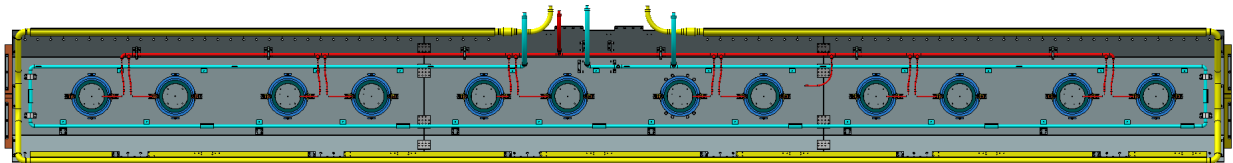


Figure 1.24: Needle Support Components

### Cryogenic Lines and Pumping Line Support

There are three separate cooling lines which are shown in Figure 1.25: 50K (yellow), 5K (blue), and 2K (red). The 50K line is a part of the thermal shield weldment and is responsible for cooling the thermal shield and any attached intercepts. The 5K line is supported via clamps attached to the cavity supports, and only one location on the line is fixed to allow for thermal contraction. This line cools components such as the Ti-2 cavity supports and couplers. Brackets at either end of the thermal shield prevent axial movement of the 5K line during transportation. The 2K line provides the liquid helium which cools the cavities and connects to the bottom of each cavity jacket. These lines and others are supported by the pumping line support, as shown in Figure 1.26, which is made from G-10 to limit thermal conduction. The 50K line is made from 6061 Al as it must be welded to the aluminum thermal shield, and the other lines are SS316L instead of aluminum as they must be able to support their own weight across spans up to 2 meters.



*Figure 1.25: Cooling Lines | Yellow 50K | Blue 5 K | Red 2K*

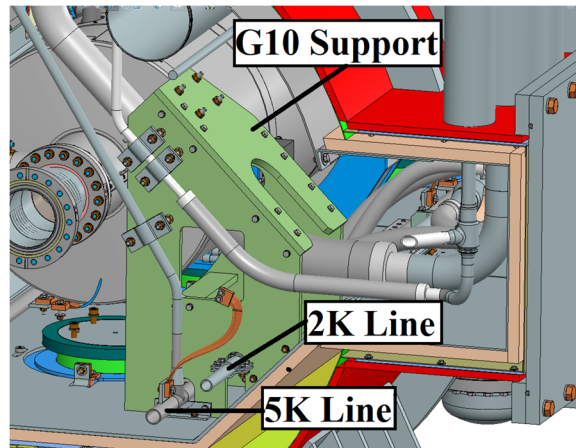
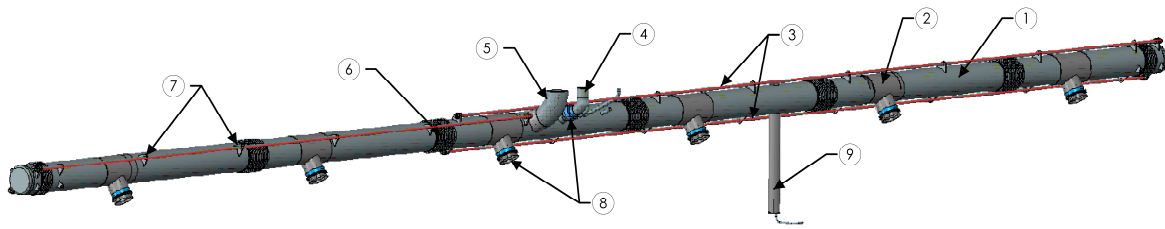


*Figure 1.26: Pumping Line Support*

### **Two-Phase Pipe and Heat Exchanger**

The two-phase pipe functions to create a single cooling system shared by all cavities, and it is shown in Figure 1.27. A welded tee to the cavity jacket supports each individual section of the pipe, which is then connected via bellows to allow for misalignment and contraction. Invar rods, which attach only rigidly to the far ends and central section, balance excessive axial forces in the event the internal vessel cavity becomes pressurized. Otherwise, each end cavity would see high axial forces as the pressure applied to the endcaps would be unbalanced. The rods are supported with guides along each section. Connections to the heat exchanger and pressure relief pipe are at the center section of the two-phase pipe, as shown in Figure 1.28. A support attached to the vessel walls constrains both axial and transverse positions of the heat exchanger, which is necessary due to its cantilevered nature. Flanges on the heat exchanger allow removal for transportation to STFC after qualifications are made at FNAL.



Number	Component	Material
1	Piping	SS316L
2	Connecting Tee	SS316L
3	Invar Rods	Invar
4	Pipe To Heat Exchanger	Alum.
5	Pipe To Relief Line	SS316L
6	Bellows	SS316L
7	Invar Rod Guides	SS316L
8	Bi-Metallic Parts	SS316L/Ti-2 or SS316L/Alum.
9	Liquid He Level Sensor Pipe	SS316L

*Figure 1.27: Two-Phase Pipe Components*

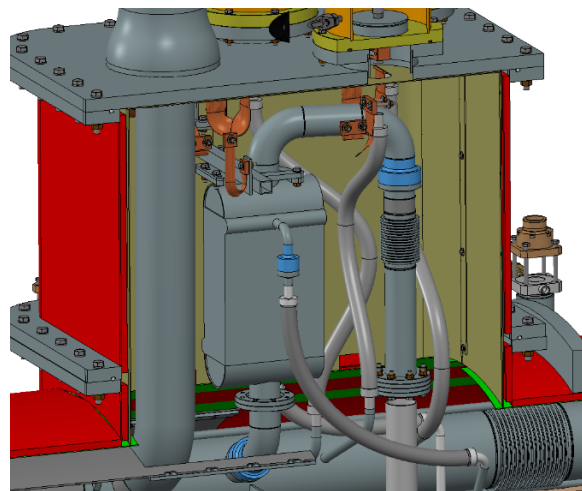


*Figure 1.28: Heat Exchanger*

## Thermal Shield

The thermal shield, as seen in Figure 1.29, is cooled to 50K during operations and primarily serves to limit radiant heat transfer from the vessel to the components within. Cutouts in the lower half allow the shield to be supported by the cavity supports. One central location on the

lower half of the shield is bolted to a support post, while the others have slotted connections to allow for thermal contraction axially. The 50K line (yellow) is part of the weldment, and it connects the upper and lower halves. All shield components are either 6061 or 1100 aluminum, which allows for effective heat conduction. Not shown are the 30+ layers of MLI between the shield and vessel, which further reduce heat transfer. G10 bumpers on the shield contact the vessel to prevent excessive movement during transportation. A support at the top port is installed for transportation, which connects the nearest sections of the shield to the vessel.

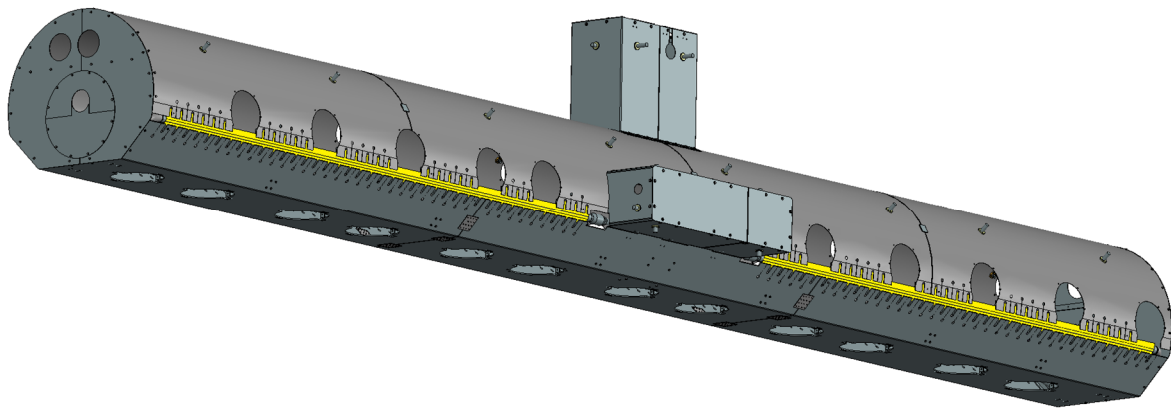


*Figure 1.29: Thermal Shield*

### **Magnetic Shields**

The global magnetic shield, as shown in Figure 1.30, affixes to the inner wall of the vacuum vessel via screws at each of the ribs. Additionally, each cavity has its own local shield, further protecting the cavity cells from magnetic induction. This is necessary as even Earth's magnetic field is 100x stronger than the allowable magnetic flux of 5 milligauss [20]. A nickel-iron alloy known as Mu-metal is used for the shields due to its very high levels of permeability that redirect the stray magnetic fields.

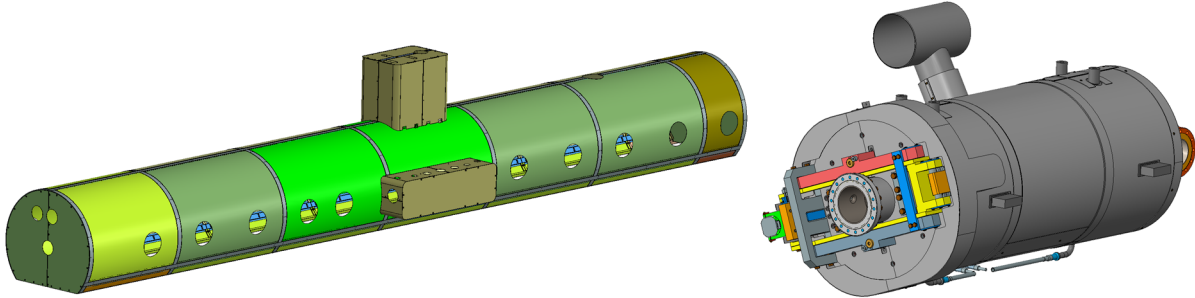
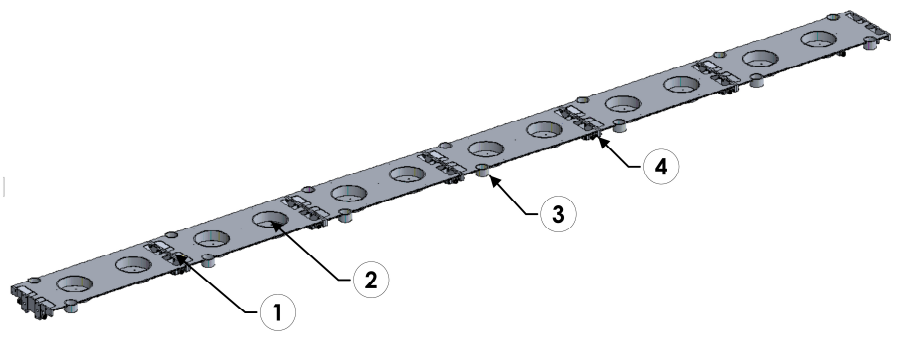


*Figure 1.30: Global and Local Magnetic Shields*

### **Strongback**

The strongback, as shown in Figure 1.31, supports the cold mass, which is shown in Figure 1.32. Once the cold mass is assembled, it is rolled into the vessel on the rail system and then affixed to and lifted by the supports. In total, the cold mass is estimated to weigh 4,000 kg. The 14 supports utilize a stud in a threaded housing to adjust the vertical position, and a spherical washer at this location aids in alignment and prevents slip in the axial or transverse direction. A cross-sectional view of the supports and rail are shown in Figure 1.33. The lower plate of the cavity support mounts in the recessed portions of the strongback. Due to the rigid connections to the vessel, the strongback is maintained at 300K to prevent contraction-induced stress. The strongback is made from SS316L due to its high stiffness and low magnetic interference, and the supports are primarily made from SS316L and Si-Brz for the same reasons. Multiple materials are used for the supports to prevent cold-welding of the components within the high vacuum environment.



Number	Component	Material
1	Section Connection	All SS316L
2	Cavity Support Mount	
3	Strongback Support Mount	
4	Wheel for Rails	

Figure 1.31: Strongback

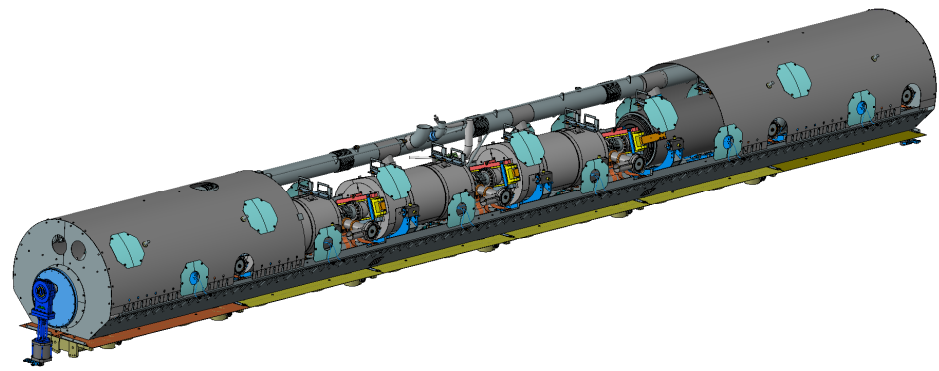
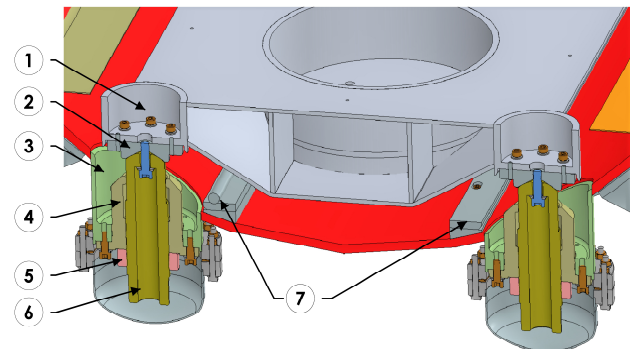


Figure 1.32: Cold Mass

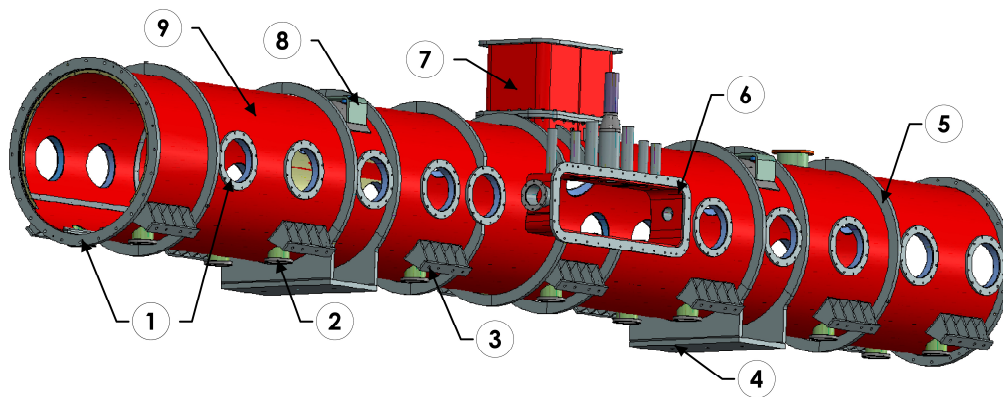


Number	Component	Material
1	Support Mount	SS316L
2	Spherical Cone	Si-Brz
3	Weldment Mount	SS316L
4	Stud Housing	Si-Brz
5	Lock Nut	Si-Brz
6	Stud	SS304
7	Rail System	SS316L

Figure 1.33: Strongback Supports

## Vacuum Vessel

The primary function of the vessel is to allow for an insulating layer of vacuum between the internal components and exterior environment. Any lifting or transportation equipment used for the cryomodule directly interfaces with the vessel. Access ports allow for adjustment of equipment, and configuration adjustments for transportation. The chimney is a removeable section that contains the heat exchanger and pressure relief line. Only the main tube of the vessel is made from A516 steel, which is due to the difficulty and expense of procuring it as stainless steel. All other components of the vessel are made from stainless steel. During installation of the cold mass, the strongback rolls on a rail system affixed to the vessel. It is then connected rigidly at 14 locations to the vessel via the strongback supports. The vacuum vessel is shown below in Figure 1.34.



Number	Component	Material
1	Cover Flange	SS316L
2	Strongback Mount	
3	Transport Mount	
4	Operations Mount	
5	Stiffener	
6	Side Port	
7	Chimney / Top Port	
8	Lifting Point	
9	Main Shell	A516 Steel

*Figure 1.34: Vacuum Vessel Components*

## 1.5 Design Requirements

Based on previous cryomodule transport experience, the following criteria were established by the FNAL Transport Specification for the HB650 [21]:

- Components of the HB650 cryomodule must be designed to withstand 5G axial acceleration, 3G vertical acceleration, and 1.5G transverse acceleration without plastic deformation, and the loads are to be considered separately.
- Critical components, which if damaged would lead to significant project setback, shall not have resonant frequencies below 20 Hz as installed in the transport configuration to mitigate fatigue failure.

These criteria contrast with the design specifications set out for the transportation frame which allow a maximum 3.5G axial, 2.5G vertical, and 1.5G transverse acceleration to the cryomodule. The frame is also required to have 80% isolation above 10 Hz [11]. This built-in factor of safety will help to further mitigate the risk of failure during transportation.

## 1.6 Thesis Objectives

The objectives of this thesis are the following: perform analysis of the HB650 cryomodule utilizing ANSYS R19.2 and analytical methods, investigate how the response of the system changes as the analysis becomes more complex, identify the controlling variable when the design is not satisfactory to make design improvements, and ultimately confirm the design of the cryomodule meets the requirements detailed in Section 1.5. Any implemented changes must not affect cryomodule operations and must adhere to FNAL guidelines.

Chapter 2 details the methods utilized and lays a framework for how the FEA models were built and simplified from their true geometries. The chapter also discusses challenges faced during

this process and how they were addressed. In Chapter 3, the model and analysis of each subsection of the cryomodule are presented. Justification for boundary conditions are given, along with discussion of results. Chapter 4 details the combined analysis of the cryomodule, in which successive components are added and reanalyzed until the model is complete. Discussion of how the response changes with each iteration is included, along with the results of the analysis. Chapter 5 includes the results summary and future work.

## 2. METHODS

The purpose of this chapter is to establish the analysis methods used to produce the results presented in Chapters 3 and 4. This chapter will also address the specific techniques used to overcome challenges of the FEA.

To validate the HB650 design for transportation, the cryomodule was first separated into subassemblies suitable for detailed analysis. The subassemblies are those elaborated in Chapter 1, which include the B90 cavity, B92 cavity, coupler, tuner, supports, two-phase pipe, heat exchanger, cooling lines, strongback, thermal shield, magnetic shield, and vessel. Once each subassembly was analyzed in detail, the models were simplified somewhat and then combined into larger assemblies. These assemblies included the sections of the cavity string which included the cavity, tuner, coupler, and supports; the entire cavity string with two-phase pipe, the strongback and vessel; and finally the full cryomodule. This method is illustrated in Figure 2.1.

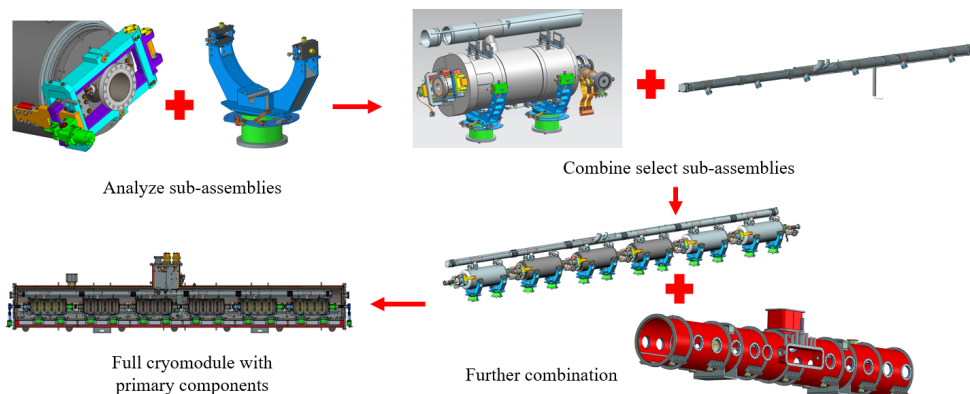


*Figure 2.1: Analysis Methods Pictorial Representation*

## 2.1 Analysis Procedure

Shown in Figure 2.2 is a flowchart detailing the general analysis procedure. Further details of each step and a relevant example are given in each of the following subsections.

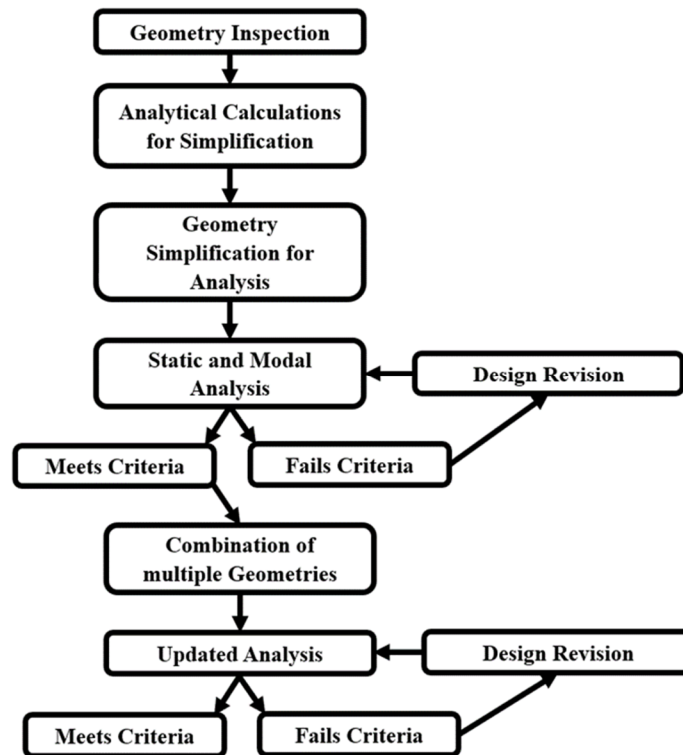


Figure 2.2: Methodology Flowchart

### 2.1.1 Geometry Inspection

To conduct an accurate analysis, an in-depth understanding of the components was required. Most of the necessary information was taken from Teamcenter™ and NX™, which are the lifecycle and CAD software that Fermilab uses. Teamcenter™ stores the CAD files for components and assemblies, drawings for manufacturing, prepared reports, and any other relevant technical documentation. Special attention was paid to the interfaces between components, as this would be important for simplification later. In addition to understanding the physical properties

and interfaces of the cryomodule components, their purpose and function must also be understood. Without this the analysis could neglect important features, and any redesign could overlook intentional choices.

Shown in Figure 2.3 is the cavity needle support, previously discussed in Chapter 1. For each step of the analysis procedure, relevant information and calculations regarding the needle support will be presented as an example. The description of the needle support in Chapter 1 will not be restated. Further analysis in Chapter 3 will discuss the calculations and simplifications made for each subassembly, but the level of detail will be limited due to their extensive nature.

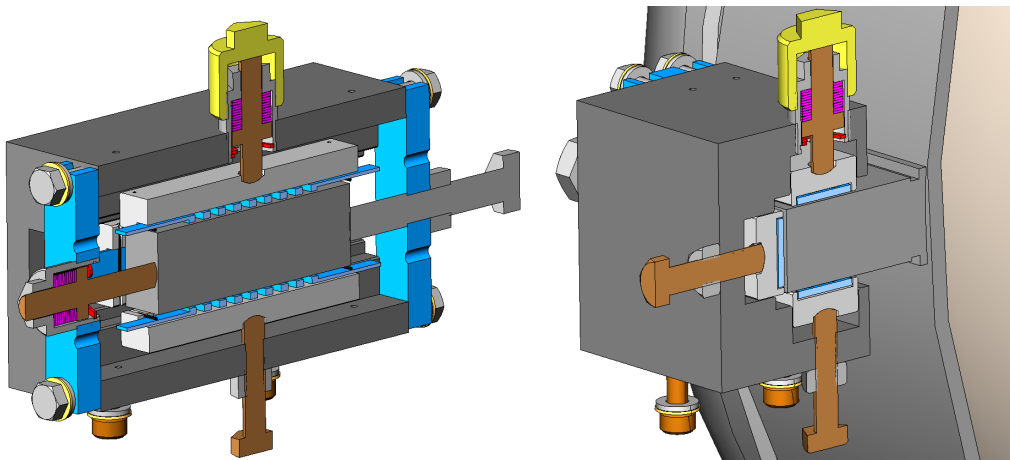


*Figure 2.3: Cavity Lug Support | Left: Transverse Section View | Right: Axial Section View*

### **2.1.2 Analytical Calculations**

The primary purpose of the analytical calculations was to validate the simplifications made for analysis. While it would be ideal to also predict the response of the system, such methods do not lend themselves easily to complex geometry, and so predictions of response were limited. Fasteners were most often checked, as they do not lend themselves well to FEA, but can be readily

evaluated with analytical methods for conditions such as shear or tensile yield. For brevity, all detailed calculations are in Appendix A, but key findings will be presented for each subsection.

In addition to analyzing all bellows for stress and maximum deflections, they were also checked for their expected fatigue life given the maximum displacements due to transportation loads. These displacements were taken from the FEA, and the calculations were performed in accordance with the 2015 American Society of Mechanical Engineers Boiler and Pressure Vessel Code, Division 1, Appendix 26, on bellows expansion joints [22]. MATLAB® was used to perform the calculations, but as this material is copyrighted, no equations or figures can be shown. The calculations have an included factor of safety of three for the number of cycles to fatigue failure. While FNAL also has their own calculation spreadsheets to determine the expected fatigue life, at the time of this work they were under revision and thus could not serve as a comparison.

The minimum allowable cycles were estimated by assuming the cryomodule would see one set of maximum loads per minute for every minute of active transport to and from STFC, or 4,800 maximum loads cycles. This is a rather conservative estimate, as in reality these maximum shocks are very seldom seen. As the components will be designed against low-frequency resonance, and the frame will damp any high-frequency shocks, resonance was not considered. However, once a system is taken to its maximum displacement, it will oscillate until the energy is damped by the flexed components, and so more than 4,800 cycles should be expected.

From discussion with FNAL staff, it was expected that any high-deformation movement would be damped out within 5-10 cycles, but due to the high uncertainty of this estimate, it was assumed the components would oscillate for 50 complete cycles with maximum amplitude. More detailed estimates of this behavior could not be made due to a lack of experimental data and inability to

model components with accurate damping factors. From these estimates, the minimum allowable fatigue life was determined to be 240,000 cycles for the bellows. As this value included several conservative estimates, and the calculated fatigue life has an FOS of three, the estimate of 240,000 cycles was thought to have an acceptable safety margin for the expected scenario.

For the case of the needle support, it was assumed that the screws and bearings support negligible shearing forces and thus could only be loaded in compression. Generally, a fastener will yield in tension or compression before the threads yield due to the ratio of the shear and tensile areas. For verification, this is demonstrated below. Shown is the evaluation of the vertical bolt which supports the weight of the cavity. Equation 1.1 illustrates that, as originally designed, the bolt sizes were insufficient for the expected loading conditions, and the sizes have since been adjusted to a more suitable M8.

$$\sigma = \frac{F}{A} \quad (1.1)$$

$$\text{Max Force} = 300 \text{ Kg Cavity Mass} * (3G + 1G) * 75\% \text{ load on one support} * \frac{1}{2 \text{ Bolts}} + \\ 1,500 \text{ N Tightening Force}$$

$$F_{max} = 6,000 \frac{N}{bolt}$$

$$SS316L \text{ YS} = 170 \text{ MPa} \mid \text{Shear YS} = 170 \text{ MPa} * 0.57 = 96.9 \text{ MPa}$$

$$M6 \text{ Area}_{\text{Thread Shear}} = 8.7 \frac{\text{mm}^2}{\text{mm}} * 9 \text{ mm thickness} = 78.3 \text{ mm}^2$$

$$\sigma_s = 76.6 \text{ MPa} < 96.9, \text{ PASS}$$

$$M6 \text{ Area}_{\text{Tensile}} = 20.1 \text{ mm}^2 \mid \sigma_T = 223.9 \text{ MPa} > 170 \text{ MPa}, \text{ FAIL}$$

### 2.1.3 Geometry Simplification

All geometry was created from scratch in ANSYS® Design Modeler™ since it allowed for direct control of the geometry, and changes were more readily made. Additionally, the CAD files from NX™ would sometimes have very slight imperfections that would greatly affect the mesh quality. The following is a list of the general guidelines used to simplify the geometry for analysis:

- Remove fasteners and welds
- Fill small holes, delete chamfers and fillets
- Make thin components as surfaces for shell meshing
- Combine parts into single bodies as appropriate, such as for welded assemblies
- Create detailed names for all parts

For the needle support, two separate geometries were evaluated: a detailed model and a simplified model. This was done to ensure a simplified model could accurately capture the behavior of the original connection. A comparison of the geometries is shown in Figure 2.4 and Figure 2.5. The detailed model includes no-separation (sliding) contacts between the bearings and lug, bolts which are combined with the needle block, bonded contacts from the bolt tips to the lugs, and no-separation contacts from the bolt tips to the bearings. The simplified geometry utilized a joint between the lug and the needle support to form a connection, and it had six degrees of freedom (DOF), which can be toggled as fixed or free, that include displacement and rotation. Only the rotation about the transverse axis was allowed, and a torsional spring with experimentally determined stiffness was attached from the lug to the support to mimic the resistance of the bolts to rotation.



Figure 2.4: Detailed Support Model | Left: Transverse Section View | Right: Axial Section View

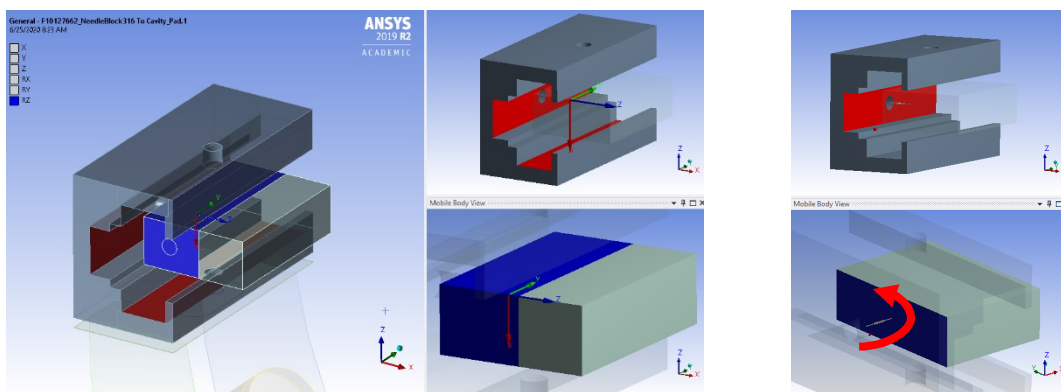


Figure 2.5: Simplified Support Model | Left: Joint Connection | Right: Torsional Spring

### 2.1.4 Analysis and Design Revision

The software used was ANSYS® Mechanical™ 2019R2, and the modules used were Static Structural and Modal. Static structural analysis was used to apply either a 5G, 3G, or 1.5G static acceleration to the subassembly to determine maximum stresses and deflections, while modal analysis was used to find the resonant frequencies. The accelerations were checked in both positive and negative directions to determine the scenario with the highest stresses. The decision to use

static structural and modal analysis was made based on the research discussed in the background Section 1.4.2.

Subassemblies that did not meet the stress criteria or that displayed low resonant modes had their design modified, and the changes were verified with FNAL engineering staff for sound design. Subassemblies that were used in the combined analysis received additional simplification after initial detailed analysis for the purpose of reducing the overall mesh size. The simplified and detailed analyses were then compared to ensure similarity. If the stress was determined to be of little concern, significant simplifications were allowed (see Section 3.2 Tuner). If stresses were still of concern, either the detail would remain (such as for the cavities) or another method would be found to allow for simplification while still having the ability to infer stresses (see section 3.1 Coupler). If available, the results were compared to previous results from FNAL engineering reports. Mesh refinement studies were performed to ensure converged results.

The detailed and modified needle bearing supports were tested using the models shown in Figure 2.4 and Figure 2.5. With the detailed analysis serving as a baseline, iterative tests of the simplified model were performed until the response was nearly identical. The response metrics included stress in the supports, maximum deflection, and mode frequencies of the system. As the exact methods and results are rather detailed, they will not be repeated in this section, but instead can be found in Section 3.5.

### **2.1.5 Combined Analysis**

For the combined analysis, the primary subassemblies were the following: each section of the cavity string which consisted of a B90 or B92 cavity, tuner, coupler, bellows and supports, the two-phase pipe, strongback, thermal shield, and vessel. Multiple copies of the string sections were

created, for six in total. By combining their models, this ensured the same mesh and connections would be retained for each copied subassembly and reduced the repeated setup work. The only setup required in the combined models was to create contacts between subassemblies and to apply the boundary conditions such as fixed locations and loads. Results of each combined analysis were compared to those of the previous subassembly analysis. The Workbench™ tree structure is shown in Figure 2.6.

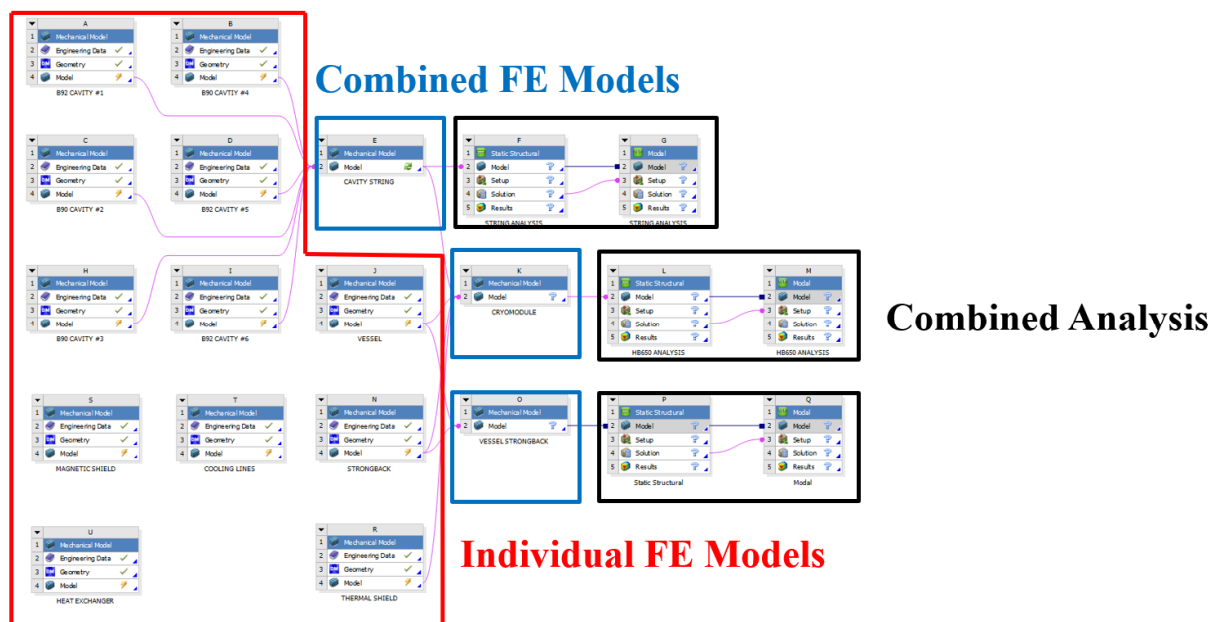


Figure 2.6: Workbench™ Model Combination Methods

## 2.2 FEA Techniques

This section serves to document some of the challenges which arose during the FEA and the techniques and studies used to address them with the goal of assisting those performing similar work in the future.

### 2.2.1 Mesh Generation

It was important to limit the number of nodes in the mesh for each subassembly; otherwise, the combined analysis would be too computationally expensive. Shell mesh was used for thin components such as cavities, piping, bellows, etc. Quadratic quadrilateral elements were used, as they were found to produce the most converged results with the fewest nodes. As appropriate for welded or otherwise rigidly connected bodies, the parts were made to share topology, which created a continuous mesh between them. Bodies that did not share mesh had their nodes aligned for optimal contact detection. Solid mesh, while seldom used, was employed with a swept quadratic mesh if possible, or a quadratic hexahedral mesh otherwise. Swept mesh is only available for solids without a shared mesh, which prompted further component combination. Similarly, beam elements were rarely used but proved useful in reducing the mesh size of bodies like the cooling lines and Invar rods.

To further reduce the mesh size, subassemblies were first analyzed with fine mesh and detailed geometry and afterwards were simplified to have a coarser mesh, but the same overall response was maintained. An example of this simplification and response validation has been given for the needle support, and further examples can be found in Chapters 3 and 4.

Initial attempts were made to eliminate the need for the bellows geometry and to instead use bushing elements. These elements are defined by three directional stiffnesses and three rotational stiffnesses. However, issues producing reliable results for modal analysis, and the need to submodel the bellows, thwarted this effort. Instead, a coarse mesh that still produces accurate results was developed and is shown in Figure 2.7. A comparison of the transverse stiffness to a unit displacement is shown in Figure 2.8, with 80 N/mm being the stiffness prediction from theory.

All mesh was quadratic order, with tetrahedral and quadrilateral being automatically generated with a body sizing while the final mesh placed controls on the number of divisions on the circumferential divisions along the bellows.

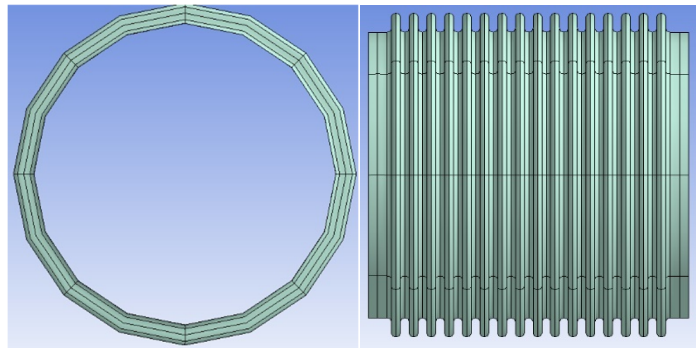


Figure 2.7: Final Bellows Mesh

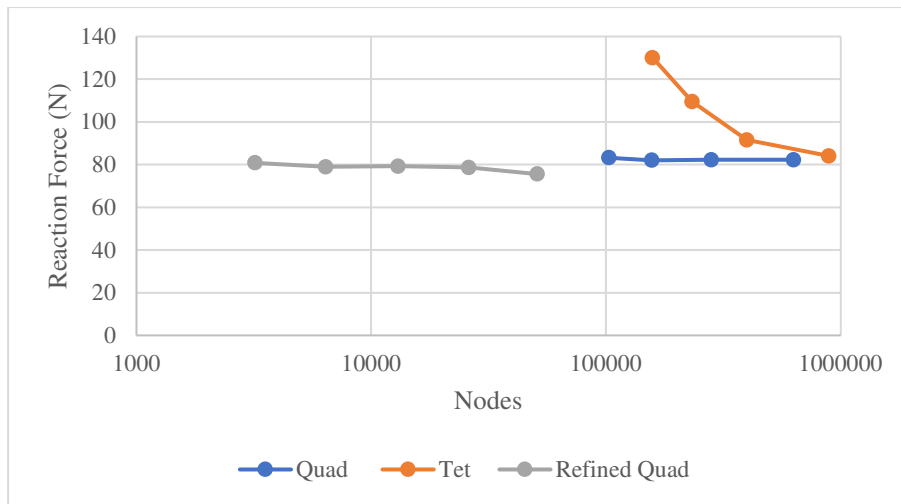
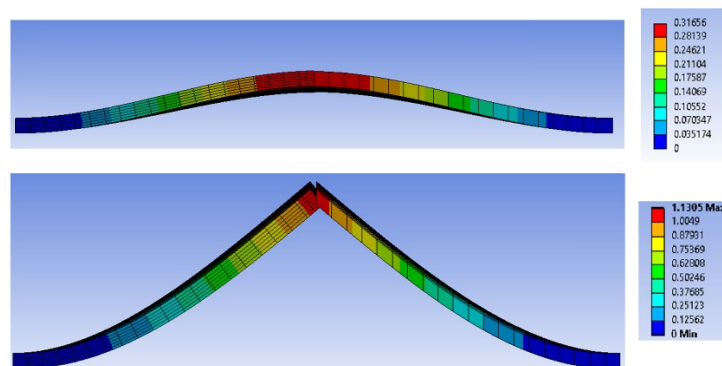


Figure 2.8: Bellows Mesh Convergence Comparison

### 2.2.2 Connections

Due to the formulation of solid elements, their only supported DOF are X, Y, and Z displacement (UDOF). Unlike shell elements, there are no rotational DOF (RDOF) to constrain the elements. If incorrect connections are made at shell-solid interfaces, then rotation between the bodies will be unconstrained and the response will be inaccurate. To remedy this, different methods of connecting shell and solid bodies were tested using a model of two plates butt-welded together, where one was shell and one solid. A force was applied normal to the plates along their connecting edge. The results were compared against a baseline of a fully solid model. The most accurate and readily implemented solution was to set the shell edge as the target, set the face of the solid as the contact, and change the formulation to multipoint constraint (MPC). Figure 2.9 compares the deformation of the MPC contact and the automatically generated contact.



*Figure 2.9: Solid-Shell Contact Comparison | Top: MPC | Bottom: Automatic*

Other connection methods included the use of joints to model complex behavior between two bodies, as the UDOF and RDOF can be individually locked or freed. Such joints were used

between the Invar rods and their guides and the cavity lugs and the needle supports. For contact generation, the contacts were created both manually and using connection groups. The contact tool proved to be invaluable for ensuring closed-contact statuses.

### 2.2.3 Modal Analysis

The primary challenge of the modal analysis was that the solution must be linear due to the need for eigenvalue solutions [23]. This applies limitations to connections such that only bonded and no-separation contacts are allowed, and joints are also allowed. Contacts which can change status from open to closed – such as a frictional contact – are not allowed. There are several cases where this becomes problematic, such as for the cooling lines. A support at one end of the cooling line prevents negative axial movement but does not prevent positive axial movement. Accurate modal analysis of this is not possible and instead two cases were tested: with the contact closed and with the contact open. The true axial resonant frequency should lie between these two sets of results. The cooling line and support are shown in Figure 2.10.

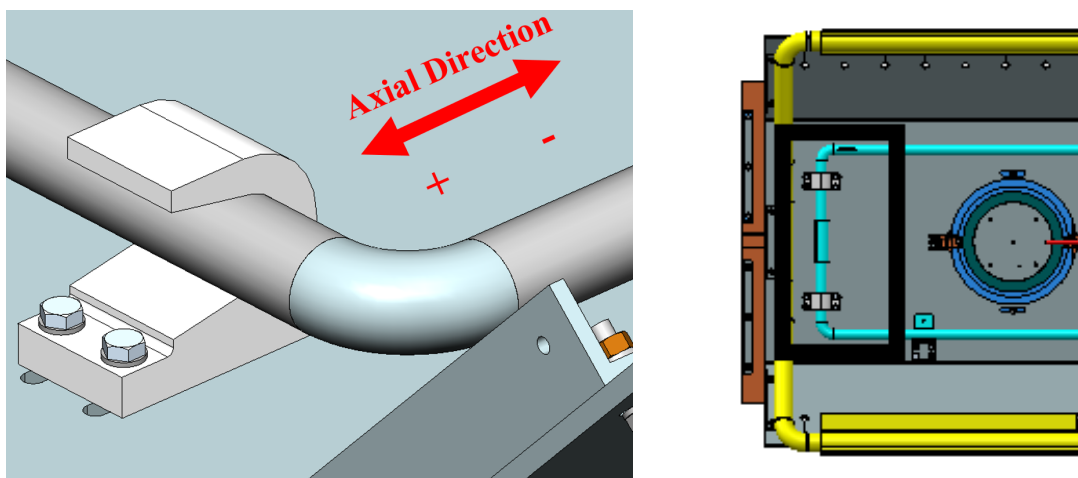


Figure 2.10: Left: Cooling Line Support | Right: Support Location

### 3. SUBSYSTEM ANALYSIS AND RESULTS

The purpose of this chapter is to detail the analysis and results of each subassembly within the cryomodule. Each section includes the following: boundary conditions, meshing methods, assumptions, analytical calculations, modal and structural results, issues found and design changes made, and model simplifications made for the combined analysis presented in Chapter 4.

#### 3.1 Coupler

The coupler required some simplification for analysis. Bolts connecting flanges were replaced with a bonded contact between the faces; heavy gauges and thermal strap cables were replaced with point masses. A fixed constraint was placed on the flange that mounts to the beamline. Bonded contacts were used throughout the model, and primarily solid mesh was used, with shell mesh for only the antenna tubes, vacuum tube, and thermal strap blocks. The mesh contained 266K nodes and 50K elements, and the mesh and boundary conditions are shown in Figure 3.1 and Figure 3.2, respectively.

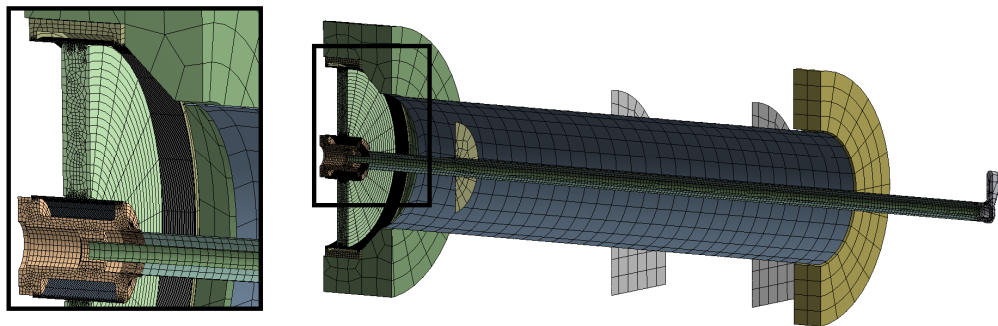


*Figure 3.1: Coupler Mesh*

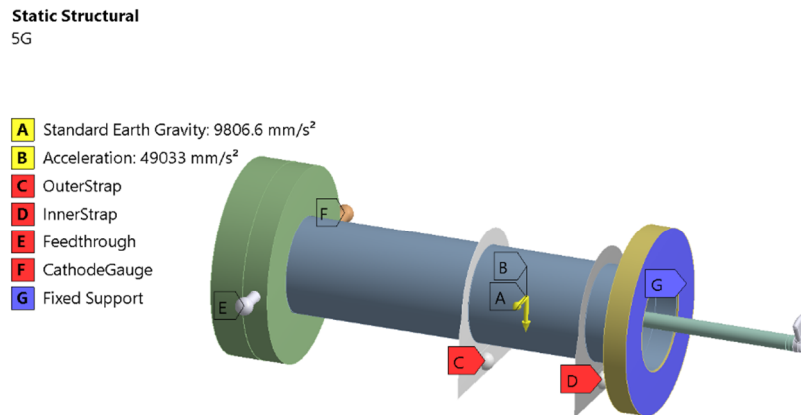


*Figure 3.2: Coupler Boundary Conditions*

Modal analysis did not highlight any issues with the coupler. The first mode occurred at 37 Hz with the antenna moving transverse to its central axis. This is in close agreement with the analytical prediction of 33 Hz, which was made assuming the stiffness of the inner and outer antenna tubes are merely additive and that the constraint of linking their ends does not provide additional rigidity. The calculation is detailed in APPENDIX A. Subsequent modes did not occur until 117 Hz. Previous analysis by FNAL staff found the first mode occurred at 37 Hz [24], which agrees with this analysis, as detailed in APPENDIX B. The first mode shape is shown in Figure 3.3.

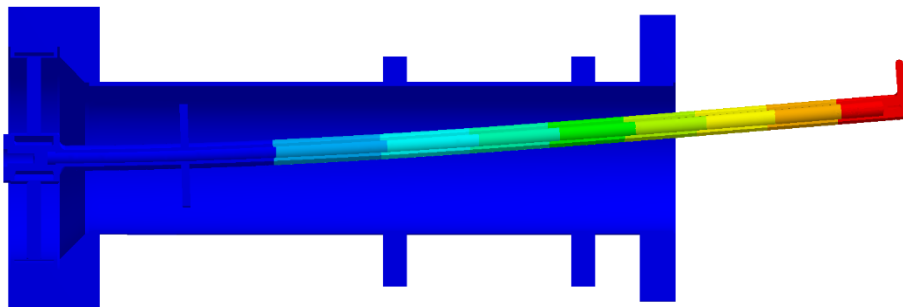


*Figure 3.3: Coupler Mode Shape 37 Hz*

Structural analysis did not find any issues with the coupler. The highest stresses were due to 5G at the copper connector, with 31 MPa stress, which is well below the allowable stress. This is shown in Figure 3.4. The tip saw a 1.30 mm deflection in the axial direction. A singularity did exist at the contact between the outer tube and the connector, which was likely due to the attachment of shell to solid elements. Previous analysis by FNAL staff, as shown in APPENDIX B, used entirely solid mesh and saw no such singularities. The previous analysis found the maximum stress to be slightly lower at 25 MPa, and the tip deflection was slightly higher at 1.35 mm [24]. The small differences were likely due to subtle variance in the model and different meshing strategies.

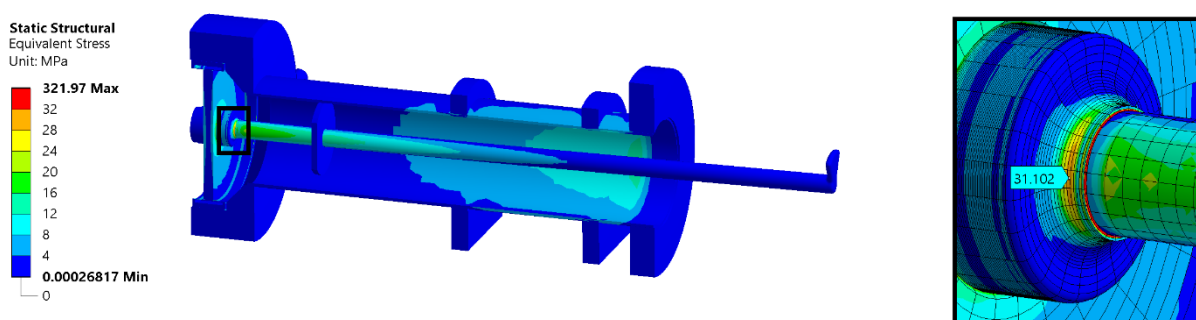


*Figure 3.4: Coupler 5G Stress*

The simplified model had the following changes: solid components such as the ceramic window were replaced with surfaces, the antenna tubes were replaced with beams, the disc and antenna tip were replaced with point masses, and the copper connector was greatly simplified. A joint between the two tube tips fixes their displacement and rotation, as would their shared contact to the antenna tip. While the stress at the connector is not expected to change in the combined

analysis, this simplification prevents the accurate stress from being known. However, since the antenna behaves similarly to the detailed model, and the deflection of the antenna linearly corresponds to the connector stress, it should be acceptable to use the antenna deflection as an indicator of the stress in the combined analysis. A plot of max eq. stress vs axial deflection is shown in Figure 3.5 to illustrate the relationship. The simplified mesh is shown in Figure 3.6 and contains 5.5K nodes and 1.4K elements.

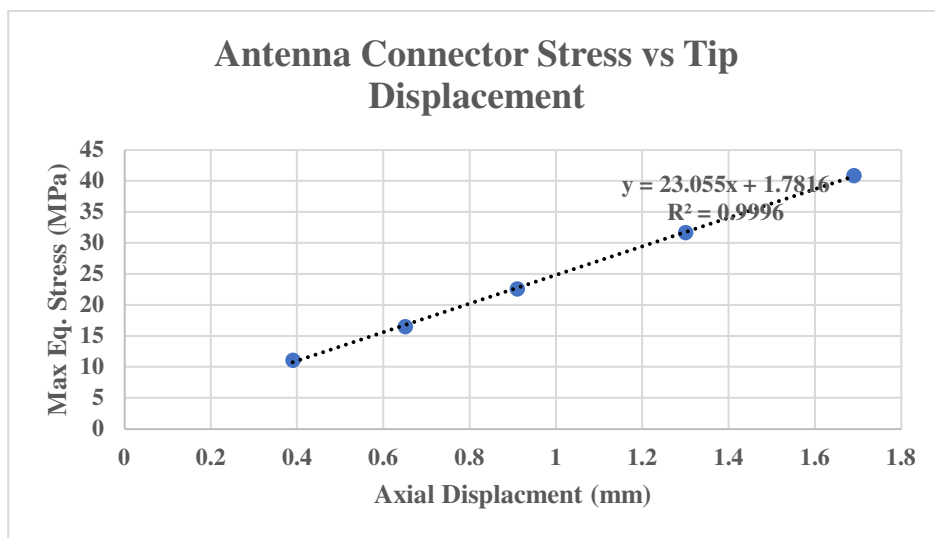
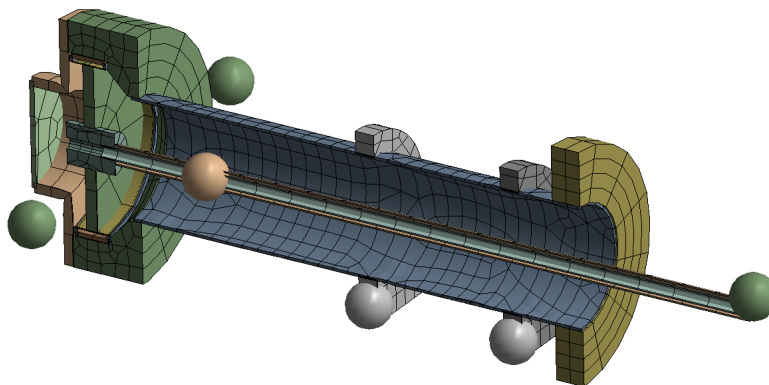


Figure 3.5: Connector Stress vs Axial Displacement



*Figure 3.6: Coupler Simplified Mesh*

The results of the simplified analysis closely matched the detailed analysis. The first mode was still 37 Hz, and successive modes matched within 5%. The axial deformation at the end of the outer tube was 1.18 mm, which is 7% less than at the same location in the detailed model. As the stress can be inferred from the displacement, this small difference was not of concern.

### 3.2 Tuner

Significant simplifications were made to the tuner for analysis, which include the following: the piezo was removed, the stepper motor was replaced with a 4 kg point mass and a simplified solid connector, bearings with revolute motion were replaced with joint connections, and the ceramic ball pivot was replaced with a joint connection. As the ceramic ball pivot is very stiff, it was modeled as a fixed joint. The faces of the arms that connect to the cavity lugs were given a fixed condition. The coordinate system was rotated by 20 degrees for the applied loads, as the tuner is mounted to the cavities at this angle. Entirely solid mesh was used, and the model had 228K nodes and 51K elements. As the B90 and B92 cavities require different tuners, both were checked. The only difference is the length of the arms that attach to the lugs, and so only results and figures will be shown for the B92 tuner, as it had lower resonant frequencies and higher stresses due to the longer arms. Boundary conditions and the mesh are shown in Figure 3.7.

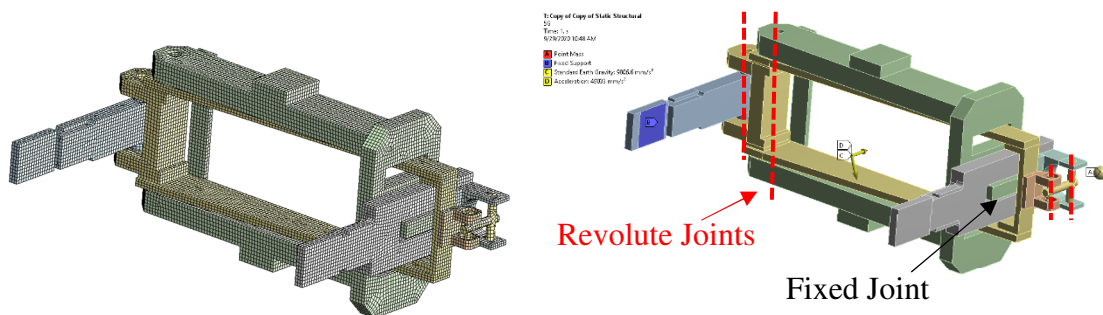


*Figure 3.7: Tuner Model | Left: Mesh | Right: Boundary Conditions*

Modal analysis did not highlight any issues; the first mode was at 80 Hz with transverse motion, and the second mode of 117 Hz displayed vertical motion. The mode shapes are shown in Figure 3.8. Previous analysis was not available for comparison.

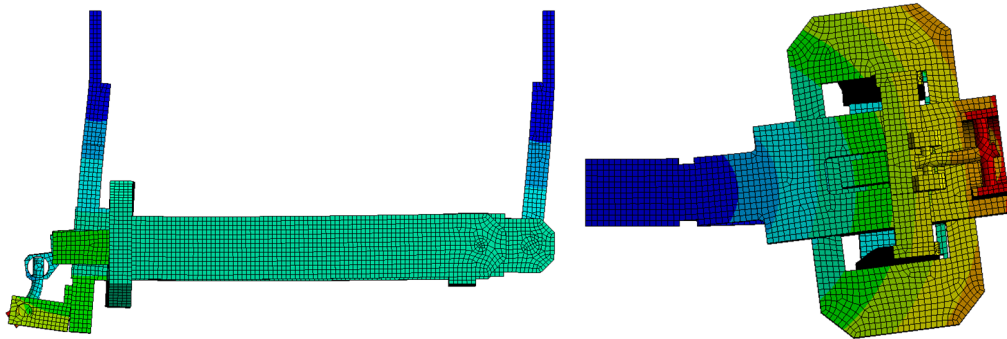


*Figure 3.8: Tuner Mode Shapes | Left: 80 Hz Top View | Right: 117 Hz Side View*

Structural analysis did not highlight any issues with the tuner (Figure 3.9). The highest stresses were seen during 3G with 90 MPa at the supporting arm. Given that this was well below the 205 MPa yield strength and located at a sharp internal corner in the mesh, it was not a concern. Previous analysis was not available for comparison.

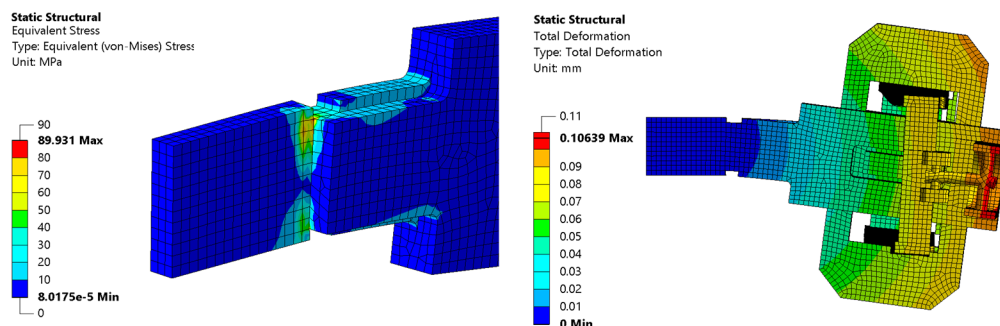


*Figure 3.9: Tuner Structural Results | Left: Stress | Right: Total Deformation*

Further simplification of the tuner combined the inner and outer arms, removed the revolute joints, and made the mesh very coarse, as shown in Figure 3.10, with only 10K nodes and 2.2K elements. This was done with the knowledge that it would not have the same modes or stresses when analyzed as a subassembly. However, since the tuner met all requirements easily, so long as the simplified model induces the same response in the combined analysis as would the detailed model, then the simplification is justified. The same overall mass and center of gravity were maintained as before.

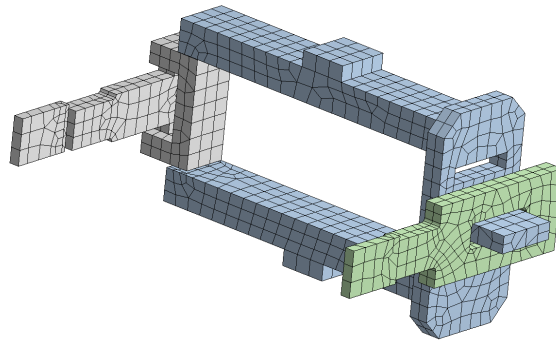


*Figure 3.10: Simplified Tuner Mesh*

For completeness, the results of the simplified model were the following: the first resonant mode was 108 Hz, the second 133 Hz, and the highest stress was 64 MPa at the same location as before due to 3G. The increased stiffness and reduced stress were due to the coarse mesh, component combination, and removal of revolute joints. A comparison of the response for a fully dressed cavity with the detailed and simplified tuner was later performed, which confirmed the aforementioned hypothesis that the response of the combined system would not change significantly due to the tuner simplification.

### 3.3 B90 Cavity

Simplifications to the B90 cavity were standard, with solid components merged, thin features made as surfaces, and bolted connections replaced with bonded contacts. Primarily shell mesh was used, but swept solid mesh was also used. Bonded contacts were used throughout the assembly. The lugs were given a fixed constraint, as they are constrained by the supports. Two springs with stiffness of 20 kN/mm were each attached from the piezo contact points on the split ring to the tuner lugs to simulate the axial tuner stiffness. The stiffness value came from experimental testing of an assembled tuner [19]. Similar boundary conditions were used in previous analysis by FNAL staff and allow for an accurate comparison of results. The mesh contained 35K nodes, 10K elements, and is shown in Figure 3.11 along with the boundary conditions.

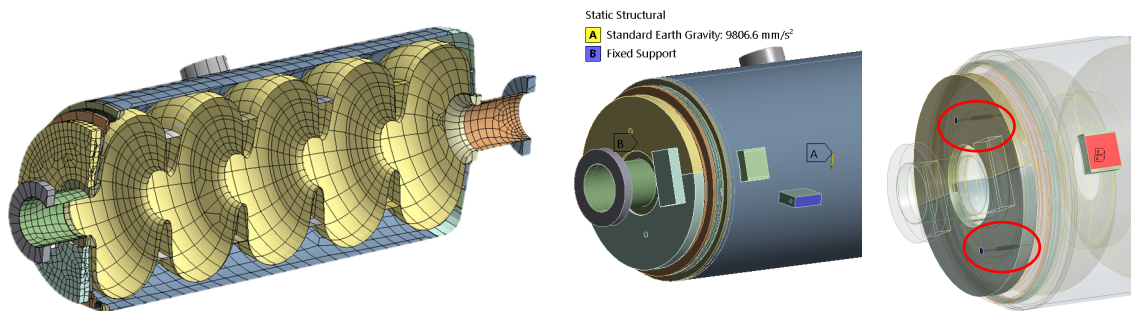
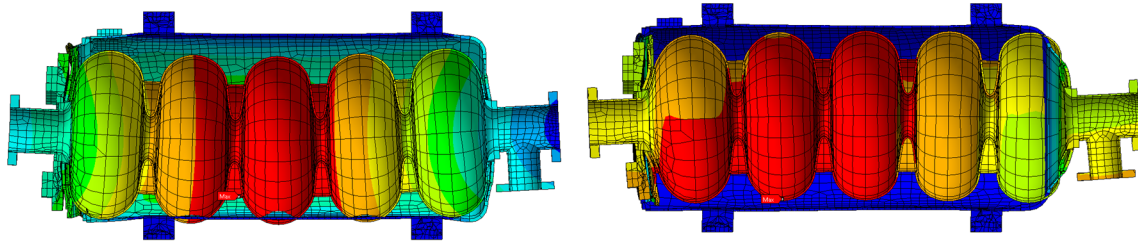


Figure 3.11: B90 Model | Left: Mesh | Center: Fixed Constraint | Right: Tuner Springs

Modal analysis did not highlight any issues. The first mode of 73 Hz saw the transverse movement of the cells and jacket, the second mode of 91 Hz saw the vertical motion of the cells, and the first axial mode occurred at 121 Hz. These results are in fairly strong agreement with previous FNAL analysis (shown in APPENDIX B), with the exception of the first transverse mode. Previously, a half-symmetry model was used, which constrained this movement and

artificially increased the transverse resonant frequency to 100 Hz. This was confirmed by placing similar constraints on the model created for this thesis. The axial resonance matched within 1% [25]. The mode shapes are shown in Figure 3.12.



*Figure 3.12: B90 Mode Shapes, Section View from Above |Left: 73 Hz |Right: 121 Hz*

Structural analysis did not highlight any issues (Figure 3.13). The highest stress in the titanium bellows was 52 MPa due to 3G, and the most stress in the niobium cells was 10 MPa due to 5G, which are both within their respective yield limits. The bellows saw a maximum transverse displacement of 0.05 mm due to 3G and a maximum axial displacement of 0.08 mm due to 5G, which are well below the 0.2 mm allowable. Previous analysis (see APPENDIX B) found the maximum bellows stress to be 24 MPa due to 3G. The difference was likely due to the use of a very fine solid mesh, with three elements through the thickness of the bellows [25], which tends to give the most accurate results. Given these results, the maximum stress was deemed acceptable.

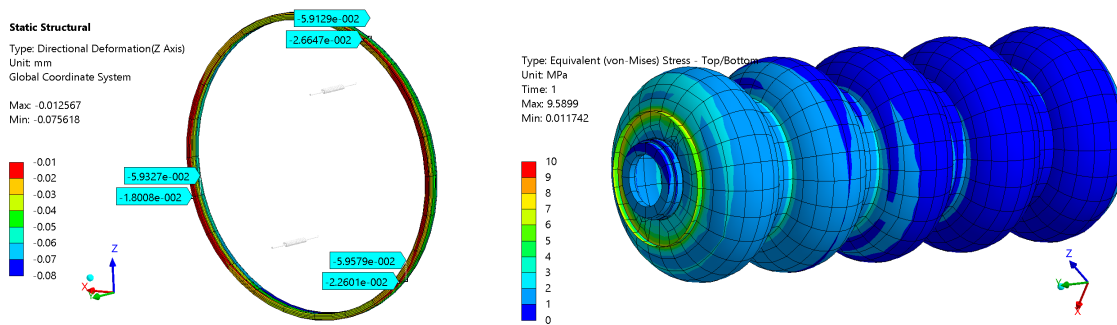


*Figure 3.13: B90 Cavity Structural Results | Left: Bellows Transverse Displacement 3G | Right: Niobium Cells Stress 5G*

No further simplification to the B90 cavity was made as the model had a sufficiently low node count, and the response was expected to change with the addition of the tuner and other components. As such, the detailed model was required to obtain accurate results.

### 3.4 B92 Cavity

The simplifications, meshing strategies, and boundary conditions for the B92 model were nearly identical to that of the B90, and therefore will not be repeated. The mesh contained 25K nodes and 7K elements and is shown in Figure 3.14.

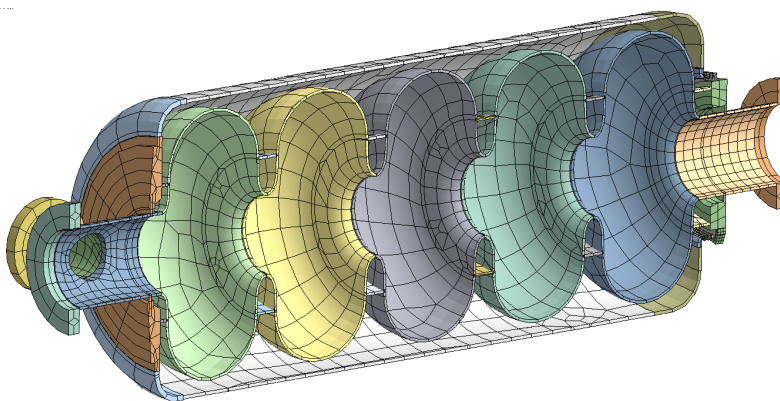


*Figure 3.14: B92 Cavity Mesh Section View*

Modal analysis did not highlight any issues. The first mode of 52 Hz saw the transverse movement of only the niobium cells, which differs from the B90. The frequency was lower as the smaller B92 bellows has a lower transverse stiffness. The mode which saw a transverse movement of the jacket and cavity did not occur until 113 Hz, compared to 73 Hz for the B90, which is explained by the lack of the heavy split ring. The first axial mode occurred at 115 Hz, which was similar to that of the B90, as it was largely dependent on the tuner stiffness. The mode shapes are shown in Figure 3.15. These results are in fairly strong agreement with previous FNAL analysis (shown in APPENDIX B), which found the first transverse mode as 48 Hz and the first axial mode as 103 Hz [26]. As the high-frequency response is not of great interest for transportation, the 12% difference was not of great concern.

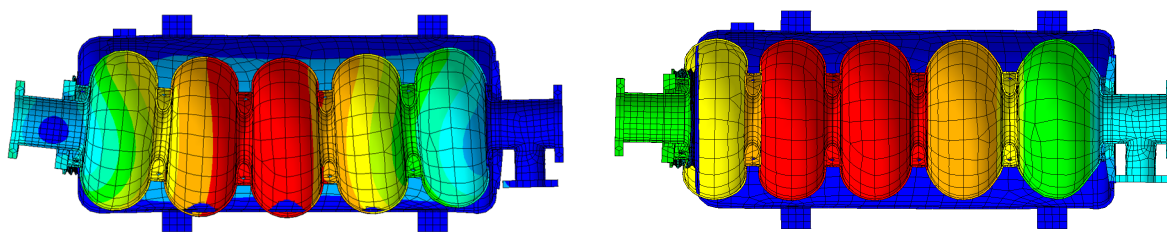


*Figure 3.15: B92 Mode Shapes, Section View |Left: 52 Hz |Right: 115Hz*

Structural analysis did not highlight any issues. The highest stress in the titanium bellows was 83 MPa due to 3G, and the most stress in the niobium cells was 24 MPa due to 3G, which are both within their respective yield limits. The bellows saw a maximum transverse displacement of 0.06 mm due to 3G and a maximum axial displacement of 0.09 mm due to 5G, both within the allowable limits. The transverse bellows displacement and niobium cells stress are shown in Figure 3.16. Previous analysis (see APPENDIX B) with very fine solid mesh found the maximum bellows stress to be 53 MPa. Other results, such as the 3G cavity deformation (not shown), matched within

5% of those determined by this thesis [26]. As the models overall had very similar results, and both stress results for the bellows were below allowable, the results were deemed satisfactory for transportation. No further simplifications were made to the model.

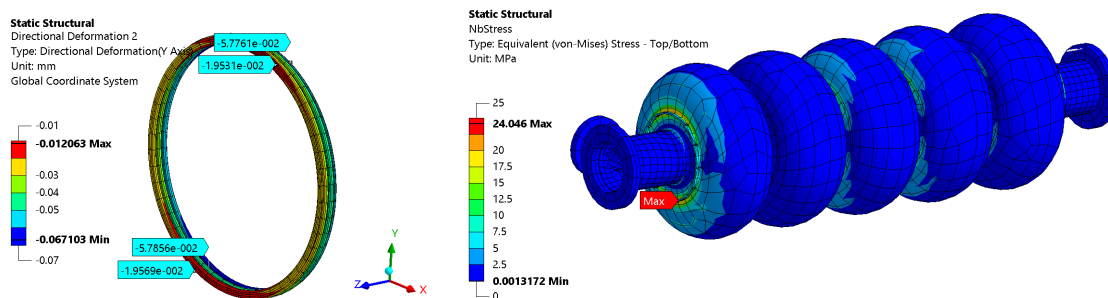
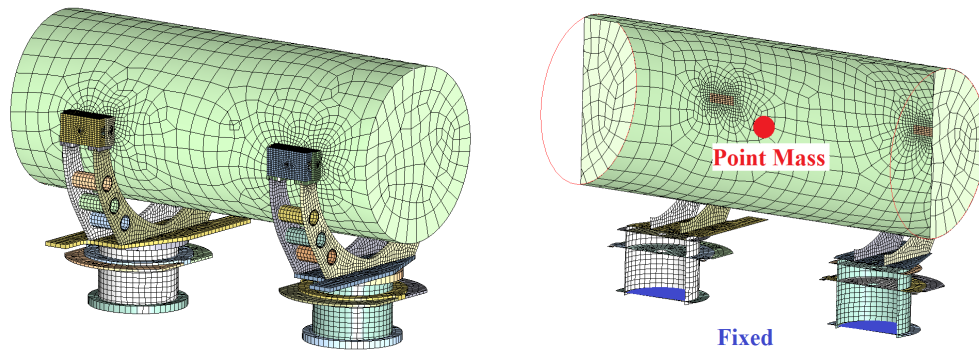


Figure 3.16: B92 Cavity Structural Results | Left: Bellows Transverse Displacement 3G | Right: Niobium Cells Stress 3G

### 3.5 Cavity Supports

Simplifications to the cavity supports included the removal of bolted connections, welds, and shrink fits in favor of bonded contacts and merged mesh. The lower face of the support which bolts to the strongback was given a fixed constraint. The needle supports which connect to the cavity lugs were not simplified at first, and the detailed model was later used for verification of a simplified model. As the behavior of the needle supports could not be accurately determined without the cavity lug, a simplified model of the cavity was used to enable a better analysis while reducing model complexity. The “dummy” cavity mimicked the helium jacket and had a point mass of 260 kg attached to it to accurately represent the mass of all other attached components. Entirely shell mesh was used for the support and dummy cavity jacket, whereas solid mesh was

used for the needle supports and lugs. In total, 169K nodes and 45K elements were used, and the model and boundary conditions are shown in Figure 3.17.



*Figure 3.17: Cavity Support | Left: Mesh | Right: Boundary Conditions*

Before further discussion of the model, analytical calculations made for the needle supports will be discussed. Due to the complexity of the needle support, the geometry is shown in Figure 3.18 as a reference. Detailed calculations are shown in APPENDIX A, and the following paragraphs are a summary of the findings. In total, the weight of the dressed cavity, tuner, coupler, magnetic shield, and attached section of two-phase pipe was 300 kg, which is the effective load a set of cavity supports accepts. This 300 kg value also includes a 10% safety buffer, as the true mass was 270 kg. Based on the geometry of the cavity, in which the heavy tuner was mounted far to one side, it was hypothesized one support would accept considerably more load than the other. An initial estimate of a 60/40% load share was made, and later analysis found it to be 67/33% load share. The analytical calculations have since been updated with the slightly more conservative estimate of 70/30% load sharing.

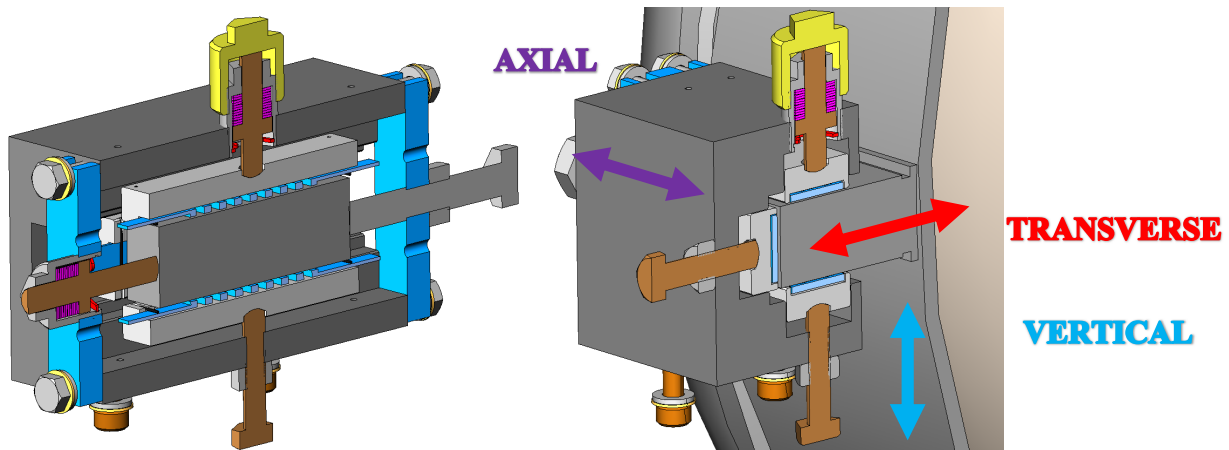


*Figure 3.18: Cavity Lug Support | Left: Transverse Section View | Right: Axial Section View*

During 5G acceleration, only one of the axial bolts on a given needle support accepts the load, as they can only be loaded in compression. This is because there is not a threaded connection, only a contact maintained by the tightness of the bolts. Therefore, the maximum load one bolt accepts is half of 70% of 300 kg at 5G, which is 5,150 N. The tightness of the bolts is additive to the acceleration load, which adds another 1,500 N of force. The original design of the needle support used M6 SS316L bolts to contact the cavity lug and needle bearings, which have a tensile area of 20.1 mm<sup>2</sup>, giving a compressive stress of 331 MPa. This is well above the 205 MPa yield limit, and so the size of the bolt was increased to M10. The sizes of other bolts, which take lesser loads due to 1.5G and 3G, were increased to M8, and the minimum diameter of the spring jacks were increased to 7.6 mm. The minimum FOS was 1.4 for the spring jack during 5G. The bolts at the base of the cavity support and needle block were also evaluated for shear due to 5G, and both saw no issues. More detailed calculations are shown in APPENDIX B.

As previously mentioned, the bearings and bolts that contact the lugs can only support a compressive load, not a tensile load. This is not an issue for 3G or 5G, as there are a set of vertical

and axial bolts to prevent movement. However, for 1.5G, as one side of the support is in compression, the other is in tension, as illustrated in Figure 3.19. The side in tension is only able to support these forces via friction between the lug and the axial bolts/bearings. Initial assumptions were for the best possible case and included the following: each side accepts 50% of the load, the static friction coefficient is 0.20, and the bolt tightness is not significantly lessened by the practice of loosening by ¼ turn from the 53 in-lbf torque specification, as is the tightening procedure. More detailed calculations are shown in APPENDIX B. For these conditions, the lug was found to slip at 1.16 G, which is below the 1.5G threshold. As this had the potential to affect the alignment of the cavity string (which is critical to performance), which must be held to  $\pm 0.25$  mm in the transverse direction, the remaining calculations and analysis were performed using a more complete assembly detailed in Chapter 4.

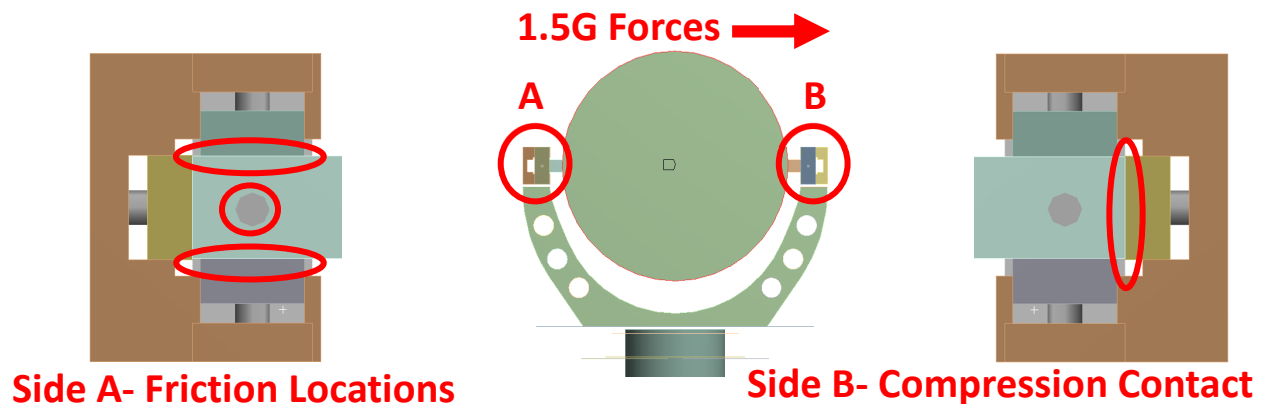


*Figure 3.19: Cavity Support 1.5G Slip Scenario*

While the detailed analysis of the 1.5G scenario is not discussed until Chapter 4, the remaining model boundary conditions and results will be discussed. Each bearing had three primary contact

points: to the bolt/spring jack, to the cavity lug via needle bearings, and to the needle block which acted as a guide. All these connections were modeled as no-separation contacts, which allow for the contacted faces to slide against each other but not separate. The contact from the axial bolt to the cavity lug was given a fixed contact but was evaluated as a sliding contact as well for the case of 1.5G. Figure 3.20 shows the model of the needle support, along with the contact locations. For clarity, only one of each contact type is annotated.

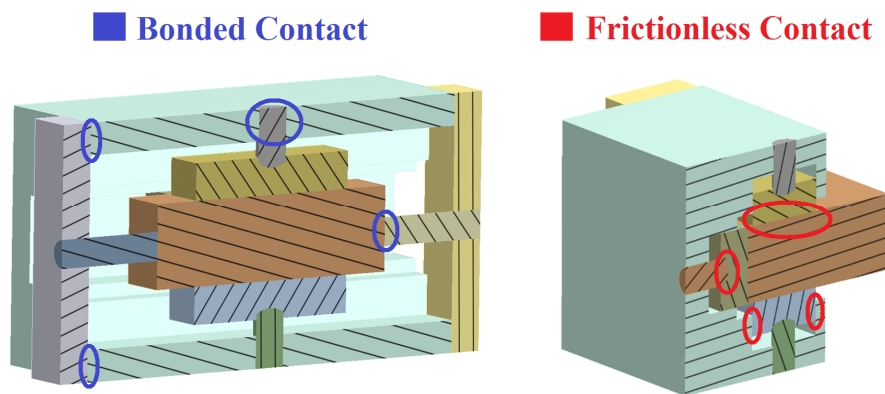


*Figure 3.20: Detailed Needle Support Section Views and Contacts*

Modal analysis of the supports did not highlight any issues. While the supports themselves are not critical components, they support the cavity string, and if the supports had low-frequency modes, it could adversely affect the intercavity bellows. As it was deemed unlikely the cavity would see excitation significant to create a slip condition, and accurate modeling of this behavior is not possible, the contacts at the needle support assumed no sliding in the transverse direction. The first mode occurred at 20 Hz with the transverse movement of the cavity, followed by the axial mode at 21 Hz, and the mode shapes are shown in Figure 3.21. A twisting motion occurred at 72 Hz but is not shown.

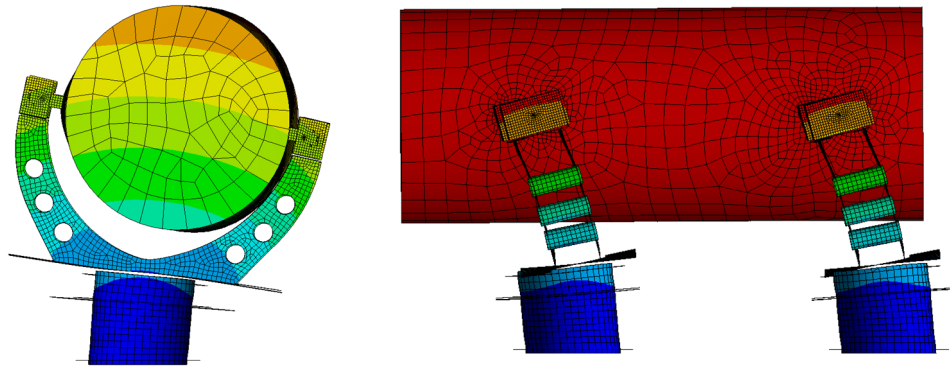


Figure 3.21: Cavity Support Mode Shapes | Left: 20 Hz | Right: 21 Hz

Structural analysis of the supports did not highlight any issues either. The highest stresses observed in the support were during 5G axial, with a maximum of 220 MPa at a sharp corner, but more realistically the maximum was 100 MPa, both of which are below the 275 MPa YS. The axial deflection at the cavity end was 2.67 mm, which is well below the axial extension limit of 10 mm for the beamline bellows. The transverse deflection at the center of the cavity face was 0.97 mm, well below the 3 mm transverse extension limit for the beamline bellows. For the case of 1.5G transverse, analysis was performed to determine the effect of slip on the support. As shown in Figure 3.22, the sliding conditions double the maximum stress within the support, as one side takes the entire load.

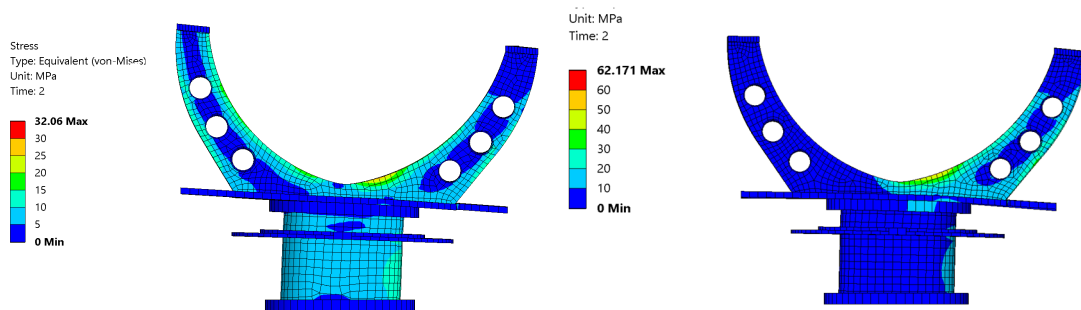
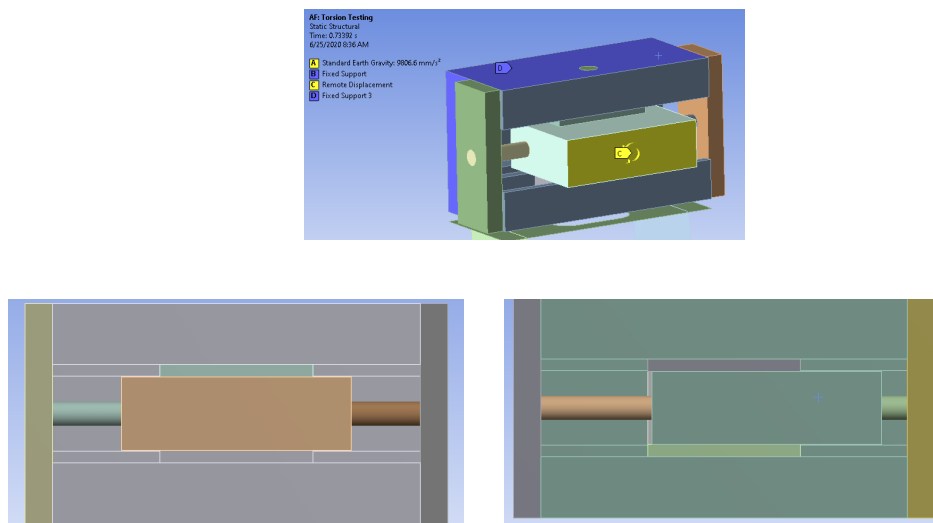


Figure 3.22: Cavity Support 1.5G Stress | Left: No Sliding | Right: Sliding

Once the initial analysis was complete and deemed satisfactory, focus shifted to simplifying the rather complex needle support geometry. The simplified geometry utilized a joint between the lug and the needle support to form a connection, and it had six degrees of freedom (DOF), which could be toggled as fixed or free, that include displacement and rotation. At first, all DOF were fixed, but this produced overly stiff behavior. Then the RDOF about the transverse axis was left free to allow for more movement, but it was not stiff enough. Finally, by keeping the transverse RDOF free while adding a torsional spring of equivalent rotational stiffness of the needle block components, the correct behavior was achieved. The rotational stiffness was determined by suppressing the cavity jacket and applying a unit degree of rotation to the lug, as shown in Figure 3.23. The rotational stiffness was found to be  $1.27 \text{ e}6 \text{ N-mm}$  per degree if the lug was centered, or  $2.45 \text{ e}6 \text{ N-mm}$  if the lug was off center by 36 mm, as it was for some cavity lugs. The geometry of the simplified joint is shown in Figure 3.24, and a more detailed comparison of results follows immediately.



*Figure 3.23: Needle Support | Top: Unit Rotation | Bottom Left: Centered Lug | Bottom Right: Offset Lug*

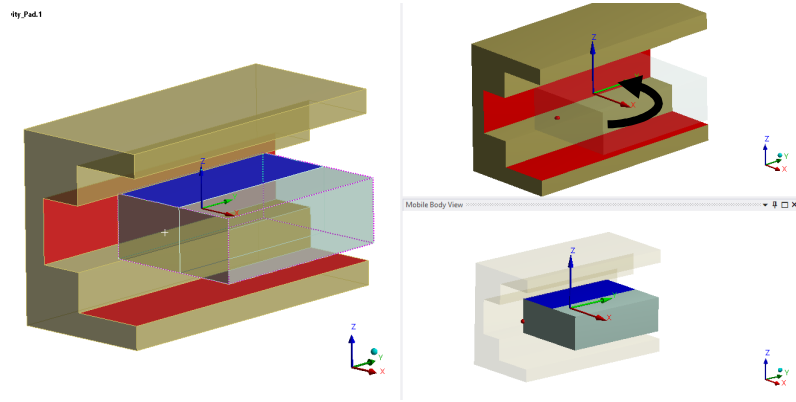


Figure 3.24: Simplified Support Model with Spring About X Axis

Shown in Table 3-1 is a detailed comparison of the simplification methods tested and the original results. From the results, it can clearly be inferred that the method using the torsion spring yields the most accurate results. A comparison of the stress due to 5G axial is shown in Figure 3.25, which illustrates the importance of accurate simplification as it relates to achieving accurate stress response. The case of 1.5G transverse slip was also evaluated, which can be tested by allowing the transverse UDOF to be free on one side of the support. The deformation of the loaded support arm was near identical for all tested models.

Table 3-1: Needle Support Results Comparison

<b>Geometry</b>	<b>Transverse Mode</b>	<b>Axial Mode</b>	<b>5G Support Max Disp.</b>	<b>1.5G Sliding Max Disp.</b>
<b>Detailed</b>	20.3 Hz	20.7 Hz	2.67 mm	1.36 mm
<b>Fixed DOF</b>	20.5 Hz	29.2 Hz	1.48 mm	1.32 mm
<b>Free Transverse RDOF</b>	18.1 Hz	20.5 Hz	3.50 mm	1.34 mm
<b>Free RDOF + Torsion Spring</b>	20.5 Hz	21.3 Hz	2.58 mm	1.33 mm

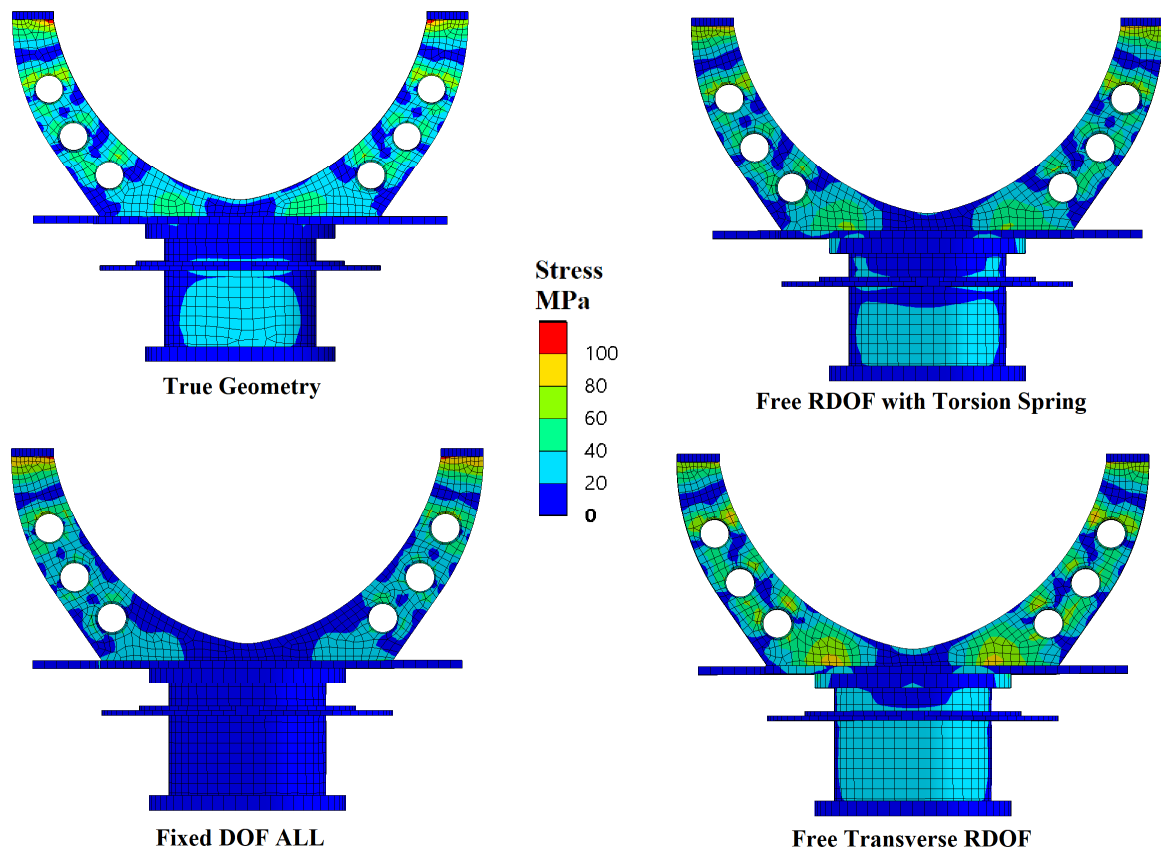
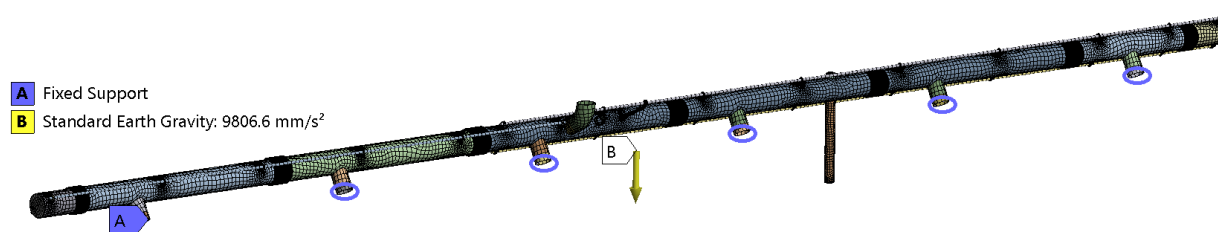


Figure 3.25: Needle Support 5G Stress Comparison

### 3.6 Two-Phase Pipe

Only minor simplifications were made to the two-phase pipe, with the flexible hoses being replaced by point masses. The model was cut at the connection points from the two-phase pipe to the cavity jackets. As this is a sturdy connection, the cut edges were given a fixed constraint. All components except for the Invar rods were meshed with shell elements. The mesh and boundary conditions are shown in Figure 3.26, and a more detailed view of the mesh is shown in Figure 3.27. The Invar rods were made of beam elements, and their connections to the rod guides varied by location. The ends of each Invar rod have fixed UDOF and RDOF, as in reality the rod is rigidly fixed at these locations. The center sections of the rod have free RDOF, fixed UDOF in the

transverse and vertical direction, and free UDOF axially. This closely mimics the behavior of a rod within a loose guide, as rotation and some axial movement is allowed but radial movement is not. This approximation was made because, at first, a solid mesh of the Invar rod and frictionless contacts between the rods and guides were used (as beam elements do not support frictionless contacts), but the structural results did not differ significantly from the beam and joint method. Additionally, the frictionless contact was unsuitable for modal analysis as it did not constrain the Invar rod motion, and the solution had trouble converging for structural analysis due to its non-linear nature. In total, 94K nodes and 31K elements were used.



*Figure 3.26: Two-Phase Pipe Mesh and Boundary Conditions*

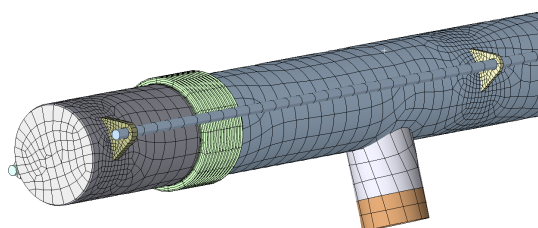


*Figure 3.27: Two-Phase Pipe End Section Mesh*

Modal analysis highlighted several critical issues with the two-phase pipe design. The first was a 10 Hz mode of the helium level sensor, as shown in Figure 3.28. As this component is made from G10 and is mounted to a stainless steel component with a sharp corner, there is potential that the axial flexing of the G10 plate could initiate a crack at this contact, as shown in Figure 3.28. As

the sensor assembly is blindly inserted into the two-phase pipe and then welded at the cap, any solution had to accommodate the lack of access to the sensor.

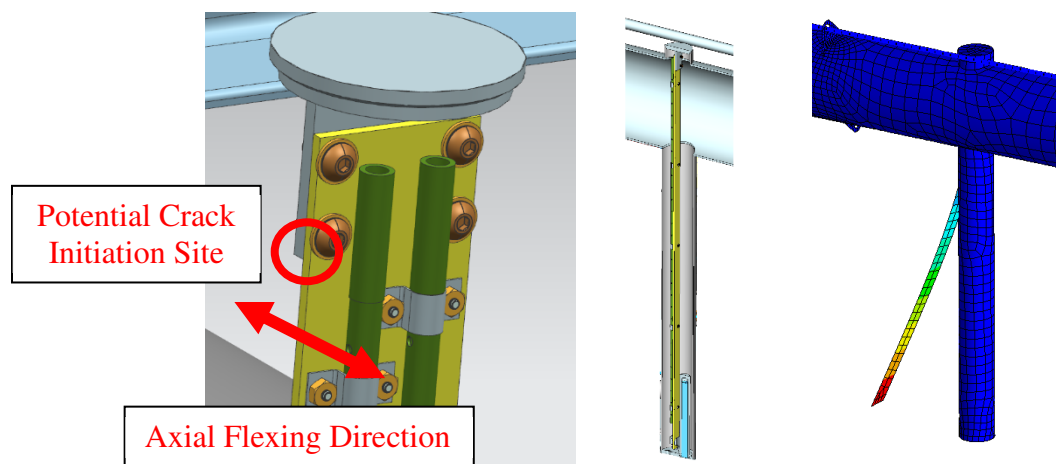


*Figure 3.28: Helium Level Sensor | Left: Potential Failure Mode | Center: Contextual View |  
Right: Mode Shape*

The second critical issue found was the motion of the end sections, which is shown in Figure 3.29. The downstream (DS) section resonated at 13 Hz while the upstream section (US) resonated at 16 Hz. The difference was due to the US having an additional rod guide near the bellow, which restricted motion. These modes had the potential to damage the bellows, as their low resonant frequency can be more easily excited during transport and fatigue can occur. Results from the structural analysis were used to confirm this hypothesis. The next lowest resonant mode was that of the helium level sensor pipe moving transversely at 34 Hz, which was not of concern due to its high frequency and low potential for high-amplitude motion.

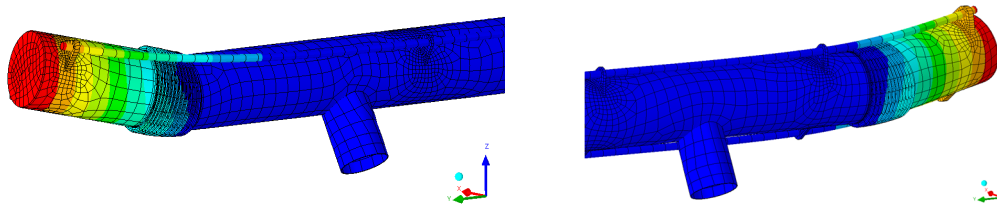


*Figure 3.29: End Section Modes | Left: Downstream 13 Hz | Right: Upstream 16 Hz*

As expected from the modal analysis, high deformation of the sensor plate was seen for 5G, and high deformation of the end sections was seen for 1.5G and 3G. The highest stresses during 5G were below 50 MPa and for 1.5G were below 90 MPa, which are well below the yield stress of both G10 and SS316L. During 3G, the stress at the bellows was near yield with 173 MPa, and the DS bellows had a maximum transverse displacement of 1.69 mm, which was close to the 2 mm limit. The total deformation of the end section due to 3G is shown in Figure 3.30; 3G deformation of a center section is shown in Figure 3.31. Given a cyclic transverse displacement of  $\pm 1.69$  mm, the bellows was predicted to have a fatigue life of 5,200 cycles, well below the necessary 240,000 cycles, and as such redesign was necessary. Other than the end bellows, the highest 3G stress was 82 MPa in the piping, and the highest transverse bellows displacement was 0.61 mm.

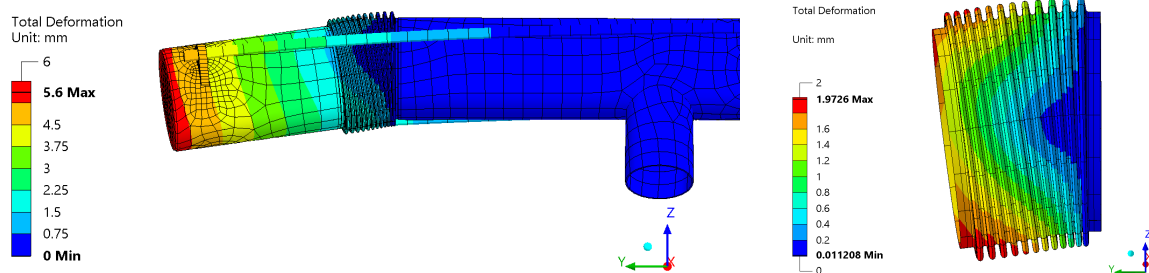


*Figure 3.30: End Section 3G Total Deformation*

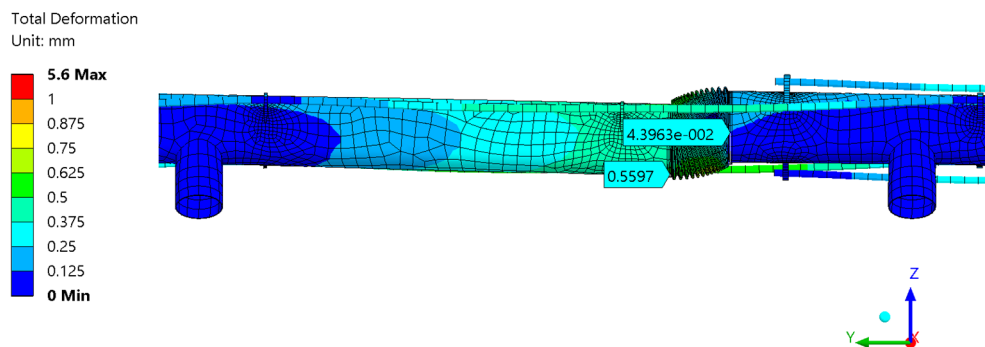


*Figure 3.31: Center Section 3G Total Deformation*

The remedy for the helium level sensor was an additional guide welded to the bottom of the helium level tube which constrained the axial motion of the plate. The guide is shown in Figure 3.32, which has tapered edges that allow for blind insertion, a cutout that allows for uninterrupted flow of liquid helium, and 1 mm of clearance on all sides of the plate. With the guide, the first resonance increased to 35 Hz, which was well above the required minimum.

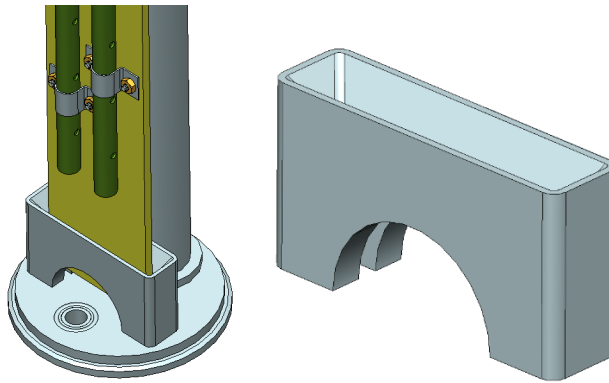


*Figure 3.32: Helium Level Sensor Guide*

To minimize movement of the end sections, two design modifications were made. First, the position of the bellows was shifted towards the end of the pipe, reducing the mass which each bellow must support. The same overall length of the pipe was maintained for purposes of balancing forces during thermal contraction. Second, additional guides were added which limited the movement of the bellows. The design of the bellow was also adjusted, but this was not for the purpose of transportation. The first resonant frequency involving the end sections increased to 31 Hz, and the maximum transverse deflection was 0.076 mm, which increased the fatigue life to above  $1e7$  cycles. Deformation of the end section is shown in Figure 3.33. As a result of identifying the end bellows as a weak point, installation tooling was added to restrain the movement of the bellows after they are welded on, but before the Invar rods are installed. This prevents excessive deflection which could damage the bellows; the tooling is shown in Figure 3.34.

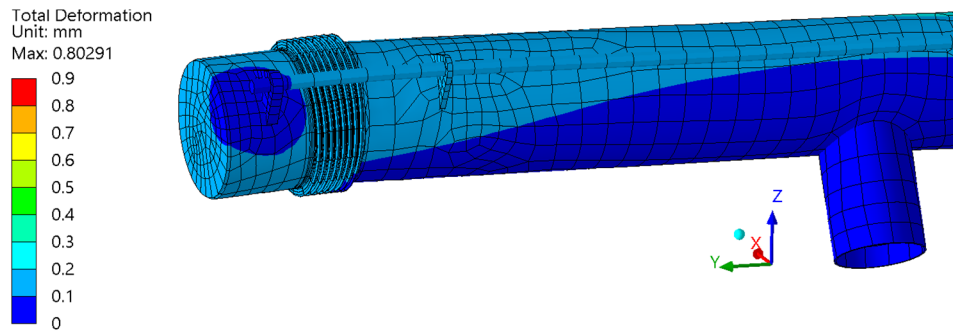


*Figure 3.33: Improved Design – End Section - 3G Total Deformation*

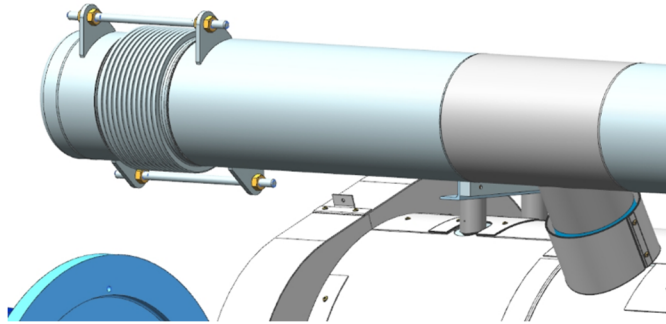


*Figure 3.34: Installation Tooling Used Before Invar Rods Can Support Bellows*

### 3.7 Heat Exchanger

While the heat exchanger will not be installed for any overseas transport, it must still survive on-site transport, and its cantilevered nature leaves it prone to low resonant vibration and potentially high stress at the lower welded connection. The cut boundaries were the welded tees to the adjacent cavity jackets and where the check-valve pipe welds to the vessel. The boundary conditions and mesh are shown below in Figure 3.35. The mesh was primarily shell elements; it contained 40K nodes and 23K elements, and bonded contacts were used throughout.

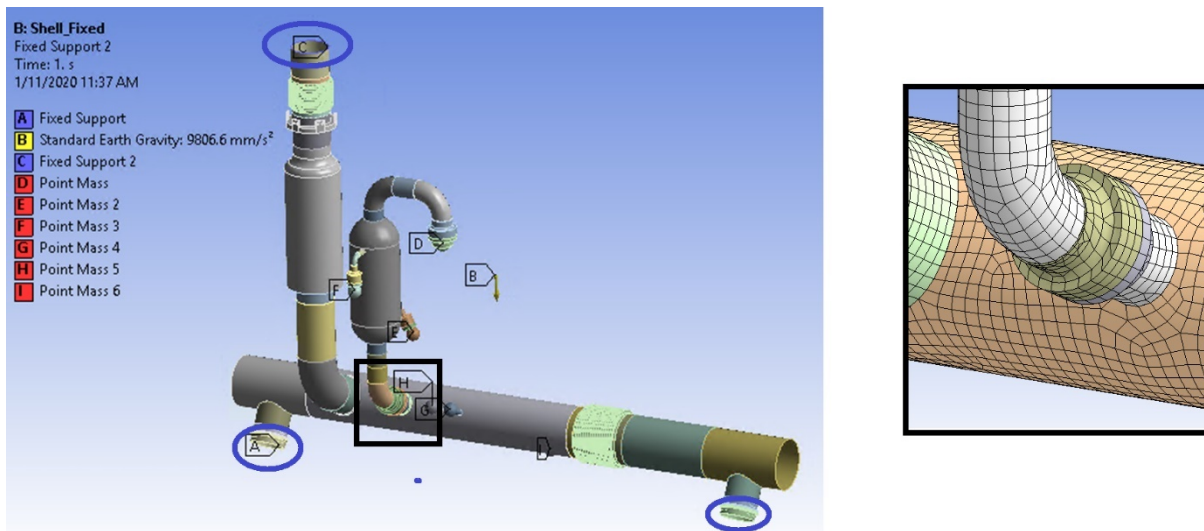


Figure 3.35: Heat Exchanger Boundary Conditions and Mesh

As expected, modal and structural analyses revealed key issues. The heat exchanger, heavy and supported only from below, resonated transversely at 8 Hz and axially at 12 Hz. Structural analysis found stress in the weld connecting the heat exchanger and two-phase pipe to be above 300 MPa during 1.5G transverse and above 270 MPa for 5G axial, both well above yield. For each case, the bellows movement was within the maximum allowable displacement. While such accelerations are not likely for on-site transportation, it is apparent that even lower magnitude accelerations could induce yielding, and due to the critical nature of the heat exchanger, a support was designed to restrict its motion. The stresses and mode shapes are shown in Figure 3.36.

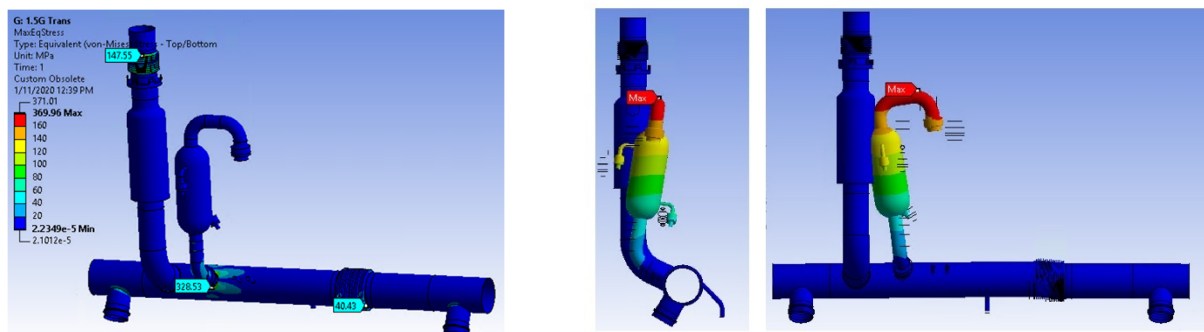
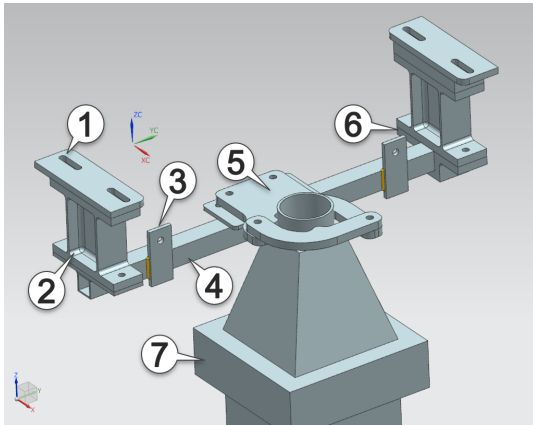


Figure 3.36: Heat Exchanger | Left: 1.5G Stress | Center: 8 Hz Mode | Right: 12 Hz Mode

Several design constraints were placed on the support, which included the following: heat load to the heat exchanger must be less than 0.20 Watts (W), heat load to the thermal shield must be less than 5.0 W, the support must allow for adjustment in the three principle directions by  $\pm 10$  mm, and the support must not inhibit thermal contraction during the cooldown process. After several iterations, the design shown in Figure 3.37 was settled on. It attached to tabs welded to the vessel (1) and utilized G10 thermal standoffs (2) to limit the heat flow from the room-temperature vessel. G10 shims between (1) and (2) allow for vertical adjustment, and slots on (1) allow for axial adjustment. The design of the standoff intentionally mimicked that of an I-beam, which limited the cross-sectional conducting area while maintaining structural rigidity and ease of manufacture. The cross-bar (4) mounts on each side to the standoffs and is fixed on one side while the other uses a guide (6) to allow for thermal contraction of the bar. The assembly has thermal intercepts (3) which connect to the 50K thermal shield via thermal straps. A two-part collar (5) surrounds the neck of the heat exchanger, limiting axial and transverse movement while allowing for vertical thermal contraction. The collar is adjustable transversely and utilizes three round contact points to limit conduction to the heat exchanger.



Number	Description
1	Vessel Tabs - SS316L
2	Thermal Standoffs - G10
3	Thermal Strap Mount - SS316L
4	Cross Member - SS-316 L
5	Mounting Collar - G10
6	Sliding Support - G10
7	Heat Exchanger (updated design)

*Figure 3.37: Heat Exchanger Support Components*

Validation of the thermal performance was done for both the standoffs and the collar. This was done with ANSYS ® Static Thermal analysis. The support had 300K and 50K temperatures applied to the opposing upper and lower surfaces, which resulted in a net heat flow of 0.57 W. For the collar, the face which mates to the cross member had an applied 50 K temperature, and the contact points to the heat exchanger had an applied 2 K temperature. The result was a 0.06 W heat load to the heat exchanger. Both heat loads were well below the established maximums. The temperature distribution for each is shown below in Figure 3.38.

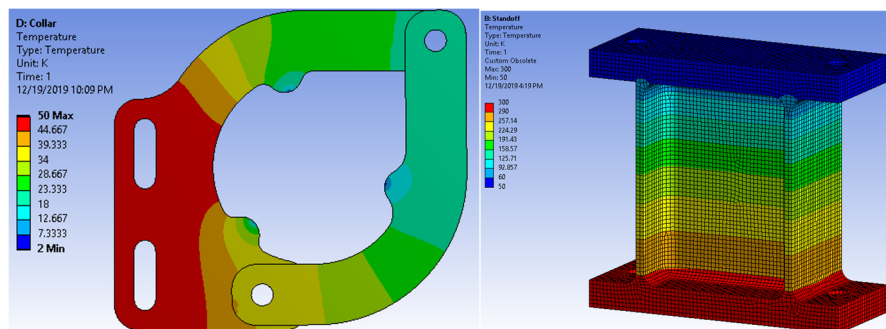


*Figure 3.38: Support Thermal Results | Left: Collar | Right: Standoff*

With the support, the maximum weld stress was reduced to 67 MPa, and the first resonance increased to 30 Hz. The highest stress in the G10 components of the support was 22 MPa. The updated first mode shape is shown in Figure 3.39.

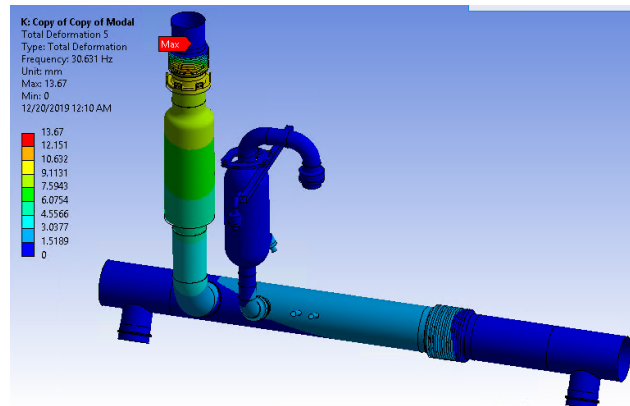


*Figure 3.39: Heat Exchanger Updated First Mode Shape*

### 3.8 Cryogenic Lines

Starting with the 2K line, the only major simplification made was to model the flexible hoses as point masses. This was done due to the complex geometry and behavior of the corrugated hoses which are wrapped in braided wire. The following locations were given fixed constraints: the edge on the fill lines that connects to each cavity jacket, the point on the 2K line that attached to the pumping line support, the edge on the line that connects to the helium level sensor, and the helium inlet line that is connected to the system via flex hose. Six guides along the length of the 2K line allow for thermal contraction but restrict transverse and vertical movement. These locations on the line were constrained as such using body-ground joints. For a more conservative analysis, the RDOF at each joint were left free. Entirely shell mesh was used, and a finer mesh was used to

accurately capture the curvature of the smaller piping. Additionally, since the model would not be later incorporated into a larger analysis, the mesh size was not prohibitive. In total, 62K nodes and 21K elements were used. The boundary conditions are illustrated in Figure 3.40, and the mesh and a reference image of the true geometry is shown in Figure 3.41.

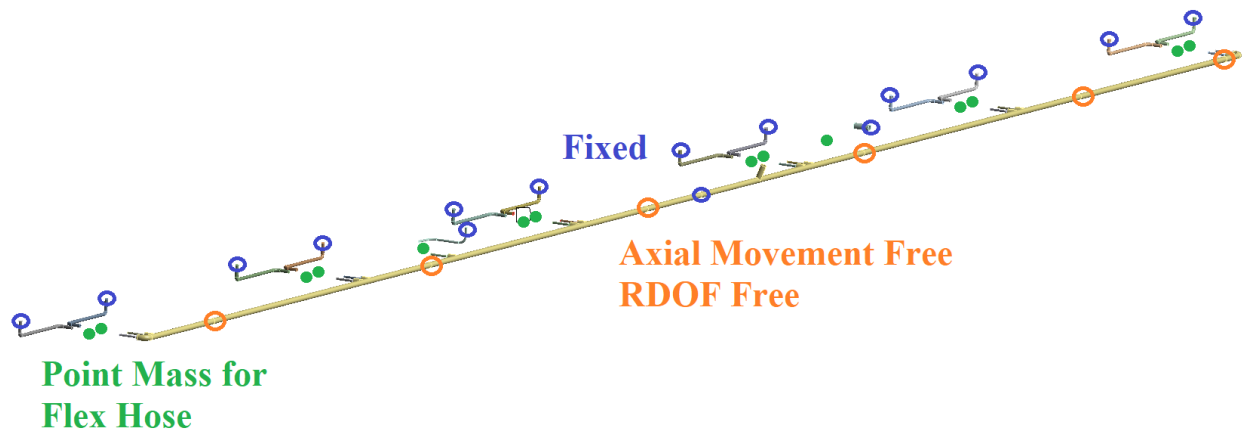


Figure 3.40: 2K Line Boundary Conditions

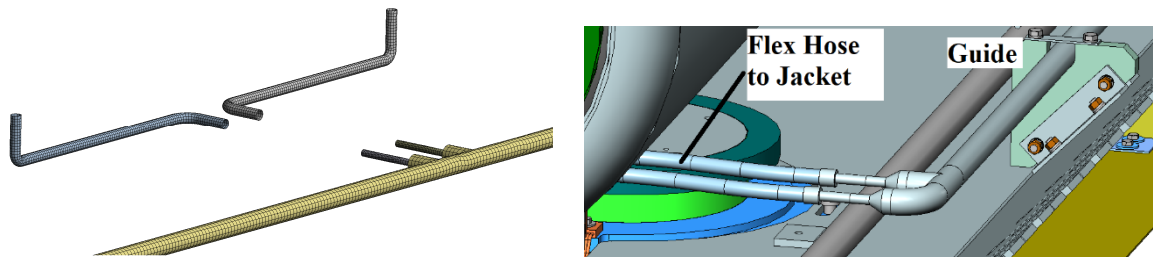


Figure 3.41: 2K Line | Left: Mesh | Right: Reference Image of CAD Model

Neither the modal nor structural analysis highlighted any issues with the 2K line. The first resonant mode occurred at 22 Hz with the transverse flexing of the largest unsupported span of the line, as shown in Figure 3.42. Resonance of the fill lines did not occur until 60 Hz. The highest stress was 30 MPa at the fill line due to 3G. As the fill lines are unsupported and must support part of the connected flex hose, which have rather low mass at 0.042 kg, this location

and magnitude of stress were reasonable. The highest deflection was also due to 3G, which saw 0.75 mm deflection in the main section of the 2K line. Both the stress and deflection are shown in Figure 3.43. As the stresses in the 2K line were very low and the first resonant mode was above 20 Hz and did not involve movement of any critical components, the results were deemed satisfactory.

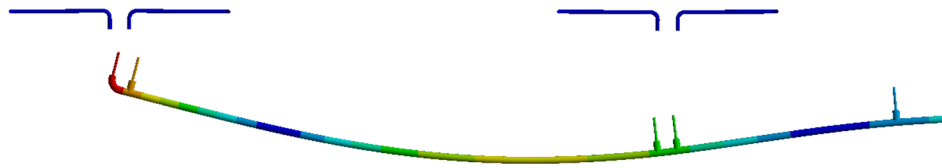


Figure 3.42: 2K Line First Mode Shape 22 Hz

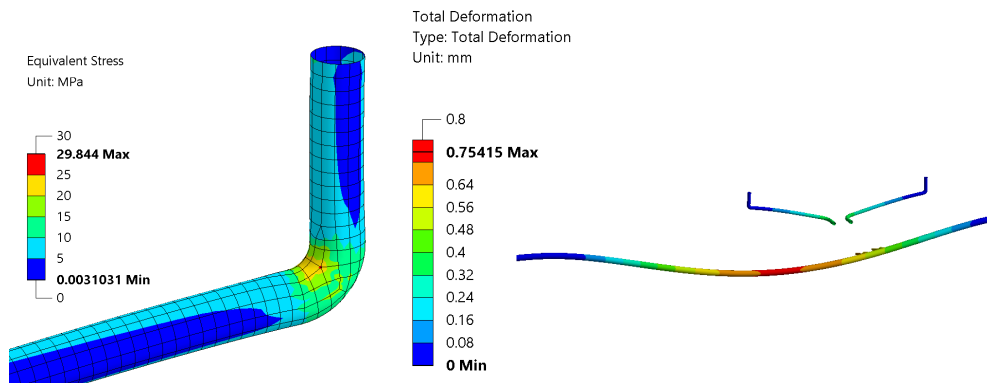


Figure 3.43: 2K Line 3G Results | Left: Fill Line Stress | Right: Total Deformation

As for the 5K line, the geometry was simplified by making any attached components, such as copper thermal straps, as point masses. The supports at either end of the 5K line only constrain

vertical motion and outward axial motion. Thus, the mating location was given a fixed condition for 3G vertical, and for 5G, one side was fixed because the opposite side must be allowed to come out of contact. For 1.5G, the fixed support was replaced with a body-ground joint which constrained axial and vertical movement but allowed transverse movement. For modal analysis, the vertical and axial movement were fixed. While this axial constraint is not entirely accurate for modal analysis, not restraining the motion would greatly underestimate the line's stiffness. As the supports are tightened against the line during installation, it is unlikely that it would see excitation sufficient to resonate axially, create a gap, and cause any meaningful amount of damage to the line. Each location where the line was supported along its length (similar to the 2K line, but via the cavity supports) was constrained in the vertical and transverse directions but remained free axially and for all rotations. Entirely shell mesh was used, with a total of 44K nodes and 11K elements. The mesh was refined at the corners, as they saw the highest stresses. The boundary conditions are shown in Figure 3.44, and the mesh and a reference image of the transport support are shown in Figure 3.45.

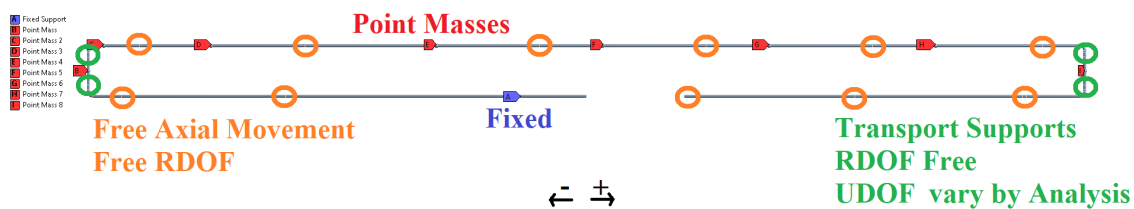
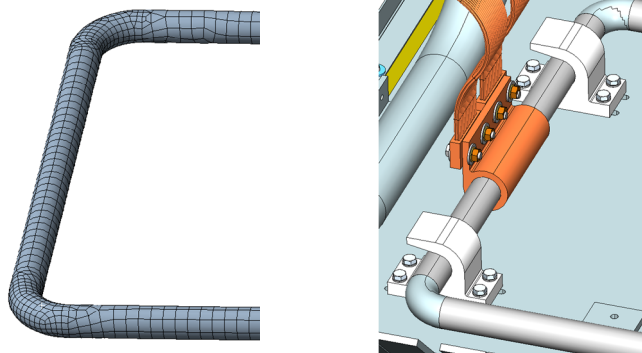
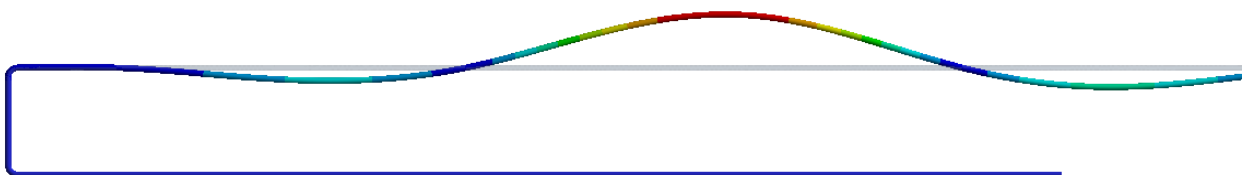


Figure 3.44: 5K Line Boundary Conditions



*Figure 3.45: 5K Line | Left: Mesh | Right: Reference Image Transport Supports*

The modal analysis did not identify any significant issues. While the first resonant frequency occurred at 14 Hz, it did not involve any movement that was expected to induce significant stress in the system or involve any delicate components. The mode shape was similar to the 2K line, in which the largest unsupported section flexed transversely, then vertically, as shown in Figure 3.46. The next resonant mode occurred above 20 Hz with a similar motion of the adjoining section.



*Figure 3.46: 5K Line 14 Hz Mode Shape*

Structural analysis identified the weakest configuration of the 5K line, which occurs during a 5G axial acceleration in only one direction. For the case of acceleration in the negative direction (as labeled at the bottom of Figure 3.45), the right half of the 5K line is free to separate from its transport supports, which only prevent inward motion. This situation causes 14.7 mm of deflection at the far end, with 193 MPa of stress. These results are shown in Figure 3.47. Given that the line is made of SS316L, this stress is allowable but does have a low factor of safety. For 5G acceleration in the opposite direction, the maximum deflection is only 0.25 mm, with 50 MPa of stress. For 3G vertical, the line saw a maximum deflection of 2.7 mm and 31 MPa of stress, and for 1.5G transverse it saw 1.3 mm deflection and 16 MPa of stress. As the 5K line did not see stresses above yielding, and the design of the system is such that no additional constraints can be added due to limited access and thermal contraction requirements, the results were deemed allowable.

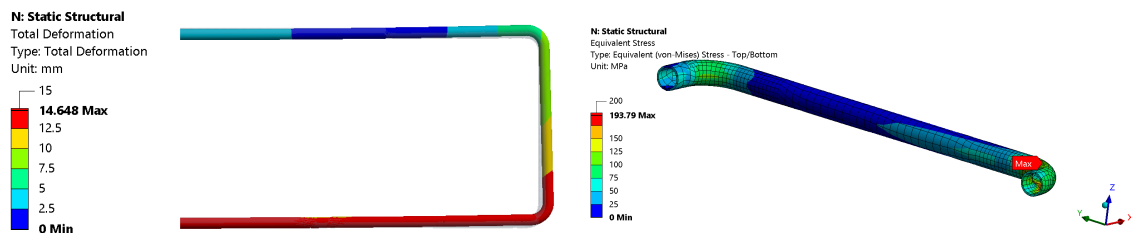


Figure 3.47: 5K Line 5G Results | Left: Deformation | Right: Stress

### 3.9 Pumping Line Support

The simplifications made to the pumping line support were the following: the angled brackets that mounted to the lower thermal shield were replaced with fixed constraints, the flexible hose

was replaced as a 2 kg point mass that attached to both sides of the pumping line, and the 2K line – which is restrained by the support – was modeled as a 13 kg point mass. The edge of the bayonet that connects to the vessel was given a fixed constraint, as shown along with the mesh in Figure 3.48. A mix of shell and solid elements was used. Solid elements were used for the threaded rods that support the pumping line and for a section of the G10 structure. Frictional contacts with bolt pretension were used to best determine the stresses at the G10 support, as it was a concern that significant displacement of the line due to 5G could create high stresses at the support, which could initiate a crack in the G10 material. In reality, a restraint between the pipe to the heat exchanger and the thermal shield will be in place for transportation. However, as the configuration is unknown, the analysis did not account for this and as a result is more conservative. In total, 51K nodes and 13K elements were used.

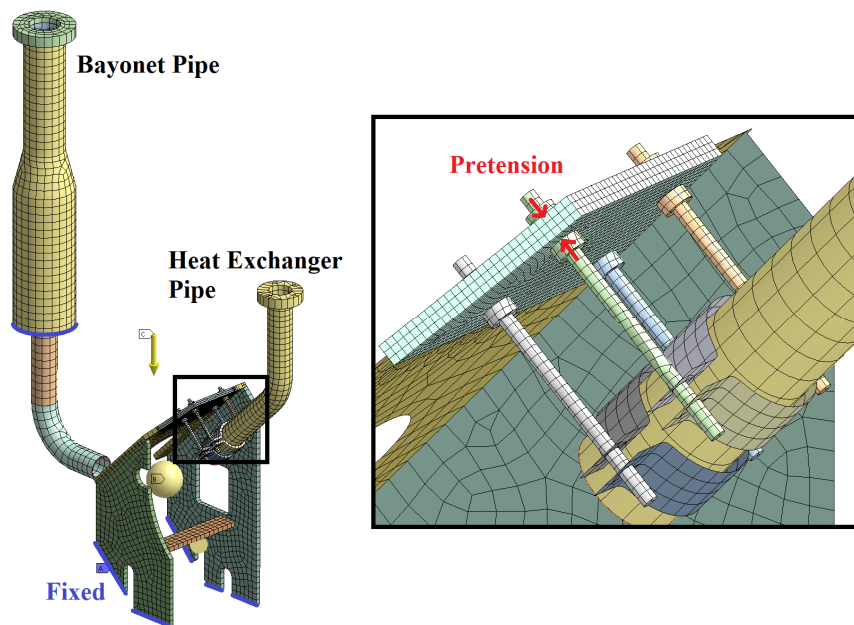


Figure 3.48: Pumping Line Support Mesh and Boundary Conditions

Modal analysis did not highlight any serious issues with the support. The first mode occurred at 27 Hz with the axial motion of the heat exchanger pipe. Structural analysis found that 5G axial created the highest deformation of the heat exchanger pipe, and thus the highest stresses. The pipe deflected by 4.6 mm, and the SS316L threaded rods saw a maximum stress of 131 MPa, which is below the yield point of 205 MPa. The maximum principal stress in the G10, which is a brittle material, was 14 MPa, far below its yield criteria. As predicted, the highest stress did occur at the contact with the threaded rods and was primarily due to the bending of the heat exchanger pipe. The mode shape and 5G deformation are shown in Figure 3.49, while the stresses due to 5G are shown in Figure 3.50.

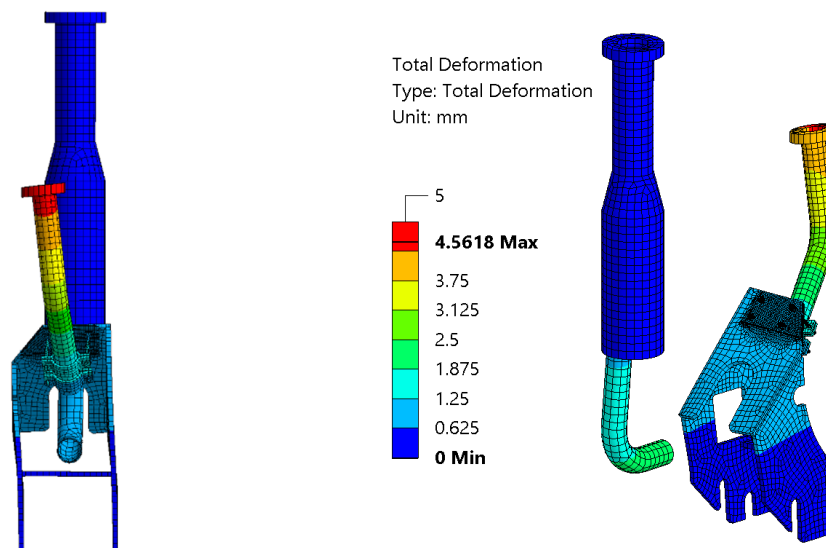


Figure 3.49: Pumping Line Support Results | Left: Mode Shape 27 Hz | Right: 5G Deformation

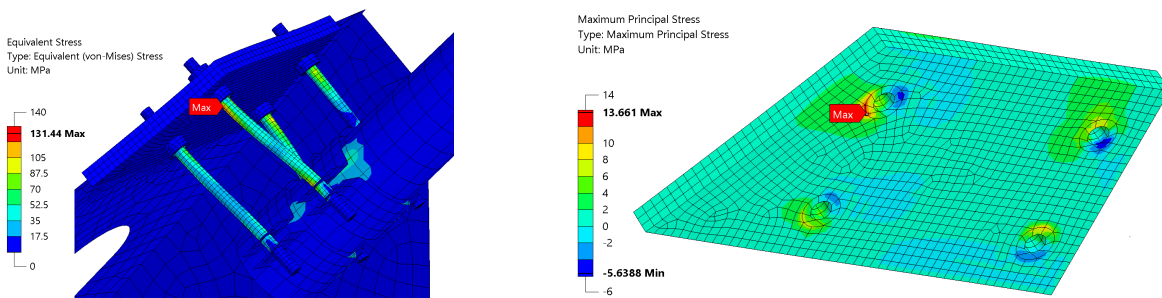


Figure 3.50: Pumping Line Support 5G Stress | Left: Rods Eq. Stress | Right: G10 Prin. Stress

### 3.10 Thermal Shield

The thermal shield had minor simplifications, which included bolted connections and welds being replaced as bonded contacts. Shell elements were used for all bodies except the G10 studs, and the mesh contained 72K nodes and 24K elements, shown in Figure 3.51. G10 studs that contact the vessel were given frictionless supports for modal analysis, as shown in Figure 3.51. This allowed the studs to slide in the directions shown, which mimicked reality as they are tightened against the vessel before transport. For structural analysis, the frictionless support was eliminated for the vertical 3G load, which allowed for separation, and for 1.5G, the supports on one side were suppressed to allow for potential separation. Both were done to allow for the highest deformation and stresses to evaluate the worst possible scenario.

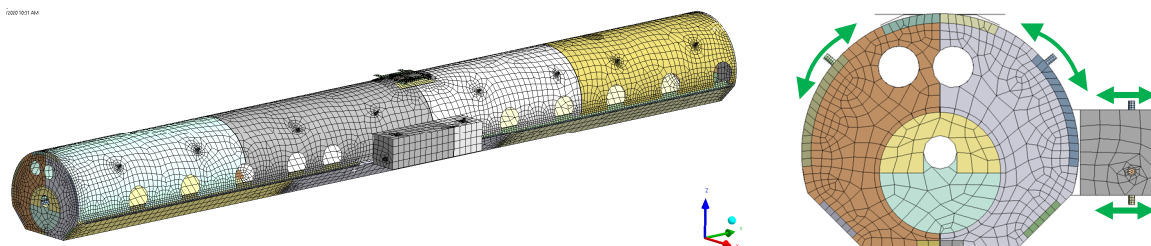
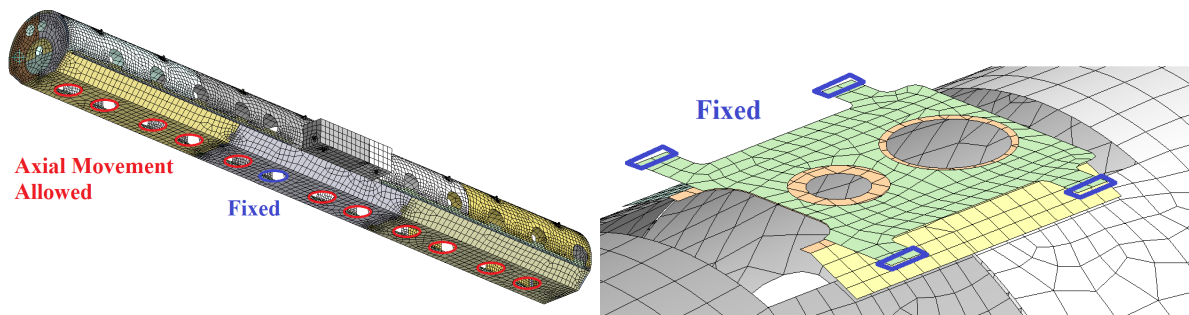
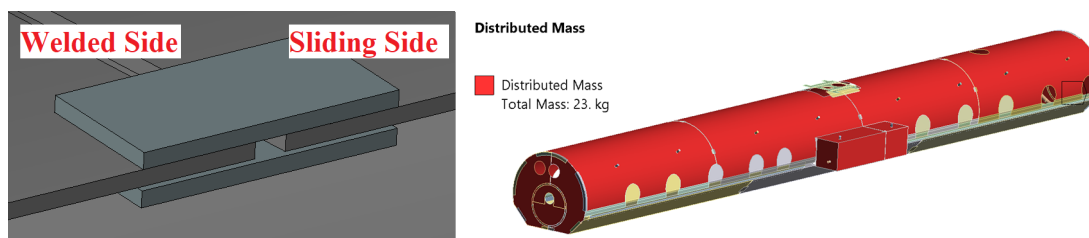


Figure 3.51: Thermal Shield | Left: Mesh | Right: Frictionless Supports

The thermal shield was supported by each cavity support, but only at one location is it fixed with screws. This allows for thermal contraction in the axial direction. At the other supports, slots in the shield and screws allow only axial movement and no vertical movement. These same constraints were placed on the model. For transportation only, a support is installed from the vessel to the shield near the chimney, which limits movement. The locations that would have mounted to the vessel were given a fixed condition, as this is a rigid connection. There are guides that connect each section of shield and prevent adjacent sections from being misaligned. Sections on the shield surface of the same size were attached via joints that locked their transverse displacement, vertical displacement, and rotations to the adjacent shield. Last, a distributed mass of 23 kg was applied to the upper thermal shield, end plates, and side port to simulate the weight of the insulation. It was only applied to surfaces that would bear the load, which is why it was not applied to the lower thermal shield. The aforementioned boundary conditions are illustrated in Figure 3.52 and Figure 3.53.



*Figure 3.52: Thermal Shield Boundary Conditions | Left: Cavity Support Conditions | Right: Transport Support*



*Figure 3.53: Thermal Shield Boundary Conditions | Left: Shield Guide Section View | Right: Distributed Mass*

The bolts at the fixed location on the shield (see Figure 3.52) were evaluated with analytical methods, as they play a critical role in restraining the shield's movement. As the other mounting locations prevent vertical and transverse movement, only the axial 5G load was considered. The entire mass of the thermal shield and attached components – 600 kg – was considered. It was assumed that the other areas provided negligible frictional resistance, and only the tightness of the bolts would prevent axial motion. With the original 6 x M8 SS316L bolts, the average shear stress was 150 MPa, which exceeded the 117 MPa shear yield strength. Additionally, the original design had the bolts threading into the aluminum plate on the support, which severely limited how tight they could be without stripping the threads. Even so, with the bolts tightened to 75% of yield, a friction coefficient of 1.05 for clean aluminum [27], and a FOS of 2 due to the uncertainties of friction estimates, the shield would slide at 2.6 G of acceleration. Understanding the modes of failure, the bolts were changed to 8 x M12 SS316L and were made to have locking nuts instead of threading into the support plate. The new design had a FOS= 2.4 for yielding and 1.7 for sliding. Figure 3.54 shows both the previous and updated designs. More detailed calculations can be found in APPENDIX A.

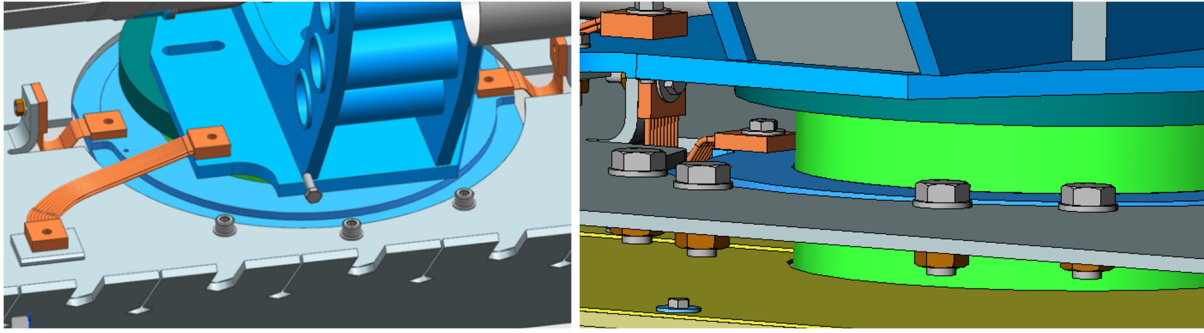


*Figure 3.54: Left: Previous Attachment to the Support Post | Right: Updated Design*

Modal analysis did not highlight any issues with the thermal shield, and the first resonant mode occurred at 23 Hz with the vertical movement of all sections of shielding. As this was above 20 Hz and did not include the movement of any critical components, it was deemed acceptable. The mode shape is shown in Figure 3.55.

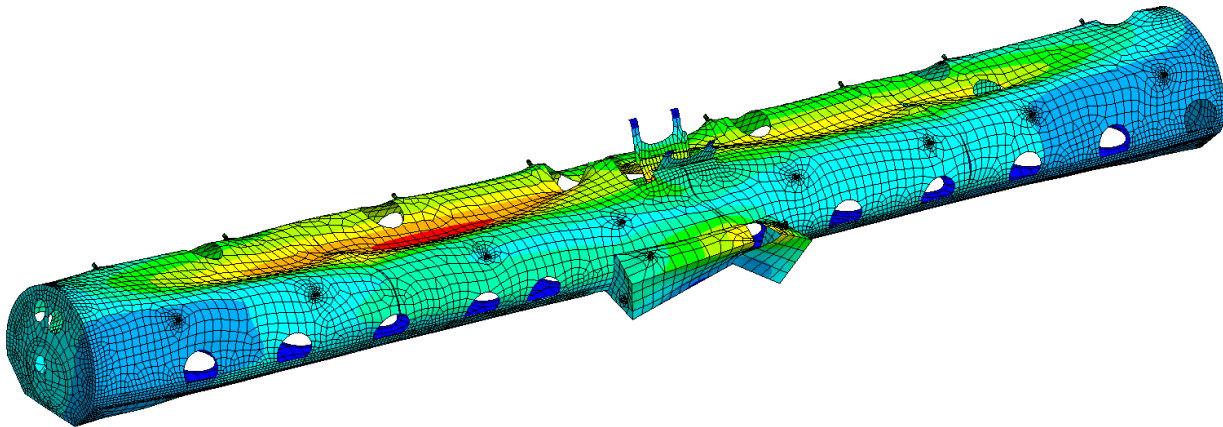


*Figure 3.55: Thermal Shield First Mode Shape 23 Hz*

Structural analysis did not highlight any issues with the shield either. The highest stress was 102 MPa at the transport support due to upward 3G acceleration, which was expected as it prevented the downward motion of the shield. The maximum deformation was below 4mm, which

is sufficiently low to stay out of contact with other components. Relevant structural results are shown in Figure 3.56 and Figure 3.57.

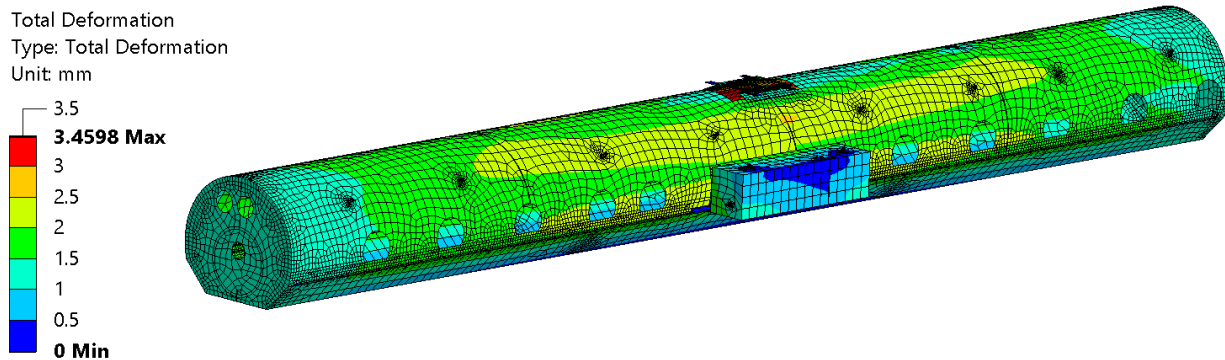


Figure 3.56: Thermal Shield 3G Deformation

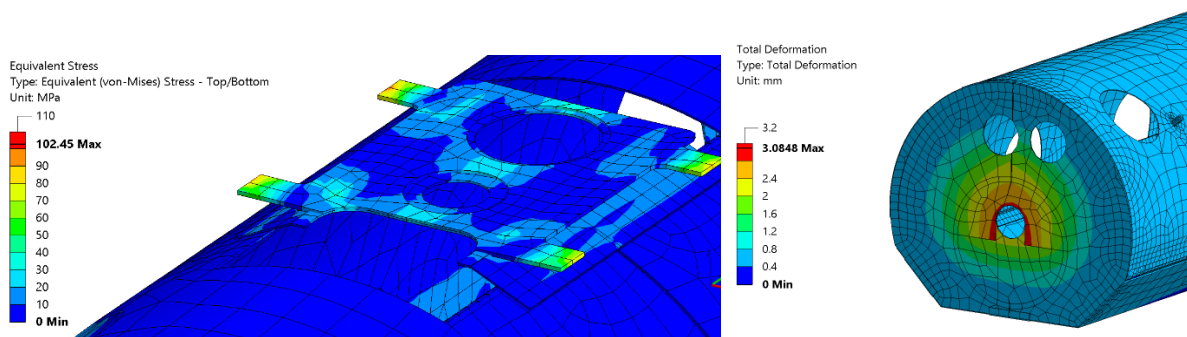


Figure 3.57: Thermal Shield Structural Results | Left: 3G Stress | Right: 5G Deformation

### 3.11 Magnetic Shields

The local magnetic shield for each cavity does not rigidly attach to the cavity at any location. Instead, the shield is assembled around the cavity jacket and attaches to itself, acting as a sleeve. This proved difficult for analysis, as frictional contacts are not viable for modal analysis and are computationally expensive for structural analysis. Low-frequency vibration of this component was unlikely to cause any damage to surrounding components. Additionally, as the shield is evenly

supported by the jacket, it was unlikely that any load would stress the shield enough to significantly affect its magnetic-shielding properties. For the aforementioned reasons, the local magnetic shields were not analyzed. Instead their effect in the combined analysis was achieved by placing an equivalent distributed mass across the cavity jacket.

The global magnetic shield was analyzed in two separate analyses: one for the center section near the side port and one of the end plates. This was done to reduce solution times and was justified since each section of the shield rigidly attaches to the vessel, and so one section does not influence the response of another. The sections evaluated are representative of all unique sections of shielding. Entirely shell mesh was used, with the central section having 74K nodes and the end section having 61K nodes. Connections to the vessels were made as fixed locations and were done so at the bolt holes in the geometry that was taken directly from FNAL. The side port had several frictionless supports which emulated the support from the G10 studs on the thermal shield. The mesh and boundary conditions for each analysis are shown in Figure 3.58 and Figure 3.59.

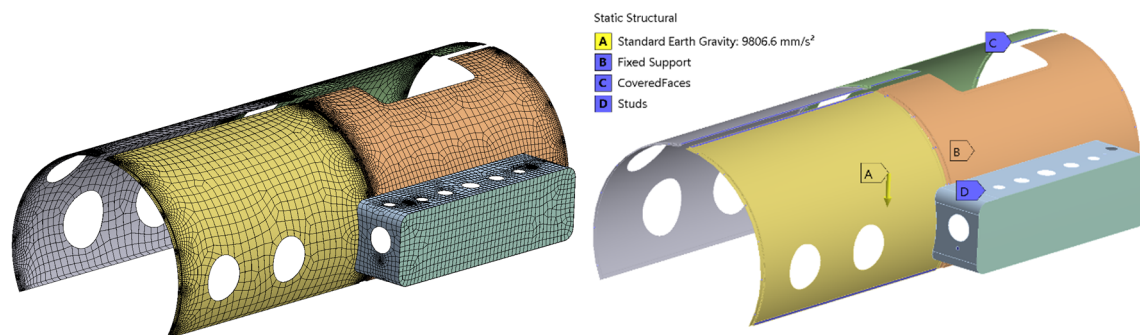


*Figure 3.58: Global Magnetic Shield Center Section Mesh and Boundary Conditions*

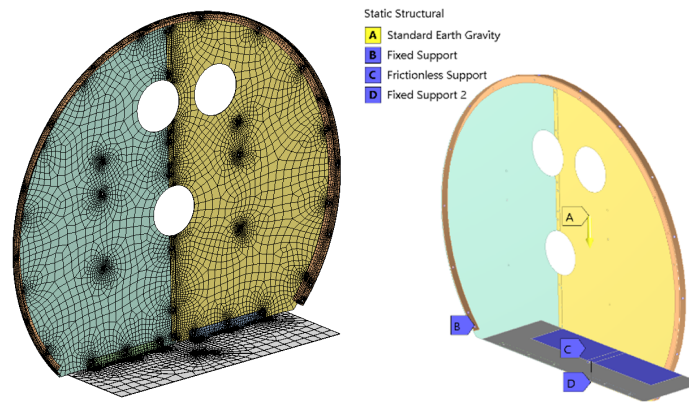


*Figure 3.59: Global Magnetic Shield End Section Mesh and Boundary Conditions*

No issues were found with the central section of shielding. The lowest resonant mode was 33 Hz, which saw the flexing of the side port, as shown in Figure 3.60. Structural analysis found the highest stress was 84 MPa due to 5G axial, but this was only a singularity at a fixed edge. Both these results were more than satisfactory per the requirements.

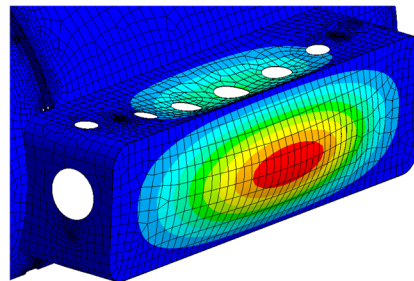


*Figure 3.60: Central Section First Mode Shape 33 Hz*

Modal analysis and structural analysis highlighted issues with the end section of shielding. The first mode occurred at 10 Hz with the axial flexing of the magnetic shield. While the shield is not as critical a component as a bellows, repeated flexing can damage its shielding properties, and

so this should be avoided if possible. Structural analysis found that at 5G the shield deflected by 23 mm, and stresses above yield for Mu-metal were present outside the edge-edge contacts, as shown in Figure 3.61.

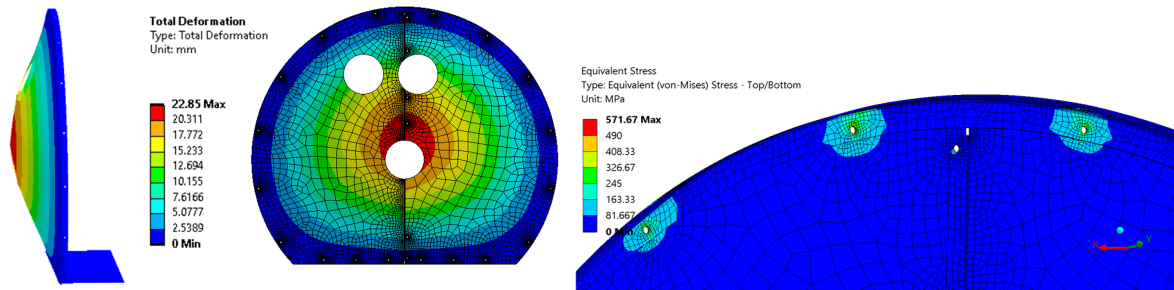


Figure 3.61: Global Shield End Section | Left: 10 Hz Mode | Center: 5G Def. | Right: 5G Stress

To increase the stiffness of the shield, two stiffener L channels were added across it. They measured 25mm x 25mm x 3 mm thickness. The first resonant mode increased to 21 Hz, the 5G deflection was limited to below 4 mm, and the maximum non-singular stress was 128 MPa, which was below the yield point of 160 MPa. The improved design and its 5G results are shown in Figure 3.62

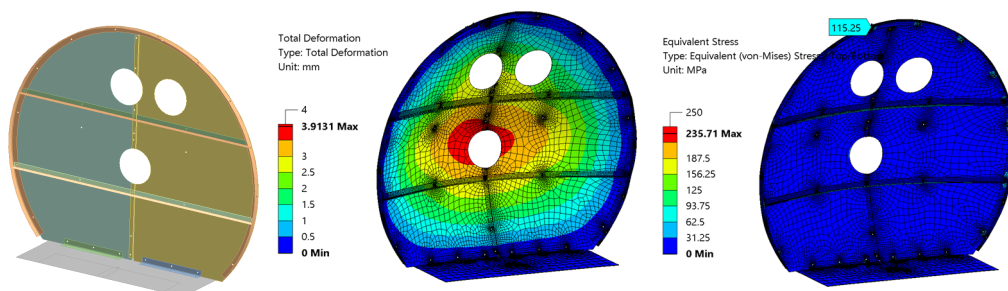
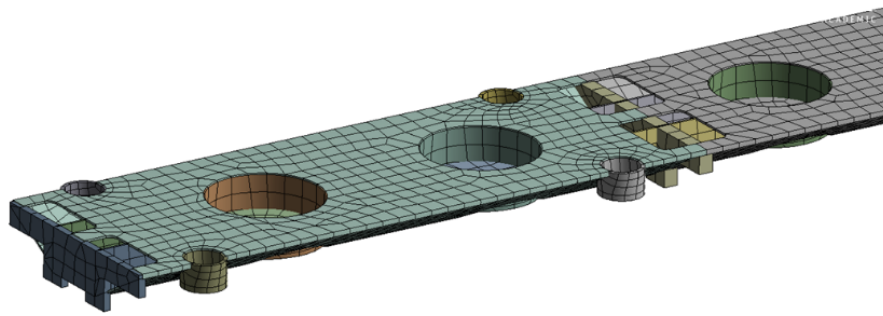


Figure 3.62: End Section Revised Design and 5G Results

### 3.12 Strongback

The strongback geometry only required minor simplification. The plates that connect each section were instead modeled as a single plate with twice the thickness. The final mesh, shown in Figure 3.63, was entirely shell, continuous, and contained 30K nodes and 10K elements. A 4,000 kg point mass attached to where the support posts would be, and this simulated the effect of the cold mass. The fixed boundary was placed at the connection to the strongback supports, as shown in Figure 3.64, and was done so as it allowed for an accurate comparison to previous analysis by CEA.



*Figure 3.63: Strongback Mesh*

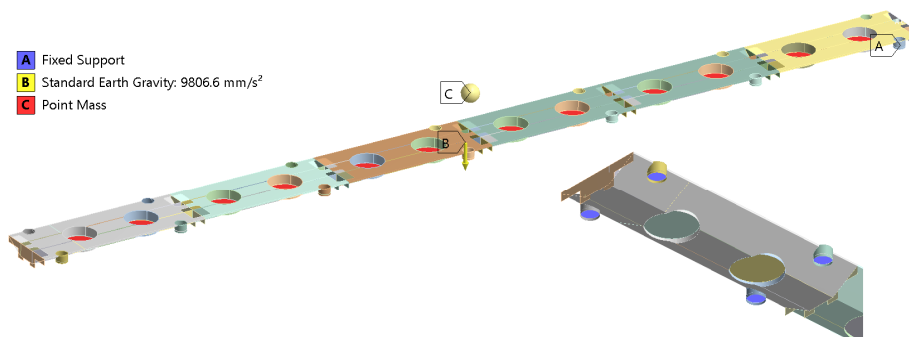


*Figure 3.64: Strongback Boundary Conditions*

Modal analysis did not highlight any issues with the strongback. The first mode occurred at 32 Hz with a transverse rocking of each section, followed by a 71 Hz vertical bouncing of each section. The response was expected to change significantly once modeled with the supports and vessel, as it would reduce the rigidity of the system. The mode shapes are shown in Figure 3.65. Previous analysis by CEA found the first mode to be 34 Hz [28], which agrees strongly with this analysis.

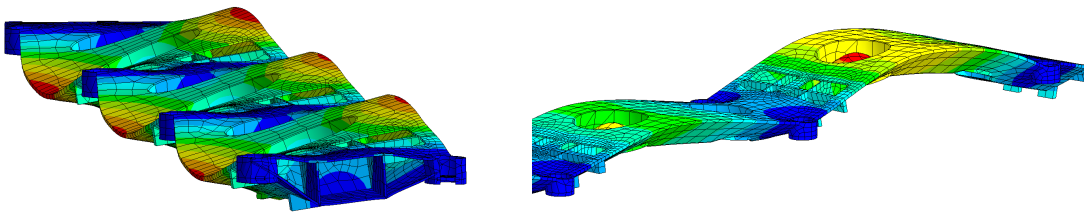


*Figure 3.65: Strongback Modes | Left: 32Hz | Right: 71Hz*

Structural analysis did not highlight any issues for the strongback. The highest stresses during 1.5G, 3G, and 5G were 67 MPa, 56 MPa, and 54 MPa, respectively. For both 5G and 3G, the highest stress occurred near the support location, and for 1.5G it occurred on the top plate. The stress due to 3G is shown in Figure 3.66. The highest deformation was 0.40 mm due to 3G at one end section, as shown in Figure 3.67. Based on the displacement of the adjoining section, this could create 0.20 mm transverse bellows displacement, which is not significant. The results from this analysis strongly matched those performed by CEA, which are shown in Appendix B.

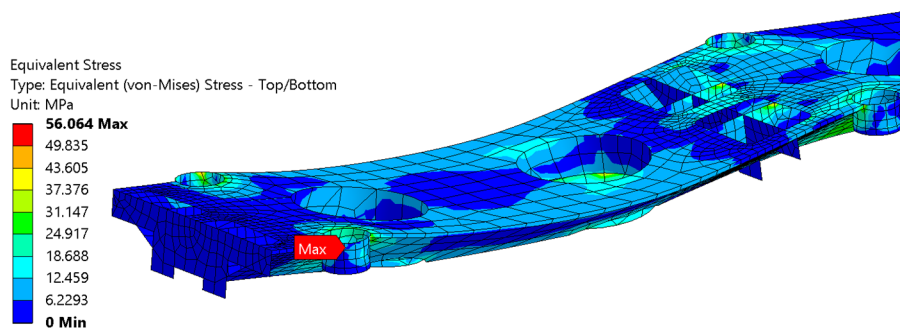


Figure 3.66: Strongback 3G Stress

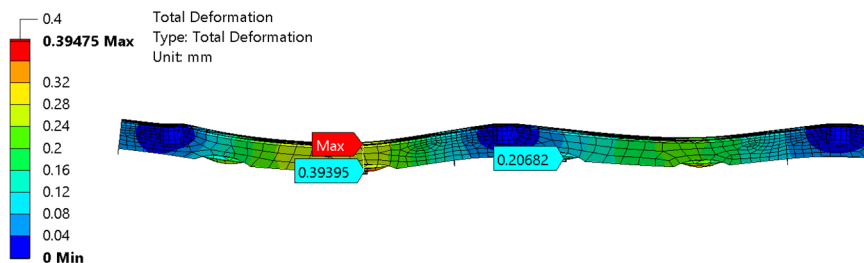


Figure 3.67: Strongback 3G Total Deformation

### 3.13 Strongback Supports

The strongback support required some simplification for initial analysis. This included the removal of bolts, pins, and threads. Analytical calculations found the design of several connections were insufficient to prevent yielding. The calculations for the three separate connections are detailed in Appendix A, a summary of the findings is given in Table 3-2, and Figure 3.68 serves as a reference for the discussed components. A description of the findings follows the table and figures.

*Table 3-2: Strongback Support Analytical Calculations Summary*

<b>Component</b>	<b>Applied Load</b>	<b>Failure Mode</b>	<b>Remedy</b>
<b>A: Si-Brz M8 Bolts</b>	1.5G, 6 kN	Slip	Rely on Dowel Pins
<b>B: 18-8 6MM Dowel Pins</b>	1.5G, 3 kN shear/pin	Yield	Adjust to 8mm, alloy steel
<b>C: SS304 Cone Plate</b>	2G Eq. Vert, 8 kN	Thread yield	Si-Brz Material
<b>D: 12.9 M12 Bolt</b>	2G Eq. Vert, 8 kN	None - PASS	N/A
<b>E: Si-Brz M10 Bolts</b>	4G Eq. Vert, 16 kN	None - PASS	N/A

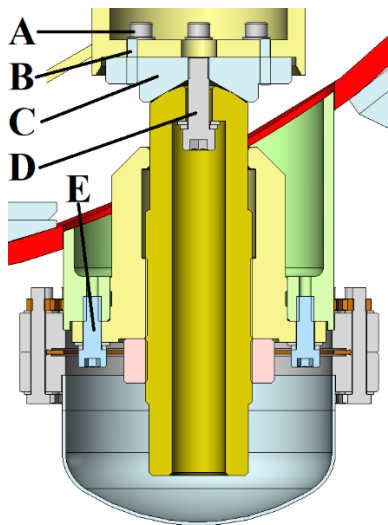


*Figure 3.68: Strongback Support Connections*

Four hundred kilograms is the maximum any one support bears, as the strongback and cold mass combined weigh 4800 kg, and the load is split across seven sets of supports. The supports at each end only accept half the load of those at the center of the module, and so the load of 4800 kg

is essentially divided among six pairs, leaving 800 kg per pair or 400 kg per support, which is equivalent to 4 kN at 1G.

The six bolts connecting the strongback and cone plate (**A**) did not yield in tension or shear but are insufficient to prevent slip due to 1.5G. As the bolt size couldn't be increased to provide additional holding force, the two alignment pins (**B**) were modified to accept the 1.5G shearing load. This was done by increasing their cross-sectional area and changing the material to a stronger alloy steel. The most axial load borne by the M12 bolt is during a downward 3G acceleration, which is a combination of tightening forces and 400 kg at 2G, which is a 3G acceleration but with the negation of gravity. This combined load was high enough that the threads of the cone plate (**C**) could yield, and when combined with vibration, the M12 bolt (**D**) could become loose. To remedy this, a stronger material, silicon bronze, was selected. The remaining bolts (**E**) were deemed satisfactory for a 4G vertical acceleration, which is an applied 3G and standard 1G from Earth's gravity. The bolts do not see a shearing load due to the fitment of the connected parts.

The mesh for the support was primarily solid swept hex, with shells used only for the vessel, as shown in Figure 3.69. It contained 33K nodes and 8K elements. Bonded contacts were used throughout. For structural analysis, forces were applied to the cone plate to emulate the supported mass of the strongback. For modal analysis, a point mass served this purpose. The two differed as the point mass did not yield realistic results for the structural analysis, but there was no other option for the modal analysis. It was therefore expected that the subassembly and combined modal analysis for the support will vary greatly. Additionally, the subassembly was tested with rotation allowed (free RDOF) and not allowed (fixed RDOF) at the cone plate. This was done as it was hypothesized the strongback would prevent any significant rotation.

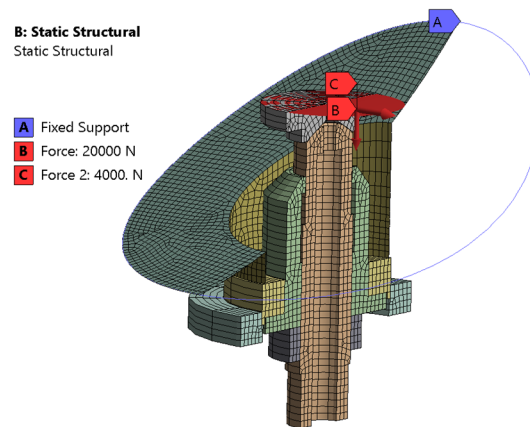


*Figure 3.69: Strongback Support Mesh and Boundary Conditions*

Modal analysis highlighted a potentially low-frequency mode in the transverse direction. The free RDOF analysis had a first mode of 9Hz while the fixed RDOF analysis was 20Hz. Due to the lack of well-defined boundary conditions for the modal analysis, the combined analysis was required to determine the true behavior. The mode shapes for each case are shown in Figure 3.70.

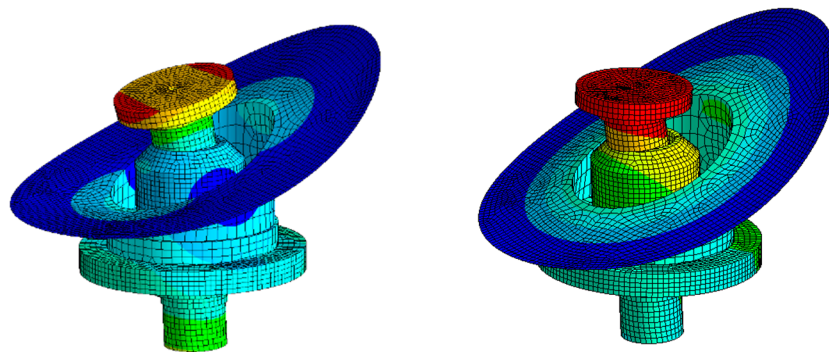


*Figure 3.70: Strongback Support Modes | Left: Free RDOF 9 Hz | Right: Fixed RDOF 20 Hz*

Structural analysis found no potential issues. The deformation and stress for the free RDOF analysis were greater than the fixed RDOF analysis. The highest stress was 142 MPa on the stud due to 5G, which occurred at the location of contact with the housing. The stud and housing were brought 0.1 mm closer, but the 0.2 mm radial clearance prevents contact. Both the axial deformation and stress are shown in Figure 3.71. For the fixed RDOF analysis, the stress and deformation were approximately halved.

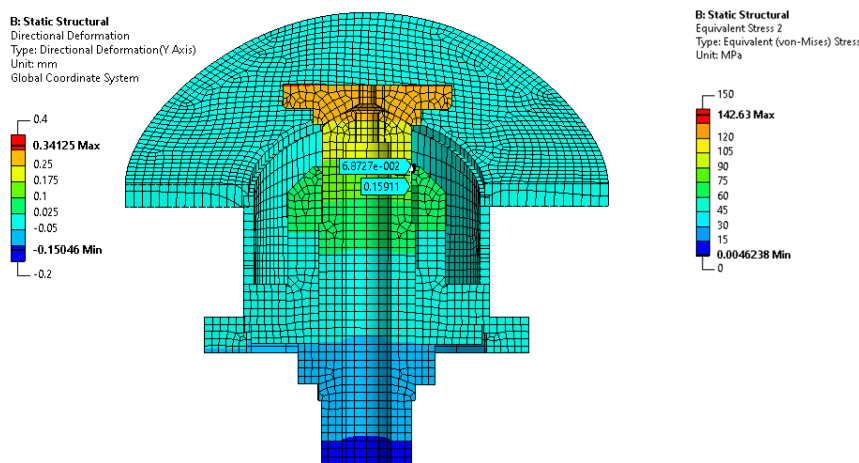
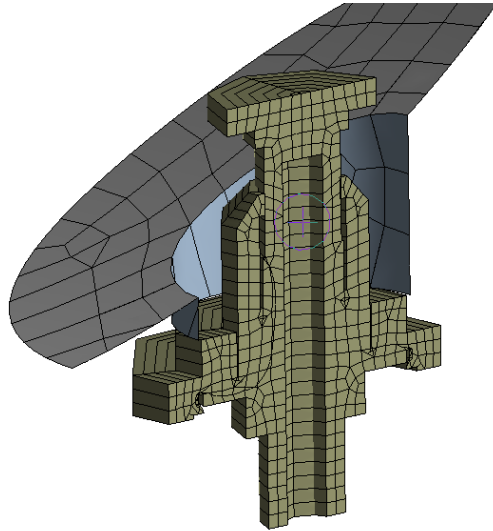


Figure 3.71: Strongback Support, 5G Load, Free RDOF | Left: Deformation | Right: Stress

The simplified model combined the solid components into a single body as this allowed for a swept mesh and it contained 3.6K nodes and 730 elements. This was justified as only bonded contacts had been used previously, and silicon bronze and stainless steel have similar Young's moduli and density. The material was set as stainless steel because its lower yield would make any issues of stress FOS apparent during later result analysis. The simplified model is shown in Figure 3.72.



*Figure 3.72: Strongback Support Simplified Mesh*

Overall, the behavior of the simplified model was fairly similar to the detailed model. The most notable difference was the lower deformation and higher stresses. The maximum stress was higher due to the presence of a sharp corner, where previously a bonded contact allowed for more flexibility. Outside of this small area, the stress magnitude and pattern matched well. As the modal results are similar, the higher stiffness indicated by the lower deformation was deemed acceptable. Table 3-3 shows a comparison of the results.

*Table 3-3: Simplified and Detailed Strongback Support Results Comparison*

<b>Model</b>	<b>Max Axial Def. (mm)</b>	<b>Max Eq. Stress (MPa)</b>	<b>Fixed RDOF 1<sup>st</sup> mode (Hz)</b>	<b>Free RDOF 1<sup>st</sup> mode (Hz)</b>
<b>Detail</b>	0.341	142	21.94	9.24
<b>Simplified</b>	0.294	230 (Singularity)	21.48	8.97
<b>Difference</b>	-14%	+62%	-2%	-3%

### 3.14 Vessel

The vessel geometry did not require significant simplification and was created with entirely shell mesh. The final mesh contained 35K nodes and 12K elements and is shown in Figure 3.73. Bonded contacts were used to attach the flanges and transportation mounts to the vessel weldment, but otherwise the mesh of the vessel was continuous. The fixed boundary was the faces of the transport mounts which attach to the isolator springs (Figure 3.74). A 4,800 kg point mass attached to where the strongback would have been, and the location was that of the cold mass. Additional point masses on the on ends of the beamline simulated the heavy gate valves.

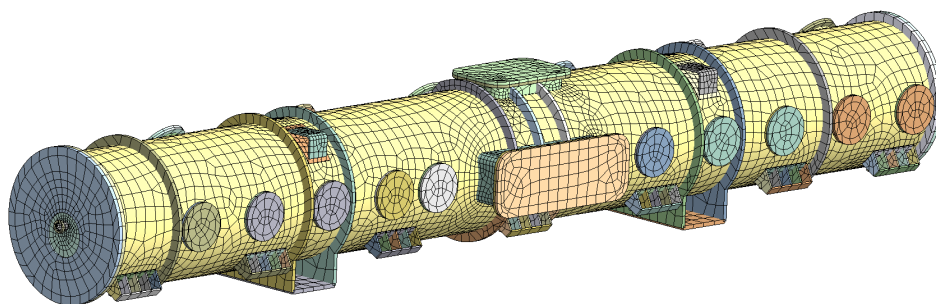


*Figure 3.73: Vessel Mesh*

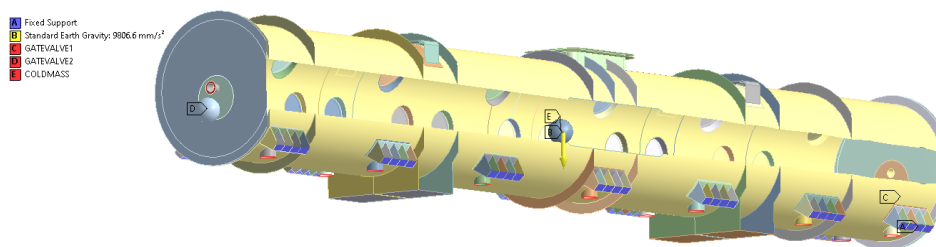


*Figure 3.74: Vessel Boundary Conditions*

Modal analysis of the vessel did not highlight any potential issues. The first mode of 32Hz was the transverse rocking of the pseudo-cold mass, the second mode of 36Hz was the transverse rocking of the entire vessel, and the third mode of 45 Hz saw the vertical movement of the gate valves. These mode shapes are shown in Figure 3.75. Previous modal analysis was not available for comparison.

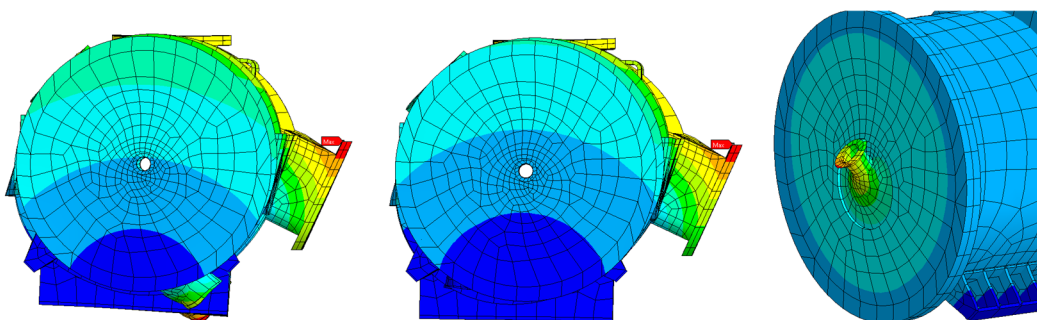


*Figure 3.75: Vessel Modes | Left: 32 Hz | Center: 36 Hz | Right: 45 Hz*

Structural analysis highlighted some areas of high stress, but ultimately no design changes were required. During 1.5G, a 162 MPa stress at the vessel-strongback connection extension was found. This response was expected to change with the addition of the strongback, as it should limit the bending at this location. Due to 5G, the transport mounts saw 205 MPa stress, which was at yielding. Because of this, the support was submodeled with a fine solid mesh, with full-penetration welds included. The resultant maximum stress was below yield outside the sharp corner of the weld toe, and discussion and result comparison with FNAL staff confirmed that design changes were not required. Figure 3.76, Figure 3.77, and Figure 3.78 show relevant structural results. The aforementioned FNAL analysis (Appendix B) had strong similarity with the presented results, each

identifying the transport supports as a high-stress area and having maximum support deformations of 0.4 -0.5 mm due to 5G [29].

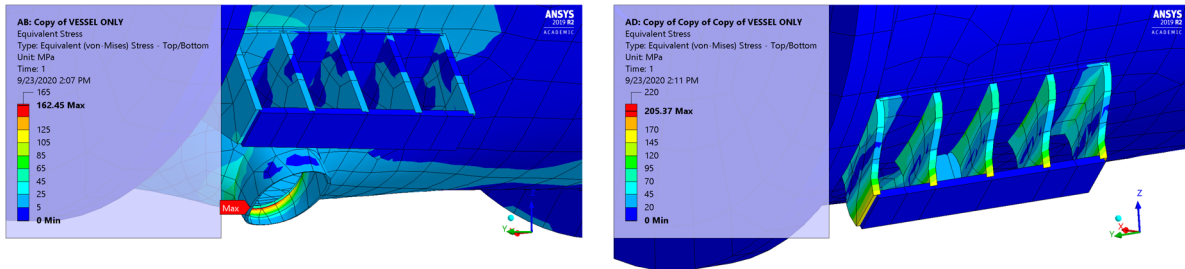


Figure 3.76: Vessel Structural Results | Left: 1.5G Stress | Right: 5G Stress

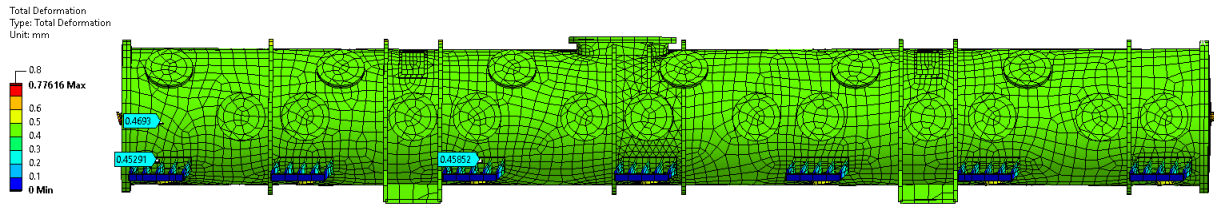


Figure 3.77: Vessel 5G Total Deformation

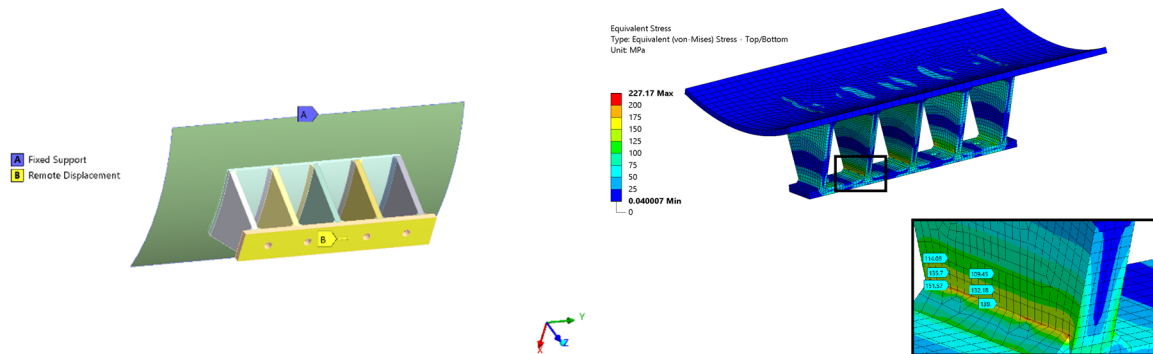


Figure 3.78: Transport Mount Submodel | Left: Boundary Conditions | Right: Stress

## **4. COMBINED SYSTEM RESULTS AND DISCUSSION**

The purpose of this chapter is to detail the analysis and results of each larger assembly within the cryomodule, which included the B90 and B92 cavity string sections, the cavity string, the vessel and strongback, and finally the full cryomodule. Each section includes discussion of boundary conditions, necessary analytical calculations, modal and structural results, any issues identified, and design changes made.

### **4.1 B90 Cavity String Section**

The B90 cavity string section combined the following subassemblies into a single analysis: the B90 cavity, the tuner, the coupler, and the cavity support. A point mass of 23 kg was used to mimic the effect of the two-phase pipe, and it attached at the cavity jacket. As previous, the support faces which mount to the strongback were given a fixed condition. The tuner and coupler were affixed with bonded contacts, and the nodes were aligned for better contact detection. Both the tuner and coupler retained their own point masses as previously detailed in Chapter 3. In total, this model contained 86K nodes and 23K elements, shown in Figure 4.1.

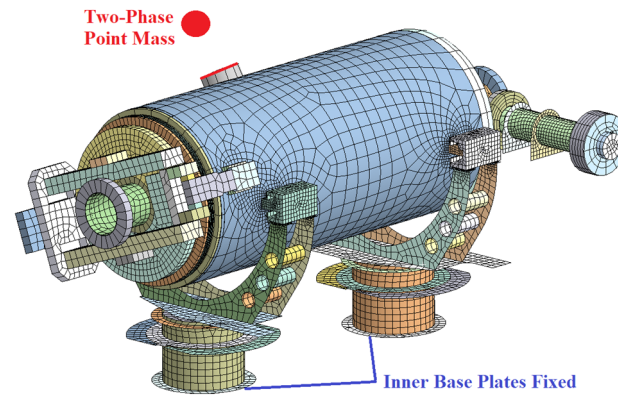


*Figure 4.1: B90 Cavity String Section Mesh and B.C.'s*

Modal analysis did not highlight any critical issues, and the results highlighted key differences between previous subassembly analysis and the larger assembly analysis. The first mode occurred transversely at 19 Hz- 1 Hz lower than previous. This is interesting as the previous model had a 300 kg mass for the cavity while the assembly only had 270 kg for the cavity and attached components. The lower frequency was caused by the heavy tuner, which is mounted so far to one side that the corresponding support resonates at a lower frequency, bringing down the overall system resonance. This was evident in the displacement, as the tuner side support saw higher overall displacement as compared to the coupler side. This behavior was not observed previously as the 260 kg point mass had been placed at the center of the cavity and did not account for the offset center of mass. This hypothesis was confirmed by retesting the subassembly of the cavity supports with an offset point mass, which lowered the resonant frequency.

The axial mode was found to be 23.1 Hz, which is more than the previous 21.3 Hz. This is explained since, in the cavity assembly analysis, the mass of the cavity and combined components is only 250 kg, not 300 kg. This is due to the 10% overestimation made previously, the missing intercavity bellows assembly, and small differences between the model created and the CAD. By

performing a simple natural frequency calculation, this new frequency can be confirmed as correct. By determining the equivalent stiffness of the subassembly in the axial direction, and then using this to compute the new natural frequency for  $m=250$  kg, the expected new frequency was found to be 23.3 Hz, which is a close match to the actual 23.1 Hz. The calculation is shown starting with Equation 4.1, and both the transverse and axial mode shapes are shown in Figure 4.2.

$$F_n = \sqrt{\frac{k_{eq}}{m}} \quad (4.1)$$

$$21.3 \text{ Hz} = \sqrt{\frac{k_{eq}}{300 \text{ kg}}} \quad K_{eq} = 136,107 \frac{N}{m}$$

$$F_n = \sqrt{\frac{136,107 \frac{N}{m}}{250 \text{ kg}}} = 23.3 \text{ Hz}$$

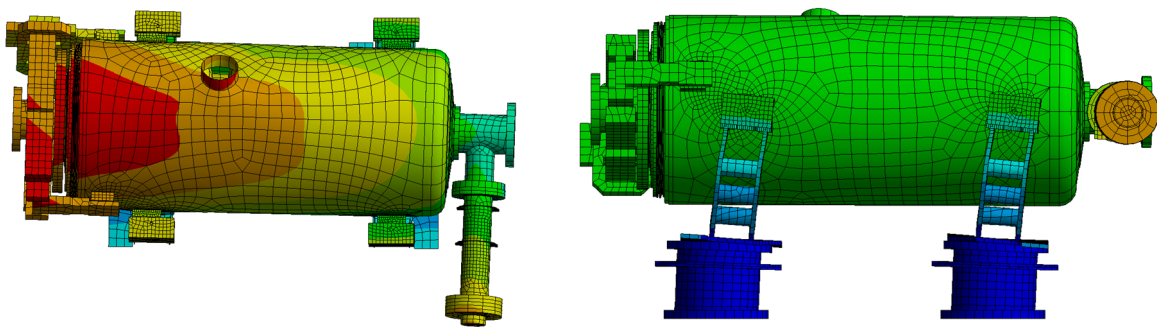
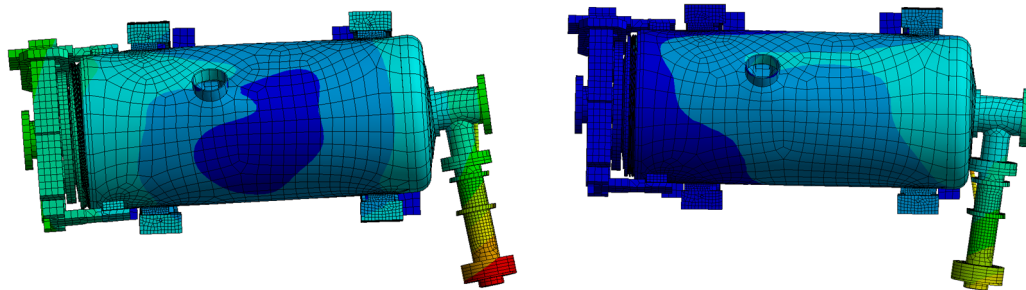


Figure 4.2: B90 Cavity Assembly Modes | Left: 19 Hz Transverse | Right: 23 Hz Axial

The third mode, occurring at 30 Hz, saw the twisting of the cavity around its center. Previously, this mode was not seen until above 70 Hz, and it is likely the tuner and coupler mounted far from the center of gravity lowered this mode frequency. Finally, the fourth mode of interest occurred at 34 Hz, with the independent movement of the coupler. Previously, this resonant frequency was not seen below 100 Hz and is explained by the longer cantilevered arm and that the beamline tube is not a perfectly rigid component. The coupler antenna still resonated at 37 Hz. Both the 30 and 34 Hz modes are shown in Figure 4.3.



*Figure 4.3: B90 Cavity Assembly Modes | Left: 30 Hz Twist | Right: 34 Hz Coupler*

Structural analysis did not highlight any major issues, although it did find an area of high stress not previously identified. The coupler tube on the beamline saw 45 MPa stress, slightly higher than the 38 MPa yield, during 3G vertical. This is shown in Figure 4.4, along with the coupler deformation during 3G. In actuality, this high stress will not occur as foam blocks between the coupler and vacuum vessel will prevent the downward deflection, and so it was not of great concern. Otherwise, results from previous analysis matched well with the updated analysis. As expected, the stress in the bellows and cavities was somewhat increased due to the tuner, but at 94

MPa and 15 MPa, respectively, remained below yielding. The stress in the supports saw similar patterns and slightly lower magnitudes compared to before for 5G, which is understandable as the cavity mass was considerably reduced. A comparison is shown in Figure 4.5. The coupler antenna saw deflections low enough that the base of the antenna would have stresses below yield.

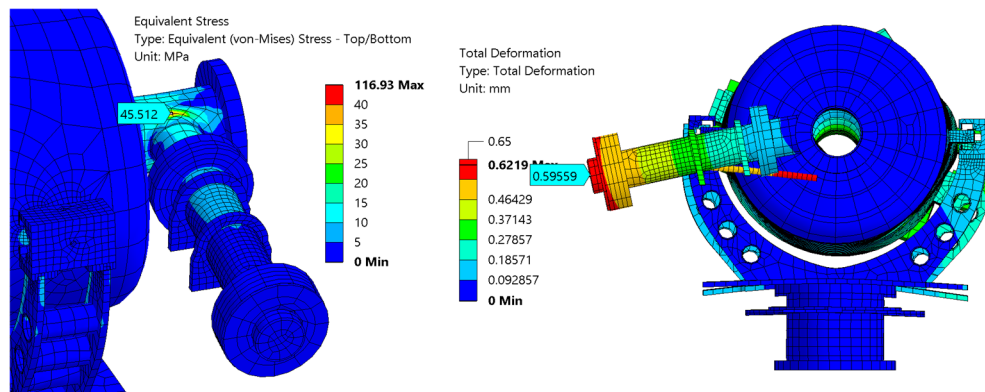


Figure 4.4: Coupler 3G Results | Left: Stress | Right: Deformation

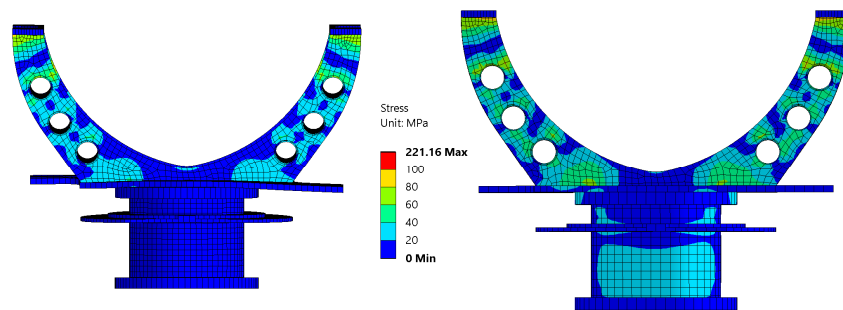
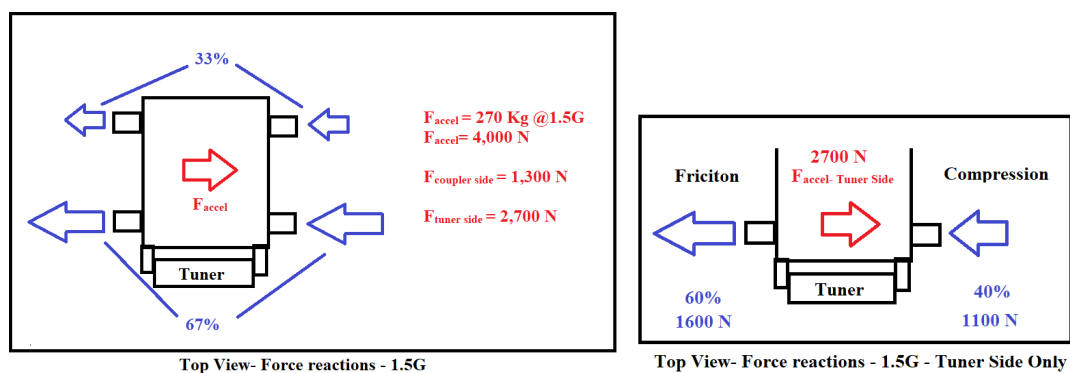


Figure 4.5: Cavity Support 5G Stress | Left: Assembly Results | Right: Subassembly Results

While the results will not be presented in any detail, a comparison of the response with the full needle support geometry vs the simplified was made. It confirmed that the overall deflections, stresses, and modal frequencies were near identical between the two.

As previously stated in Chapter 3, due to the critical nature of the cavity alignment, the estimation of maximum possible sliding was delayed until the more accurate assembly could be used. By evaluating the reaction forces at each needle support during 1.5G with no sliding, the load distribution was determined, as shown in Figure 4.6. It was found that the tuner side support accepts 67% of the total cavity load, and for that support, the side in tension accepts 60% of the load and the side in compression accepts 40%. Based on a cavity mass of 270 kg (less conservative estimate used as a built-in FOS was not necessary), the side in tension can see 1,600 N of separation forces, which would cause slip to occur. As the exact normal forces and friction coefficients for the needle support were unknown, a worst possible case was evaluated.



*Figure 4.6: 1.5G Sliding Load Distribution*

An acceleration event occurs of the form shown in Figure 4.7. The initial acceleration is in the positive direction and is then followed by negative acceleration in the opposite direction. If the initial acceleration were large enough to cause slip, but the return acceleration was of a slightly lower magnitude and did not cause slip to occur, it would leave an open gap between the cavity lug and needle bearing. Data from the LCLS-II transports was studied and it was found

that some higher magnitude accelerations had this hypothesized behavior, typically with the return acceleration being no less than 80% the magnitude of the original acceleration.

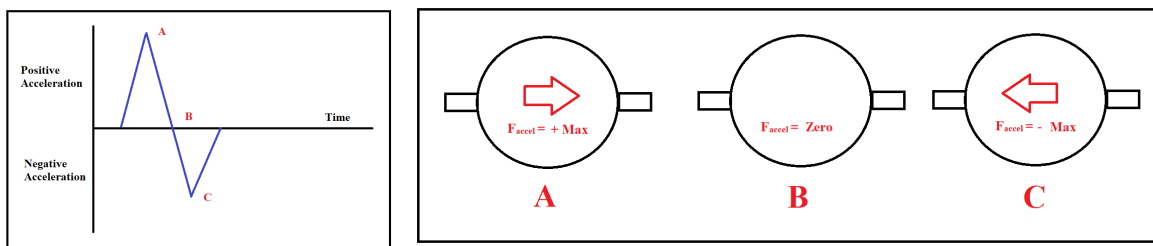


*Figure 4.7: Acceleration Event Diagram*

For this case, if the maximum static friction force was 1,550 N and the sliding friction force was 1,000N, it would allow a gap to form. Between the acceleration events when the  $F_{\text{accel}} = 0$  N, the lug sees some force pushing it back, as the support is in a deformed state. During the negative acceleration event, the returning force is additive with this “spring” force from the support. The maximum spring force which is not overcome by the return acceleration is approximately 600N, and for brevity, the details of this estimation are in Appendix B.

To determine the effect on cavity alignment, further analysis was conducted. On one side of each support, transverse movement was allowed, a 600 N force was placed on each lug in the positive transverse direction, and a 600N force in the opposite direction was placed on each needle support. This is illustrated in Figure 4.8.

The results of this analysis revealed that, in a worst case, the cavity would move outside the alignment tolerance. As shown in Figure 4.9, 0.61 mm of separation occurs between the lug and the needle block, and the cavity cells move by 0.41 mm. As the position of the cells is most critical, their displacement is what was compared to the 0.25 mm alignment value.

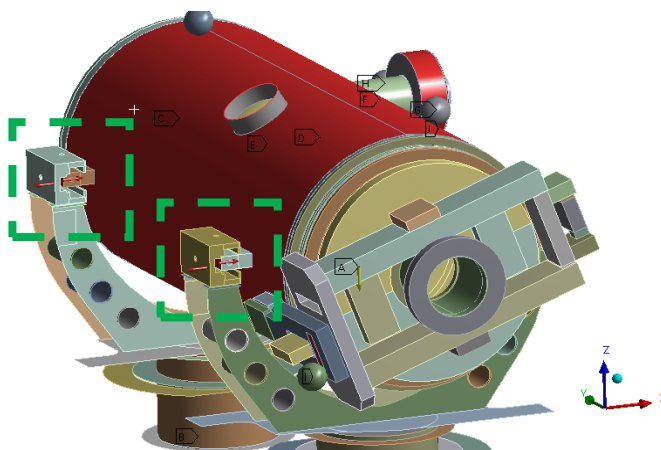


Figure 4.8: Applied Separation Forces

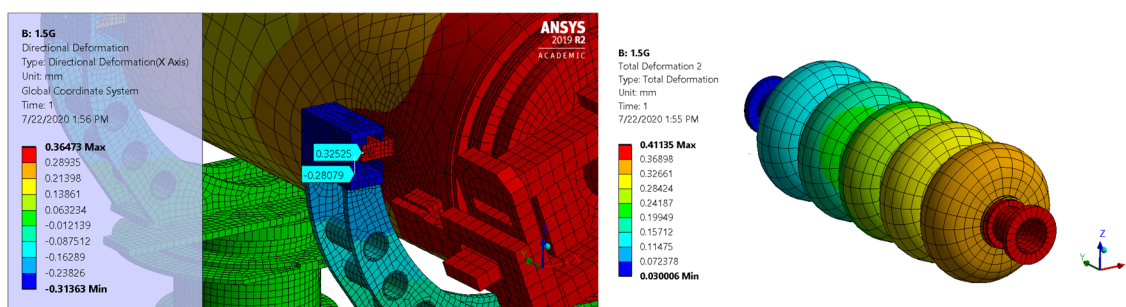


Figure 4.9: 1.5G Sliding Worst Case Deflections | Left: Lug Separation | Right: Cells Position

As it would be very difficult to realign the cavity string after transport, the decision was made to alter the cryomodule design to prevent such a misalignment. It was not allowable to connect from the needle support to the cavity for two reasons: the available space on the lug between the magnetic shield and the needle support was only 10mm, and the design of the cavity jacket could not be altered as it was already in production. For these reasons, the decision was made to increase the stiffness of the support in the transverse direction to limit the possible misalignment.

After several iterations, the design shown in Figure 4.10 was settled on. This design was the effort of a collaboration of both the author and FNAL staff. The central section is made of a solid block of Ti-2, and the arm design used a box frame design, both of which added rigidity when compared to the previous design. For the final design, 0.28 mm of separation occurred between the lug and the bearing, with the cavity cells moving only 0.19 mm. These results are shown in Figure 4.11.

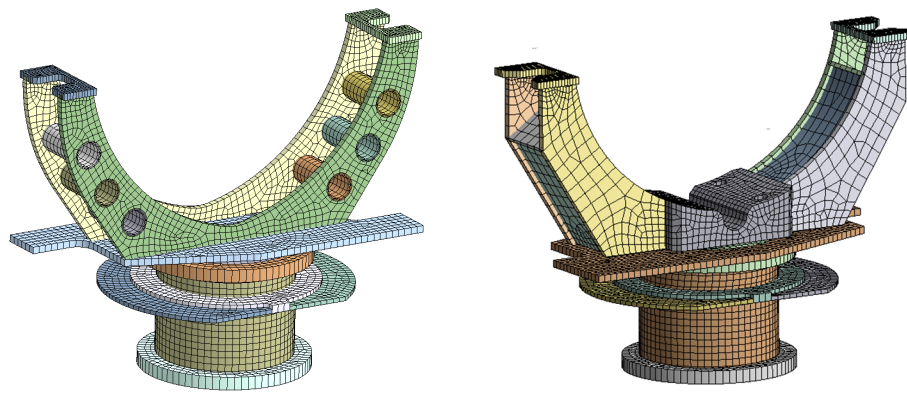


Figure 4.10: Cavity Support | Left: Previous Design | Right: Stiffer Design

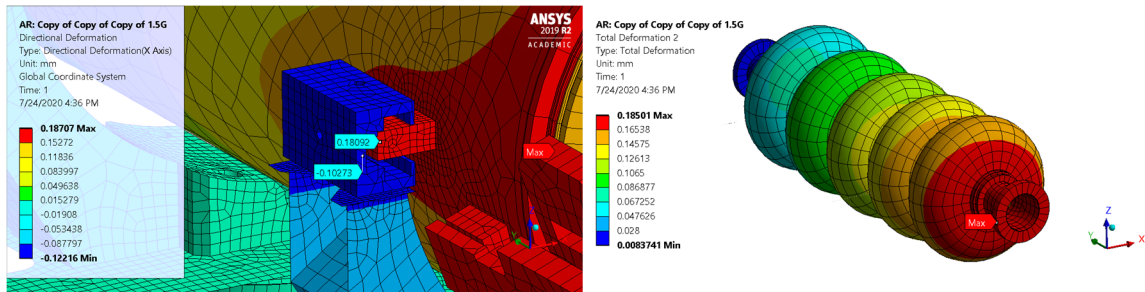
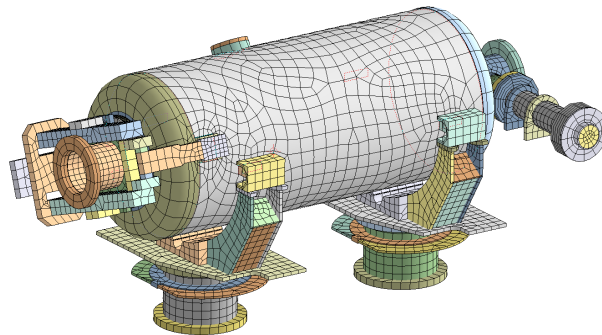


Figure 4.11: Updated Design Worst Case | Left: Lug Separation | Right: Cells Position

With the new support design, the modes of the B90 cavity assembly increased to 22 Hz transverse and 29 Hz axial. The twisting mode and the coupler modes occurred at the same frequencies as before. The maximum stress in the support was found to be 70 MPa due to 5G, well below the yield of 275 MPa. Stresses in the bellows and niobium cells were also checked and were within their respective limits.

## 4.2 B92 Cavity String Section

The combined analysis with the B92 cavity included the updated design of the cavity supports. The boundary conditions were the same as for the combined B90 analysis and are not discussed for brevity. The final mesh contained 46K nodes and 14K elements and is shown in Figure 4.12.



*Figure 4.12: B92 Cavity String Section Mesh*

The modal results did not highlight any issues, and results were largely similar to the B90 assembly results. The transverse mode occurred at 21 Hz, axial at 29 Hz, and the coupler and assembly moved in a twisting motion at 33 Hz. Other modes, such as for the coupler antenna, were similar to those identified in the subassembly analysis. As the mode shapes are similar to those previously shown in Figure 4.2 and Figure 4.3, they are not shown.

The structural analysis results did not highlight any issues and were largely similar to the B90 assembly results and results from the B92 cavity subassembly analysis. Components such as the bellows, niobium cells, and cavity supports had deflections like previous and with stresses within the allowable limitations.

### 4.3 Cavity String

The cavity string assembly used seven separate mechanical models that were combined to form the string, one for the two-phase pipe and one for each cavity section of the string. The beamline bellows were included, and the end bellows were given fixed conditions where they attach to the vacuum vessel. Bonded contacts were used to connect the separate subassemblies, and the nodes of the mesh were aligned to ensure proper contact detection and behavior. As previous, the lower faces of each cavity support were given a fixed condition. Due to time constraints and the low likelihood of significant result differences, the 2K line and 5K line were not included. Before the model was created, the mesh for each cavity assembly was made coarse while retaining correct behavior. In total, the string contained 423K nodes and 125K elements. A view of the full string mesh is shown in Figure 4.13; while a view of one section and its boundary conditions is shown in Figure 4.14.

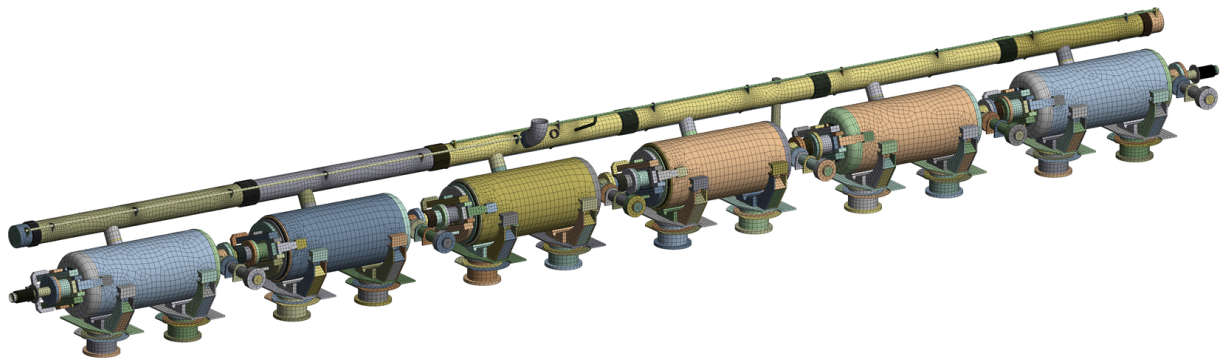


*Figure 4.13: Cavity String Mesh*

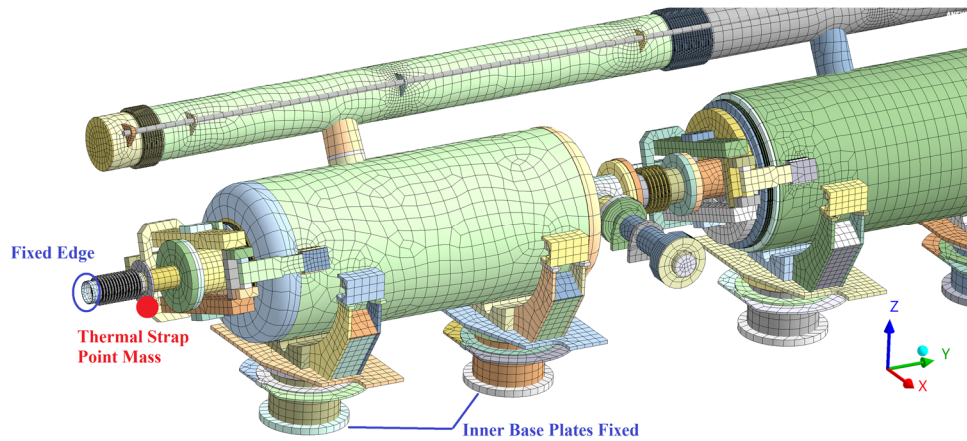


*Figure 4.14: Cavity String Mesh Detailed View and Boundary Conditions*

Modal analysis did not find any issues with the string but highlighted some key differences from the subassemblies. The primary difference was the increased flexibility of the two-phase pipe. Given that the subassembly considered the edge which attached to the jacket as fixed, it was not surprising that a deformable connection allowed for much less rigidity. The first mode occurred at 21 Hz with the entire string moving transversely, which is only 1 Hz lower than the cavity assembly analysis, and this was likely due to the two-phase pipe geometry being more flexible than a simple point mass. The following mode occurred at 23 Hz, which saw the end sections of the two-phase pipe flexing, as shown in Figure 4.15. Previously, this occurred at 34 Hz and is explained by the difference in boundary conditions.

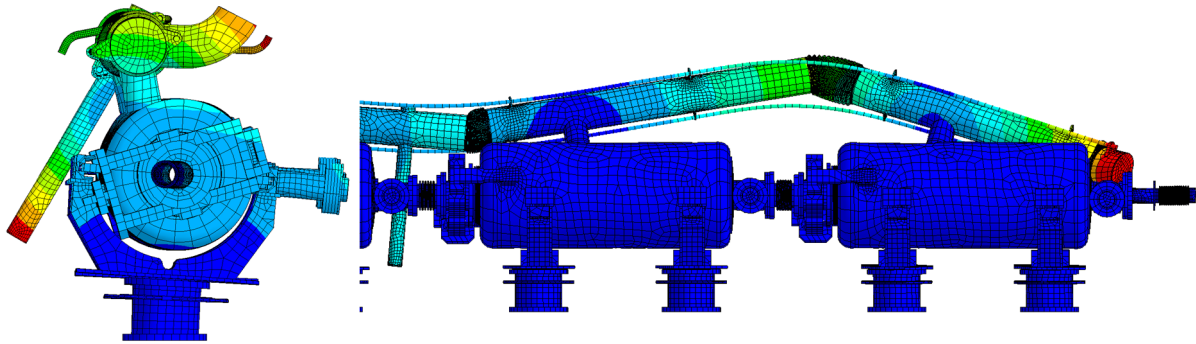


*Figure 4.15: Cavity String Modes | Left: 21 Hz | Right: 23 Hz*

Other modes of interest included the axial movement of a single cavity, which occurred at 30 Hz. Previously this occurred at 29 Hz, and the slight increase is likely due to the intercavity bellows stiffness and the two-phase pipe providing additional rigidity. Other modes, such as the coupler at 34 and 37 Hz, remained identical. Lastly, a mode which saw opposing movement of alternating cavities in the transverse direction occurred at 27 Hz. As this frequency is sufficiently high, it is unlikely to produce any damage to the bellows. The axial and alternating mode shapes are shown in Figure 4.16 and Figure 4.17, respectively.

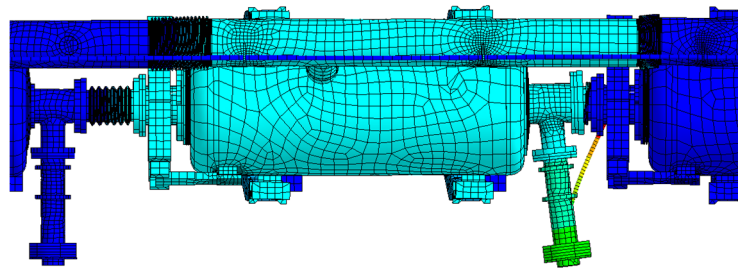


*Figure 4.16: Axial Mode Shape 30 Hz*

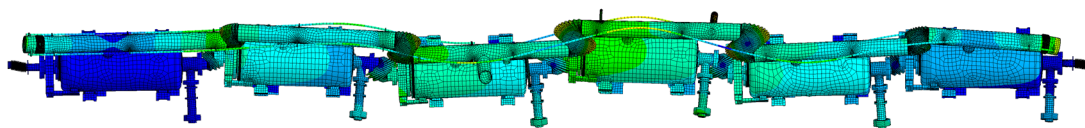


*Figure 4.17: Transverse Alternating Mode Shape 27 Hz*

Structural analysis highlighted one design adjustment that was necessary. Results for the cavities and their components were largely the same as previous, with bellows and niobium cell stresses below allowable. The two-phase pipe saw a significant increase in stress at one of its central bellows, with 207 MPa during 5G, 1.65 mm of transverse deflection, shown in Figure 4.18. Previously, this bellows only saw 80 MPa of stress, and the change is due to the increased flexibility of the two-phase pipe, as deformation is a driving cause of stress in a bellow. As this was above the yield of SS316L and the fatigue life was below allowable at 167,000 cycles, an additional rod guide was added before the bellow to prevent this movement. This reduced the transverse deflection to 1.32 mm, the maximum stress to 168 MPa, and improved the fatigue life to 412,000 cycles. A comparison of their vertical deflections is shown in Figure 4.19. While still near yielding, these results were found to be acceptable as the bellow did not see any low-frequency resonance, and the fatigue life was above the minimum allowable. The highest stress in a beamline bellows occurred during 5G with 98 MPa. The maximum axial and transverse displacement, maximum equivalent stress, and predicted fatigue life for each type of bellow were verified to be within the allowable limits, and a tabulation of these results for the final model is shown in Section 4.5.

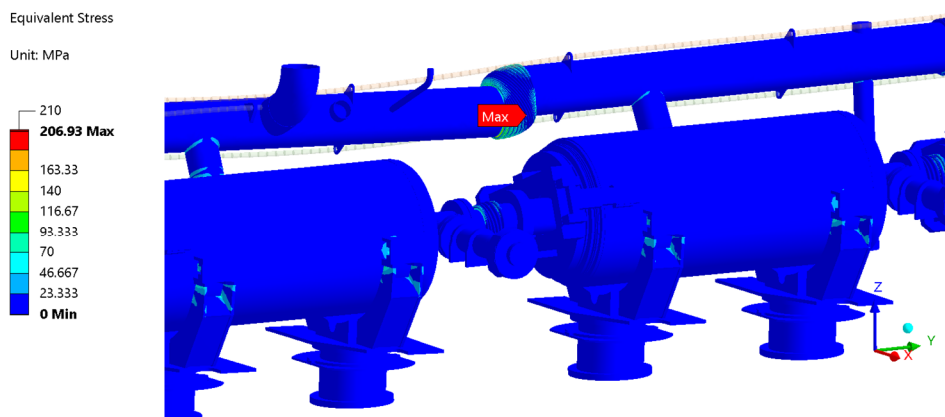


Figure 4.18: 5G Stress at Two-Phase Bellows

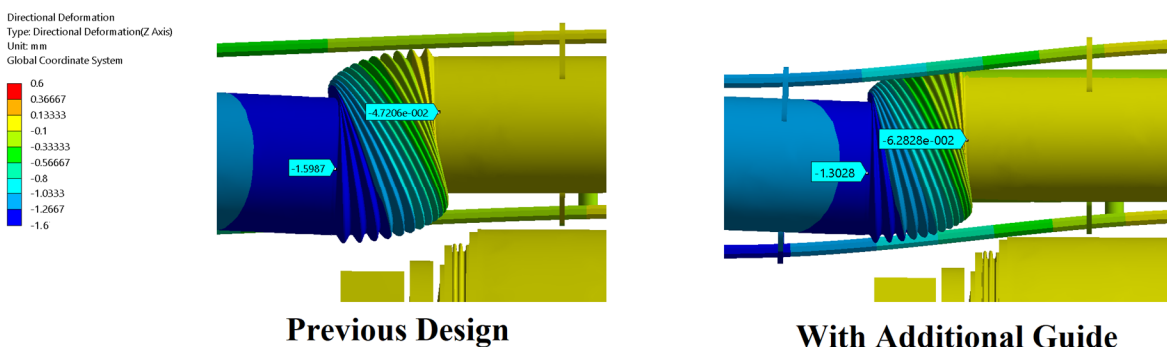
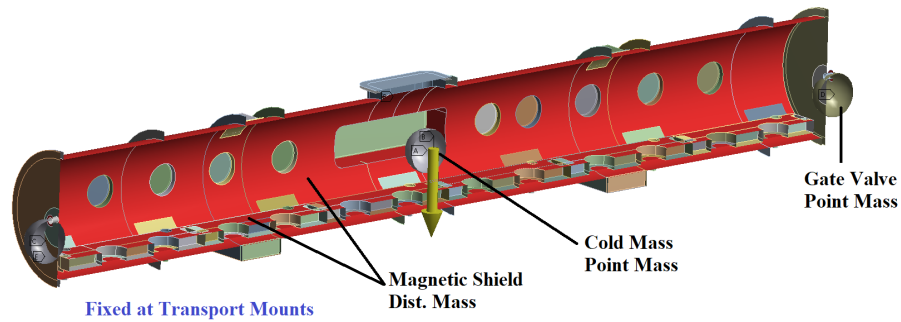


Figure 4.19: Bellows Deflection Comparison | Left: Previous | Right: With Guide

#### 4.4 Vessel and Strongback

As the strongback and vessel were modeled within the same model, there was no need to combine models for the analysis. The boundary conditions were similar to those previous, with the vessel being fixed at its transport mounts and with point masses for the gate valves. A 4,000 kg point mass attached to the strongback where the support posts would. The point mass behavior was rigid at the faces, and a distributed mass was included to mimic the magnetic shield; and all

these conditions are shown in Figure 4.20. Bonded contacts connected the strongback, supports, and vessel. The mesh contained 106K nodes and 28K elements, shown in Figure 4.21.



*Figure 4.20: Vessel and Strongback Boundary Conditions*

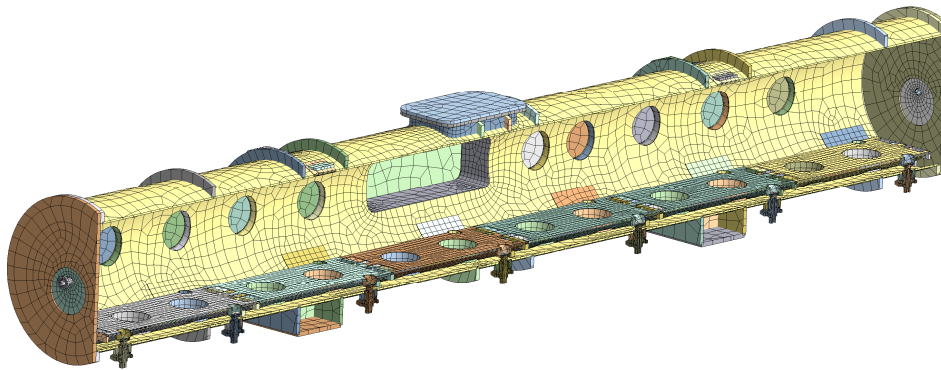


*Figure 4.21: Vessel and Strongback Mesh*

Modal analysis did not highlight any key issues, but it did confirm expected differences for the strongback mode frequencies. As expected, the transverse mode dropped significantly, reaching 23 Hz, which is shown in Figure 4.22. As compared to the subassembly analysis of the strongback support, the results more closely match the support that had its RDOF constrained, which saw a mode of 20 Hz. The transverse vessel mode remained at 37 Hz as before.

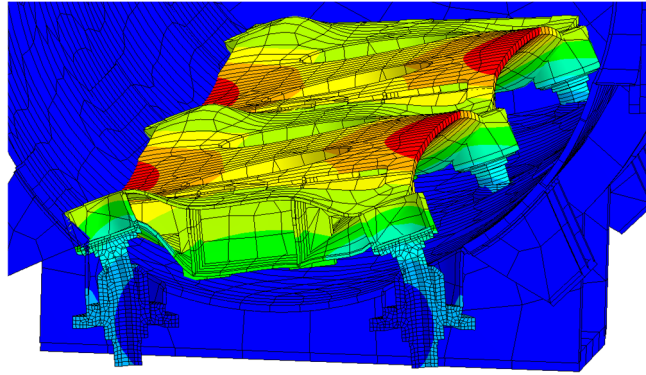


*Figure 4.22: Strongback Transverse Mode 23 Hz*

Structural analysis did not highlight any key issues but did confirm the methods of the subassembly analysis for each component. The stress at the vessel during 5G was only slightly higher due to the inclusion of the magnetic shield weight. The deformation across the transport mounts was previously 0.46 mm, and it increased slightly to 0.48 mm. The strongback supports had a maximum stress of 98 Mpa due to 5G and 84 Mpa due to 1.5G, both of which were below the subassembly estimate of 140 Mpa. This was due to the lower deformations seen by the supports when compared to the subassembly results, and this difference was due to the inability of either tested method to accurately capture the support behavior. The strongback exhibited similar stress levels, stress patterns, and relative deformations as previous.

#### **4.5 Full Cryomodule**

The final analysis combined the cavity string, vessel with strongback, and the thermal shield. As before, the vessel was fixed at its transport mounts. Bonded contacts were used throughout to connect the components, except for the thermal shield and vessel, which used no separation contacts to allow for sliding of the G10 bumpers. In total, the mesh contained 601K nodes and 178K elements. To solve the first 50 modes took 30 minutes on a computer with a recent 8 core I9 processor. The mesh is shown in Figure 4.23.

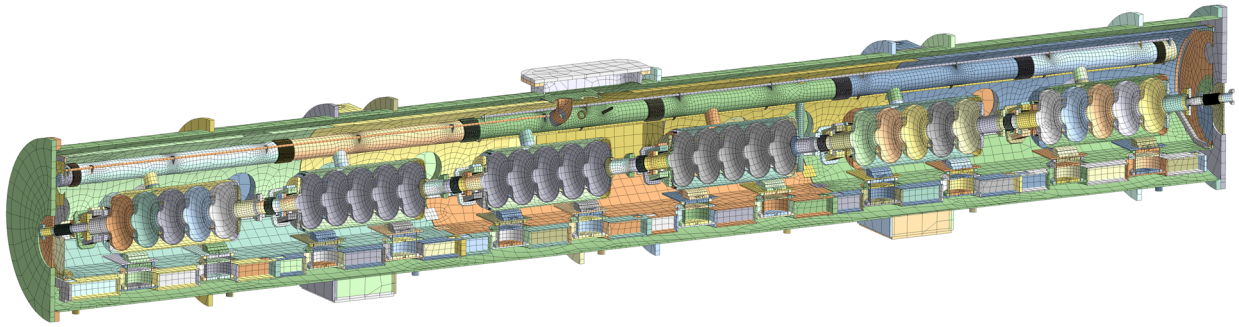


*Figure 4.23: Cryomodule Mesh*

The modal analysis did not highlight any major differences from previous analysis, and as expected, mode frequencies generally decreased with the increased system flexibility. The cavity string moved transversely on the strongback at 18 Hz, 3 Hz lower than previously, as shown in Figure 4.24. The thermal shield also saw a drop to 20 Hz, and the first axial cavity mode dropped to 27 Hz. Each of these differences is explained by the comparison of previous boundary conditions with the updated, less rigid conditions. While the cavity string saw resonance at 18 Hz and transversely at other frequencies in the low 20's, this was not of great concern, as any such resonance would occur with very low magnitude, as discussed in the following paragraph.

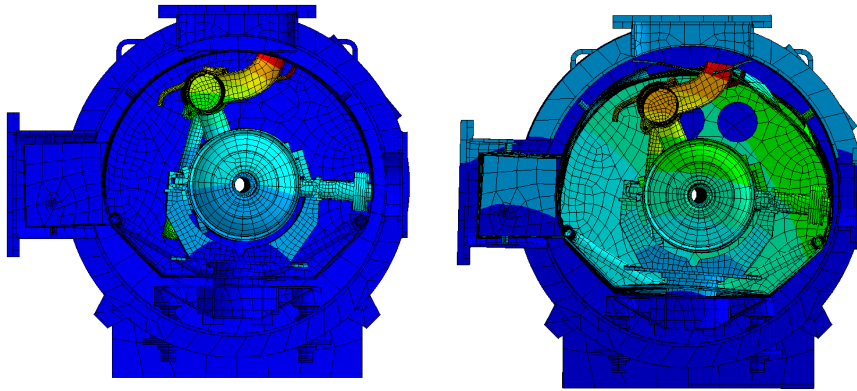


*Figure 4.24: Cryomodule Results | Left: 18 Hz Mode | Right: 1.5G Deformation Shape*

Structural analysis did not highlight any issues and only served to confirm the results of previous analysis. During 1.5G, the bellows connecting the cavity string and vessel saw 1 mm of transverse displacement, slightly higher than before, but still well within the maximum of 3 mm. The results for all bellows are shown in Table 4-1. As the 1.5G deformation and 18 Hz mode shape have similar deflection patterns (Figure 4.24), it is assumed the resonant frequency would exhibit similar deflections and stresses, and so the 18 Hz resonant frequency is not of concern because this movement does not occur with sufficient magnitude to cause harm to any critical components, such as the beamline bellows. Additionally, the change made to the central section of the two-phase pipe made a significant difference in the fatigue life, increasing the cycles from 138,000, which was below the minimum of 240,000 to 260,000 cycles. These values are lower than those reported for the cavity string because the two-phase pipe saw higher deformations in the full model.

*Table 4-1: Cryomodule Bellows Results*

<b>Bellows</b>	<b>Max Axial Disp.</b>	<b>Axial Limit</b>	<b>Max Tran. Disp.</b>	<b>Trans. Limit</b>	<b>Max Stress</b>	<b>Fatigue Cycles</b>
Beam Pipe	1.73 mm (5G)	12 mm	0.96 mm (1.5G)	5 mm	85 MPa (5G)	1,230,000
Two-Phase Center - Previous	0.44 mm (5G)	6 mm	1.74 mm (5G)	2 mm	213 MPa (5G)	138,000
Two-Phase Center- Updated	0.44 mm (5G)	6 mm	1.47 mm (5G)	2 mm	188 MPa (5G)	260,000
Two-Phase Ends	0.10 mm (5G)	6 mm	0.11 mm (5G)	2 mm	31 MPa (3G)	>1e7
Intercavity	0.79 mm (5G)	10 mm	0.50 mm (5G)	3 mm	121 MPa (5G)	475,000

## **5. RESULTS SUMMARY AND FUTURE WORK**

The objectives of this thesis were the following: to evaluate the HB650 cryomodule design for transportation conditions using modal and structural analysis, to improve any components found to not meet the established criteria, and to gain understanding of how the system response changes as model complexity increases.

Several components were identified as unsatisfactory per the established criterion, which included the magnetic shield, two-phase pipe, cavity supports, strongback supports, and heat exchanger. In collaboration with FNAL engineering staff, design changes were made to each component which allowed each to meet the necessary criteria and mitigated the risk of failure due transportation. Table 5-1 details each design change made and its impact, as well as other results of the HB650.

The method of analysis, whereby individual detailed analyses were combined to form a more complex system, proved to be an effective mechanism of study for the HB650. In general, as the model became more complex and the fixed boundary locations farther from the areas of interest, the resonant frequencies decreased as the system became less stiff. Other behavior, such as stress and deformation of a particular system, varied only somewhat from the original subassembly analysis. Testing of each subassembly using a fine mesh followed by simplification

for the larger model, allowed for only modest computational requirements, and could serve as a guiding method for future analyses of similarly complex systems.

*Table 5-1: Summary of Results*

Sub-Assembly	Issues Found?	Design Changes
Coupler	No	n/a
Tuner	No	n/a
Cavities	No	n/a
Cavity Supports	Yes	Stiffness increased to prevent misalignment. Bolt sizings increased to prevent yield.
Two-Phase Pipe	Yes	Bellows placement changed, guides added, low cycle fatigue eliminated. Guide added for sensor plate to eliminate low frequency resonance.
Heat Exchanger	Yes	Support attaching from vessel to heat exchanger added to prevent movement.
Cryogenic Lines	No	n/a
Pumping Support	No	n/a
Thermal Shield	Yes	Mounting location at support strengthened to prevent slip during 5G.
Magnetic Shield	Yes	Additional supports added to prevent low resonance and yield due to 5G.
Strongback	No	n/a
Strongback Supports	Yes	Larger dowel pins and certain component materials adjusted to accommodate 5G loading.
Vacuum Vessel	No	n/a

There are several investigations which would benefit further study. As certain subassembly results saw a significant difference compared to the final analysis, it would be beneficial to study what boundary conditions would have allowed for the difference to be minimized. For example, the two-phase pipe could be analyzed with pseudo-cavity jackets to allow for more flexibility or the strongback could be evaluated with the supports but no vessel. These changes would have minimal impact on the computational requirements but could greatly improve the predictive power of future analyses of individual components. As it relates to the full assembly, the inclusion of

smaller components and the use of bushing elements to allow for a less rigid connection from the vessel to the “frame” would be of interest. Finally, once the HB650 fabrication is sufficiently mature, it would be beneficial to validate the results of this thesis against experimental measurements. This could include impact testing for modal frequencies or purposeful elastic deformation of select components. Both would require additional analysis with updated boundary conditions to best approximate the as-built cryomodule.

## REFERENCES

- [1] D. Kubik, "Fermilab Accelerator," 2005. [Online]. Available: <https://home.fnal.gov/~kubik/Accelerators/Fermilab.pdf>. [Accessed 20 October 2020].
- [2] Fermilab National Accelerator Laboratory, "Proton Improvement Plan-II," Batavia, 2013.
- [3] W. Singer et al., "RRR-Measurement Techniques on High Purity Niobium," DESY, Hamburg, 2010.
- [4] F. G. Garcia, "PIP-II Linac Installation and Commissioning External Review: Scope/BOE/VE," 4 March 2019. [Online]. Available: <https://indico.fnal.gov/event/19887/>. [Accessed 12 September 2020].
- [5] V. Bocean et al., "Referencing and Stability Studies of the Fermilab 3.9 GHz Cryomodule for DESY TTF/Flash," in *The 10th International Workshop on Accelerator Alignment*, Tsukuba, 2008.
- [6] M. W. McGee et al., "Transport of LCLS-II 1.3 GHz Cryomodule to SLAC," Fermilab, Batavia, 2016.
- [7] M. W. McGee et al., "Transatlantic Transport of the Fermilab 3.9 GHz Cryomodule to DESY," in *Partical Accelerator Conference*, Vancouver, 2009.
- [8] E. Harms et al., "Third Harmonic System at Fermilab/Flash," in *SRF 2009*, Berlin, 2009.
- [9] N. Huque et al., "Improvements To LCLS-II Cryomodule Transportation," in *SRF 2019*, Dresden, Germany.
- [10] P. Neri et al., "Development of a Suspension System for the Road Transportation of Cryomodule SSR1 Through a Multilevel Finite Element-Multibody Approach," in *SRF2019*, Dresden, Germany, 2019.
- [11] M. Kane, "HB650 Transport Frame FDR Design Overview," STFC, Daresbury, 2020.
- [12] S. Barbanotti et al., "XFEL Cryomodule Transport: From the Assembly Laboratory In CEA\_Saclay (France) to the Test-Hall In Desy-Hamburg (Germany)," in *LINAC 2014*, Switzerland, 2014.
- [13] T. Whitlatch et al., "Shipping and Alignment For The SNS Cryomodule," Thomas Jefferson National Accelerator Facility, Newport News.
- [14] S. Barbanotti et al., "Monitoring The Flash Cryomodule Transportation From DESY Hamburg to CEA Saclay: Coupler Contact, Vacuum, Acceleration and Vibration Analysis," FERMILAB, Batavia, 2009.

- [15] S. Barbanotti et al., "Modal Analysis of the XFEL 1.3 GHz Cavity and Cryomodule Main Components and Comparison With Measured Data," in *19th Int. Conf. on RF Superconductivity*, Dresden, 2019.
- [16] T. J. Jones, "Design of the High Luminosity Large Hadron Collider Crab Cavity Support System," Lancaster University, Lancaster, 2020.
- [17] S. Barbanotti et al., "Measurement of the Vibration Response of the EXFEL RF Coupler and Comparison With Simulated Data (Finite Element Analysis)," in *19th Int. Conf. on RF Superconductivity*, Dresden, 2019.
- [18] S. Cheban, "PIP-II 650 MHz High Beta Cryomodule Preliminary Design Review," 11 December 2019. [Online]. Available: <https://indico.fnal.gov/event/22509/>. [Accessed 5 April 2020].
- [19] Y. Pischalnikov, "PIP-II 650 MHz High Beta Prototype Cryomodule Final Design Review - Tuner introduction and activities at FNAL," 31 July 2020. [Online]. Available: <https://indico.fnal.gov/event/43274/>. [Accessed 5 September 2020].
- [20] Deakin University, "Magnetic Field Guidelines," August 2009. [Online]. Available: [https://www.deakin.edu.au/\\_\\_data/assets/pdf\\_file/0004/228649/magnetic-fields-guidelines.pdf](https://www.deakin.edu.au/__data/assets/pdf_file/0004/228649/magnetic-fields-guidelines.pdf). [Accessed June 2020].
- [21] J. Holzbauer, "PIP-II HB650 Cryomodule Transportation Specification," FNAL, Batavia, 2020.
- [22] American Society of Mechanical Engineers, Boiler and Pressure Vessel Code, New York: American Society of Mechanical Engineers, Boiler and Pressure Vessel Committee, 2015, pp. 489-512.
- [23] E. Cheever, "Eigenvalues and Eigenvectors," Swarthmore , 2005. [Online]. Available: <https://lpsa.swarthmore.edu/MtrxVibe/EigMat/MatrixEigen.html>. [Accessed April 2020].
- [24] N. Nigam, "PIP-II 650 MHz Coupler Proto-Final Design Review," 11 February 2020. [Online]. Available: <https://indico.fnal.gov/event/22769/>. [Accessed 4 October 2020].
- [25] N. Nigam et al., "PIP-II 650 MHz  $\beta=0.9$  Jacketed Cavity Engineering Analysis Report ED0010266," FNAL, Batavia, 2019.
- [26] N. K. Sharma, "Cavity Design : PIP-II 650 MHz  $\beta=0.90$  &  $0.92$  Jacketed Cavity Prototype Final Design Review," Fermilab National Accelerator Laboratory , Batavia, 2019.
- [27] The Engineering Toolbox , "Friction and Friction Coefficient," 2004. [Online]. Available: [https://www.engineeringtoolbox.com/friction-coefficients-d\\_778.html](https://www.engineeringtoolbox.com/friction-coefficients-d_778.html). [Accessed 6 May 2020].
- [28] M. La Croix, "PIP-II 650 MHz High Beta Prototype Cryomodule Final Design Review - Strongback," 31 July 2020. [Online]. Available: <https://indico.fnal.gov/event/43274/>. [Accessed 22 August 2020].

- [29] M. Chen, "PIP-II 650 MHz High Beta Prototype Cryomodule Final Design Review - Vacuum vessel (Structural analyses)," 31 July 2020. [Online]. Available: <https://indico.fnal.gov/event/43274/>. [Accessed 3 August 2020].
- [30] C. Kumar et al., "Canteliver Beam With Tip Mass At Free End Analysis By FEM," *International Journal Of Scientific Research And Education*, vol. 2, no. 7, pp. 1077-1090, 2014.
- [31] Fastenal, "Screw Thread Design," Fastenal, March 2009. [Online]. Available: <https://www.fastenal.com/content/feds/pdf/2017/02/Screw%20Threads%20Article%20rev%202017-02-21.pdf>. [Accessed May 2020].

**APPENDIX A**

**ANALYTICAL VALIDATION OF SIMPLIFIED  
COMPONENTS**

## Coupler

### Estimation of Antenna First Mode

Relevant terminology is shown below in Figure A.0.1.

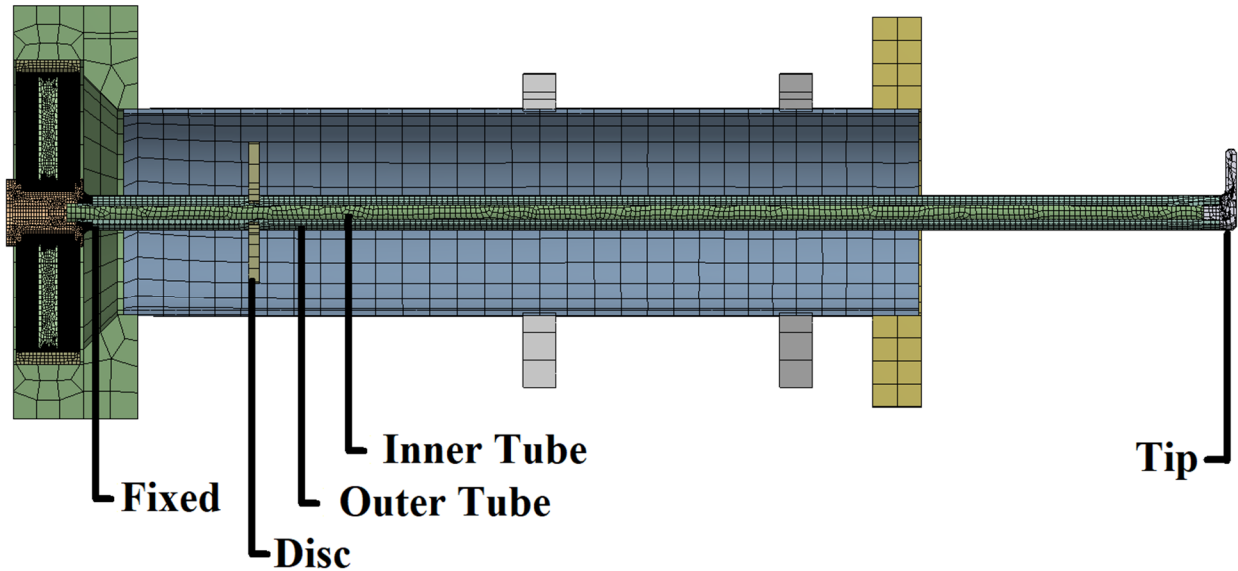


*Figure A.0.1: Coupler Antenna Terminology*

Assumptions:

- The antenna tip will have significantly more effect than the disc, and the mass of the disc can be neglected
- The stiffnesses of the inner and outer tube are additive
- The attachment to the copper connector is a fixed location

Governing equations for a cantilever beam with a fixed end and a point mass at one end [30]:

$$\text{Mass: } m_{eq} = \frac{33}{140} m_{beam} + m_{tip}$$

$$\text{Stiffness: } k = \frac{3EI}{l^3}$$

$$frequency_{natural} = \frac{\sqrt{\frac{k}{m}}}{2\pi}$$

Where E is Young's Modulus, I is the Area Moment of Inertia, and l is length.

Inner Tube:

Material: SS316L, E = 200 GPa

$$I = \frac{\pi(D^4 - d^4)}{64} = \frac{\pi((0.0123\text{mm})^4 - (0.0114\text{mm})^4)}{64} = 2.945 e - 10 m^4$$

Outer Tube:

Material: OFHC Copper, E= 117 GPa

$$I = \frac{\pi(D^4 - d^4)}{64} = \frac{\pi((0.0075\text{mm})^4 - (0.0066\text{mm})^4)}{64} = 6.217 e - 11 m^4$$

$$m_{eq} = \frac{33}{140}(m_{inner\ tube} + m_{outer\ tube}) + m_{tip}$$

$$m_{eq} = \frac{33}{140}(0.065\ kg + 0.125\ kg) + 0.021\ kg = 0.066\ kg$$

$$k_{eq} = k_{outer} + k_{inner}$$

$$k = \frac{3}{(0.413\ m)^3}(EI_{inner} + EI_{outer})$$

$$k = \frac{3}{(0.413\ m)^3} \left( \frac{200e9N}{m^2} * 2.945e - 10m^4 + \frac{117e9N}{m^2} * 6.217e - 11m^4 \right) = 2818.1\ N/m$$

$$f_n = \frac{\sqrt{\frac{2818.1\ N/m}{0.066\ kg}}}{2\pi} = 32.9\ Hz$$

## Cavity Supports Bolts

### Loading Conditions

- Each cavity with attached components past the needle block connection weighs 300 kg
- Two supports support each cavity. One accepts 70% of the cavity weight, the other 30%
- As bolts contacting the lugs/bearings are only held in contact by bolt tightness/gravity, during an acceleration, the bolts can only be loaded in compression
- For the bolts contacting the cavity lugs/bearings, pretension is considered to have a meaningful effect on the overall stress

### Lower Si-Brz M10 Bolts – 4X

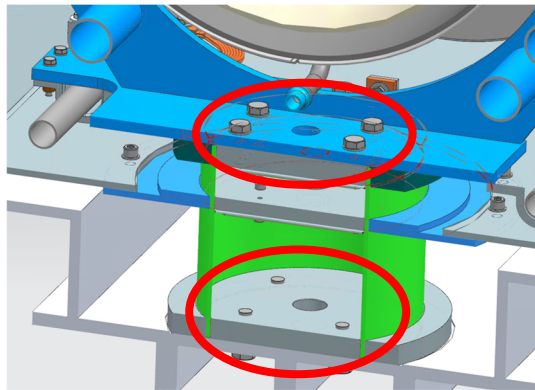


Figure A.0.2: Cavity Support M10 Bolts

Yield due to 5G:

$$\text{Si-Brz: } \sigma_{sy} = 370 \text{ Mpa} * 0.57 = 211 \text{ MPa}$$

$$A_{shear} = 52.3 \text{ mm}^2$$

$$\sigma_s = \frac{F}{A} = \frac{\left(300 \text{ Kg} * 5G * \frac{9.8066 \text{ m}}{\text{s}^2}\right) * 70\%}{4 \text{ bolts} * 52.3 \text{ mm}^2} = \frac{10,297 \text{ N}}{209.2 \text{ mm}^2} = 49.2 \text{ MPa}$$

$$\sigma_s \ll \sigma_{sy}, \text{ PASS}$$

### Lower Needle Support Bolts

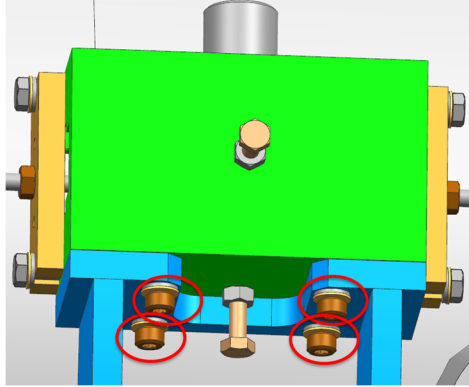


Figure A.0.3: Needle Block Lower Bolts

Yield due to 5G:

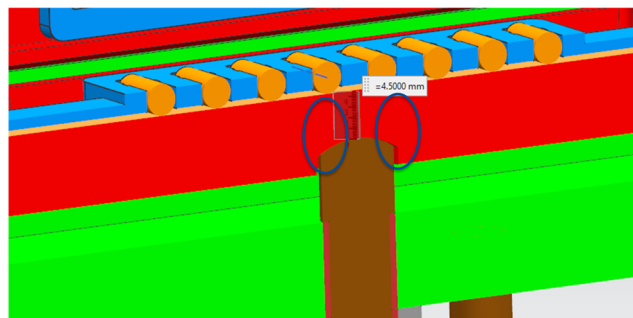
$$\text{Si-Brz: } \sigma_{sy} = 370 \text{ MPa} * 0.57 = 211 \text{ MPa}$$

$$A_{shear} = 17.9 \text{ mm}^2$$

$$\sigma_s = \frac{F}{A} = \frac{\left(300 \text{ Kg} * 5G * \frac{9.8066 \text{ m}}{\text{s}^2}\right) * 35\%}{4 \text{ bolts} * 17.9 \text{ mm}^2} = \frac{5,148 \text{ N}}{79.6 \text{ mm}^2} = 72 \text{ MPa}$$

$$\sigma_s \ll \sigma_{sy}, \text{ PASS}$$

### Bearing Shear



Approx. Shear Area Circled

Figure A.0.4: Needle Bearing Shear Area

Bolt Pretension:

Torque for spring jacks: 53 in-lbf

$$Torque = K * F_{axial} * D \mid F_{axial} = \frac{53 \text{ in} - \text{lbf}}{0.2 * 20 \text{ mm} * \frac{1 \text{ in}}{25.4 \text{ mm}}} = 336.5 \text{ lbf} = 1500 \text{ N}$$

Yield due to 3G:

$$\text{SS316L: } \sigma_{sy} = 205 \text{ Mpa} * 0.57 = 117 \text{ MPa}$$

$$A_{shear} = D * \pi * t = 6.77 \text{ mm} * \pi * 4.5 \text{ mm} = 95.7 \text{ mm}^2$$

$$\sigma_s = \frac{F}{A} = \frac{\left(300 \text{ Kg} * 3G * \frac{9.8066 \text{ m}}{\text{s}^2}\right) * 35\% + 1500 \text{ N Tight}}{95.7 \text{ mm}^2} = \frac{4,589 \text{ N}}{95.7 \text{ mm}^2} = 48 \text{ MPa}$$

$$\sigma_s \ll \sigma_{sy}, \text{ PASS}$$

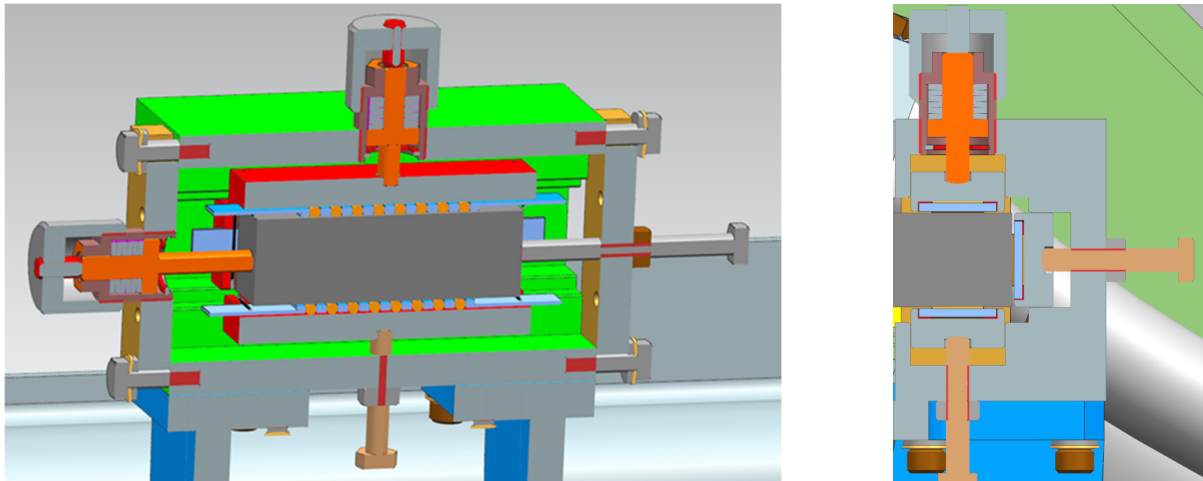
**Axial Loading**

Figure A.0.5: Needle Block Support | Left: Transverse Section View | Right: Axial Section View

Yield due to 5G: M6 Bolt

$$\text{SS316L: } \sigma_y = 205 \text{ Mpa}$$

$$A_{tensile} = 20.1 \text{ mm}^2$$

$$\sigma_t = \frac{F}{A} = \frac{\left(300\text{Kg} * 5\text{G} * \frac{9.8066\text{m}}{\text{s}^2}\right) * 35\% + 1500\text{N Tight}}{28.3\text{mm}^2} = \frac{6,648\text{N}}{20.1\text{mm}^2} = 331 \text{ MPa}$$

$$\sigma_s > \sigma_{sy}, \text{ FAIL}$$

Increase size to M10

$$\text{SS316L: } \sigma_y = 205\text{Mpa}$$

$$A_{tensile} = 58.0 \text{ mm}^2$$

$$\sigma_t = \frac{F}{A} = \frac{\left(300\text{Kg} * 5\text{G} * \frac{9.8066\text{m}}{\text{s}^2}\right) * 35\% + 1500\text{N Tight}}{58.0 \text{ mm}^2} = \frac{6,648\text{N}}{58.0\text{mm}^2} = 115 \text{ MPa}$$

$$\sigma_t \ll \sigma_y, \text{ PASS}$$

Spring jack with 8mm Barrel

$$\text{SS316L: } \sigma_y = 205\text{Mpa}$$

$$A_{tensile} = \pi r^2 = \pi * (3.8\text{mm})^2 = 45.4 \text{ mm}^2$$

$$\sigma_t = \frac{F}{A} = \frac{\left(300\text{Kg} * 5\text{G} * \frac{9.8066\text{m}}{\text{s}^2}\right) * 35\% + 1500\text{N Tight}}{45.4 \text{ mm}^2} = \frac{6,648\text{N}}{45.4\text{mm}^2} = 146 \text{ MPa}$$

$$\sigma_t \ll \sigma_y, \text{ PASS}$$

Stainless steel was retained as the material as it has a much lower thermal conductivity than Si-Brz, and the bolts act as a heat conductor to the 2K cavities. The design of the spring jack was adjusted to have a diameter of 7.6 mm, giving it a cross-sectional area similar to that of the M10

bolts. At this time, other bolt sizes were increased to M8, and the calculations are shown below to verify this sizing.

## Vertical and Transverse Loading

### M8 SS316L Bolts – Transverse and Vertical Directions

#### Maximum Load Determination

3G Load Including weight from gravity:

$$F = \frac{\left(300 \text{ kg} * 4G * \frac{9.8066m}{s^2}\right) * 70\%}{2 \text{ bolts}} = 4,118 \text{ N}$$

1.5G Load with only one side in compression:

$$F = \frac{\left(300 \text{ kg} * 1.5G * \frac{9.8066m}{s^2}\right) * 70\%}{1 \text{ bolt}} = 3,089 \text{ N}$$

$$\text{SS316L: } \sigma_y = 205 \text{ Mpa}$$

$$A_{tensile} = 36.6 \text{ mm}^2$$

$$\sigma_t = \frac{F}{A} = \frac{4,118 \text{ N} + 1500 \text{ N Tight}}{2 * 36.6 \text{ mm}^2} = 78 \text{ MPa}$$

$$\sigma_t \ll \sigma_y, \text{ PASS}$$

## Cavity Supports 1.5G Sliding

### Maximum Holding Force:

Spring Jack Torque Spec: 53 in-lbf , then loosen ¼ turn (assume full tightness)

$$Torque = K * F_{axial} * D \mid F_{axial} = \frac{53in - lbf}{0.2 * 20mm * \frac{1in}{25.4mm}} = 168.4 lbf$$

$$= 1500 N \text{ per Bolt}$$

There are four bolts in total. Both the needle bearings and contacted bolts are SS316L. The friction coefficient between SS316L and Ti-2 is not readily available after research and will be assumed as 0.20.

$$Total Normal Force = F_N = 1,500N * 4 bolts = 6,000 N$$

$$F_{Static Max} = F_n * \mu = 6,000N * 0.2 = 1,200 N$$

### Maximum Expected Load:

$$Applied Force = F = \frac{300 kg * 1.5G * \frac{9.8066m}{s^2} * 70\%}{2 Sides} = 1,550 N < F_{Static Max}$$

## Thermal Shield

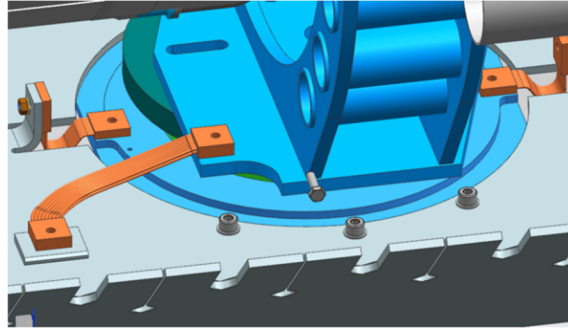


Figure A.0.6: Original Thermal Shield Design

Assumptions:

- Only movement can be in axial direction due to a 5G load
- The bolts evenly accept the load, and no load is supported by friction due to the weight of the shield- only the clamping force of the bolts

Yield due to 5G:

$$\text{SS316L: } \sigma_{sy} = 205 \text{ Mpa} * 0.57 = 117 \text{ MPa}$$

$$A_{shear} = 32.8 \text{ mm}^2$$

$$\sigma_s = \frac{F}{A} = \frac{\left(600 \text{ Kg} * 5G * \frac{9.8066 \text{ m}}{\text{s}^2}\right)}{6 \text{ bolts} * 32.8 \text{ mm}^2} = \frac{29,420 \text{ N}}{196.8 \text{ mm}^2} = 149.5 \text{ MPa}$$

$$\sigma_s \gg \sigma_{sy}, \text{ FAIL}$$

Slip due to 5G:

$$\text{SS316L: } \sigma_y = 205 \text{ MPa}$$

$$A_{min} = 32.8 \text{ mm}^2$$

If bolts tightened to 75%  $\sigma_y$ ,  $F_{normal} = 32.8 \text{ mm}^2 * 205 \text{ MPa} * 0.75 = 5,043 \text{ N per bolt}$

$$\text{Safety Factor: } F_N = \frac{5043N}{2} = 2,021 N$$

$$F_{Normal} = 6 \text{ bolts} * 2,021N = 12,126 N$$

$\mu = 1.05$  – clean and dry aluminum – aluminum (greasy is 0.3)

$$F_{friction} = \mu * F_N = 1.05 * 12,126 N = 12,732 N$$

$$\text{Divide by unit G force: } \frac{12,732 N}{\frac{9.8066m}{s^2} * 600Kg} = 2.16G \text{ to cause slip} \ll 5G$$

New design validation:

New bolt configuration: 8 x M12 SS316

Yielding:

$$A_{shear} = 76.3 \text{ mm}^2$$

$$\sigma_s = \frac{F}{A} = \frac{29,420N}{610.4 \text{ mm}^2} = 48.2 \text{ MPa}$$

$$\sigma_s \ll \sigma_{sy}, \text{ PASS}$$

Sliding:

$$A_{min} = 76.3 \text{ mm}^2$$

If bolts tightened to 75%  $\sigma_y$ ,  $F_{normal} = 76.3 \text{ mm}^2 * 205 \text{ MPa} * 0.75 = 11,731N \text{ per bolt}$

$$\text{Safety Factor: } F_N = \frac{11,731N}{2} = 5,835 N$$

$$F_{Normal} = 8 \text{ bolts} * 5,835N = 46,680 N$$

## Strongback Supports

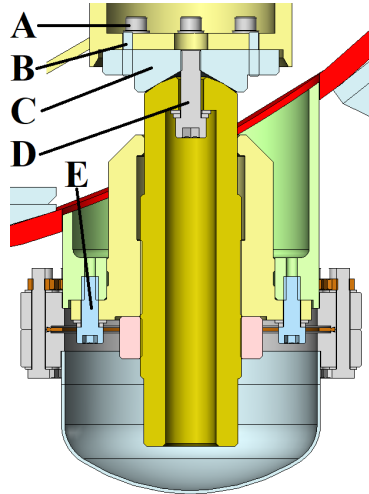


Figure A.0.7: Strongback Support Connections

Load per support = 400 kg = 4 kN @ 1G

**Connection A: 6x M8 Si-Brz Bolts**

5G Axial Acceleration:

1.5G not evaluated since loading conditions are same as 5G with lower magnitude.

Check for yielding due to shear forces:

$$F = 20 \text{ kN along shear plane} \quad A_{\text{shear}} = 32.8 \text{ mm}^2 * 6 \text{ bolts} = 196.8 \text{ mm}^2$$

$$\tau_{\text{allowable}} = 370 \text{ MPa (YS)} * 0.57 = 211 \text{ MPa}$$

$$\tau = \frac{F}{A} = 101.6 \text{ MPa} : \text{PASS}$$

Check for holding friction for slip:

$$\text{Clamping Force per bolt} = F_{\text{clamp}} = \frac{T}{KD} = \frac{14.1 \text{ N} \cdot \text{m}}{0.2 * 0.008\text{m}} = 8800 \text{ N}$$

$$F_{\text{Static Max}} = F_N * \mu \quad \mu \text{ unknown for SS316 - Si - Brz, assume 0.2 conservatively}$$

$$F_{\text{Static Max}} = 8,800 \text{ N} * 6 \text{ bolts} * 0.2 = 10,560 \text{ N} \ll 20 \text{ kN} : \text{FAIL}$$

Sliding possible, could affect alignment. Unable to increase bolt size, so the dowel pins will be used to prevent movement.

3G Vertical Acceleration:

$$F_{\text{Tensile Max}} = \text{Accel Load} + \text{Tightness Load} = \frac{400 \text{ kg} * 2G}{6 \text{ bolts}} + 8800 \text{ N} = 1,140 \frac{\text{N}}{\text{bolt}}$$

$$A_{\text{Tensile}} = 36.6 \text{ mm}^2 \quad \sigma_{\text{YS}} = 370 \text{ MPa} \quad \sigma = \frac{F}{A} = 277 \text{ MPa} : \text{PASS}$$

**Connection B: 2x 6mm SS 18-8 Dowel Pins**

5G Axial Acceleration:

Check for yielding due to shear forces:

$$F = 20 \text{ kN along shear plane} \quad A_{\text{Shear}} = \pi r^2 = \pi * (3\text{mm})^2 * 2 \text{ pins} = 56.5 \text{ mm}^2$$

$$\tau_{\text{allowable}} = 215 \text{ MPa (YS)} * 0.57 = 123 \text{ MPa}$$

$$\tau = \frac{F}{A} = 354 \text{ MPa} \gg 123 \text{ MPa} : \text{FAIL}$$

Modify Design: use 8mm pins with 52100 Alloy Steel

$$F = 20 \text{ kN along shear plane} \quad A_{Shear} = \pi r^2 = \pi * (4\text{mm})^2 * 2 \text{ pins} = 100.5 \text{ mm}^2$$

$$\tau_{allowable} = 413 \text{ MPa (YS)} * 0.57 = 235 \text{ MPa}$$

$$\tau = \frac{F}{A} = 199 \text{ MP} < 235 \text{ MPa} : \text{PASS}$$

### Connection C: SS304 Cone Plate

#### 3G Vertical Acceleration:

Other loads not considered as spherical connection carries shearing forces.

$$F_{Tensile \text{ Max}} = \text{Accel Load} + \text{Tightness Load} = 400 \text{ kg} * 2G + 1.5 * (F_{Accel}) = 20 \text{ kN}$$

Due to the high strength bolt, failure will occur in the internal thread first. The bolt should not be torque to spec, as this assumes similar materials. The recommended tightness is 1.5x the maximum applied separation force to ensure contact and therefore alignment is maintained.

$$A_{Shear} = 26.1 \frac{\text{mm}^2}{\text{mm thread}} \quad \sigma_{YS} = 215 \text{ MPa} \quad \tau_{allowable} = 215 \text{ MPa} * 0.57 = 123 \text{ MPa}$$

The load on internal threads is not evenly distributed, and the first thread will accept the most load. If the first thread yields, then subsequent threads will also yield. According to Fastenal®, the first thread accepts 34% of the tensile load [31].

$$A_{Shear} = 26.1 \frac{\text{mm}^2}{\text{mm thread}} * 1.75\text{mm pitch} = 45.7 \text{ mm}^2$$

$$\tau = \frac{F}{A} = \frac{20,000\text{N} * 0.34}{45.7\text{mm}^2} = 149 \text{ MPa} > 123 \text{ MPa} : \text{FAIL}$$

Material adjusted to Si-Brz to increase the yield strength.

$$\tau = 149 \text{ MPa} < 211 \text{ MPa}$$

**Connection D: 1x 12.9 M12 Bolt**

$$A_{Shear} = 19.0 \frac{mm^2}{mm \text{ thread}} * 1.75mm \text{ pitch} = 33.2 mm^2$$

$$\tau = \frac{F}{A} = \frac{20,000N * 0.34}{33.2mm^2} = 205 MPa < 502 MPa (Ssy) : PASS$$

**Connection E: 6x M10 Si-Brz Bolts**3G Vertical Acceleration:

1.5G and 5G are not evaluated due to the tight fitment of the stud within the housing preventing any significant transverse/axial movement.

$$F_{Tensile Max} = Accel Load + Tightness Load = \frac{400 kg * 4G + 1.5 * (F_{Accel})}{6 bolts} = 6.7 kN$$

$$A_{Tensile} = 58.0 mm^2 \quad \sigma_{YS} = 370 MPa \quad \sigma = \frac{F}{A} = 116 MPa : PASS$$

## 1.5G Cavity Support Sliding Estimation

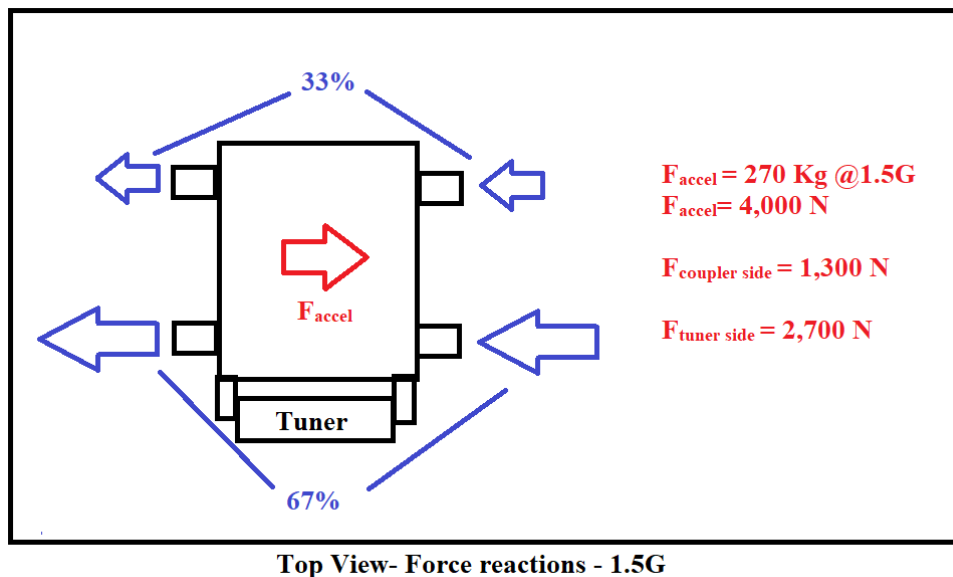


Figure B.0.8: Load Sharing Between Needle Supports

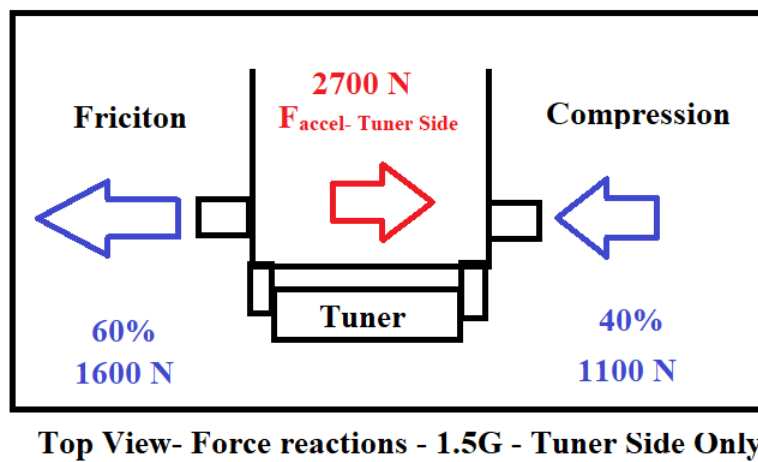
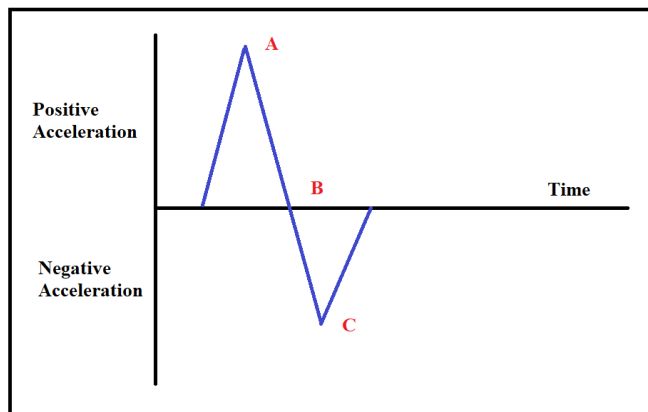
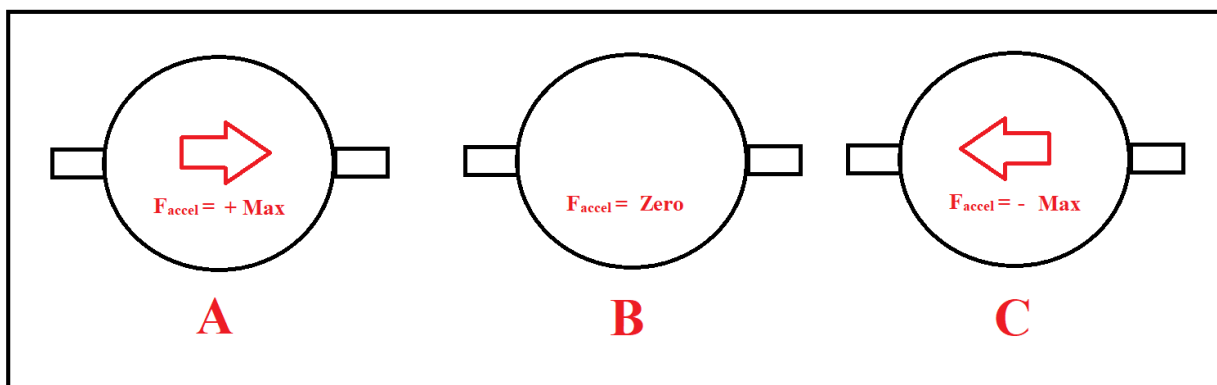


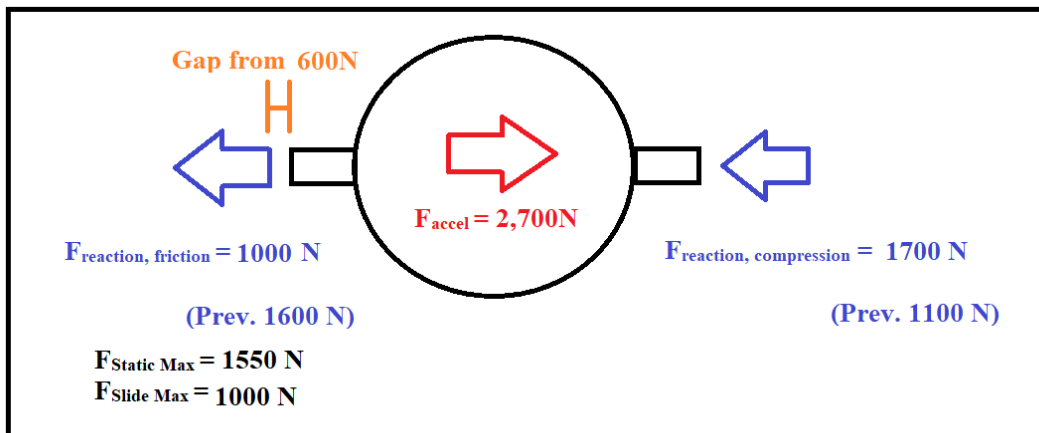
Figure B.0.9: Load Sharing of Tuner Side



*Figure B.0.10: Hypothetical Acceleration Event*

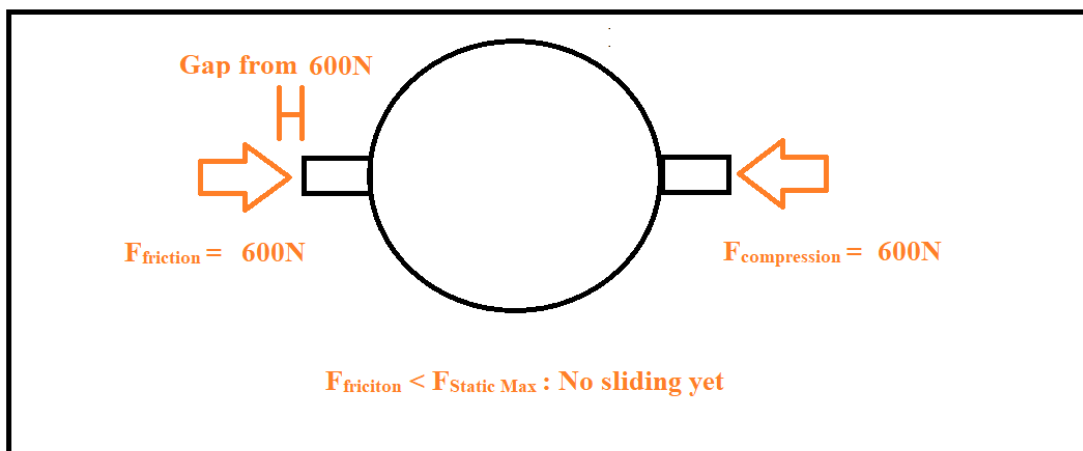


*Figure B.0.11: Free Body Diagrams During Acceleration Event*



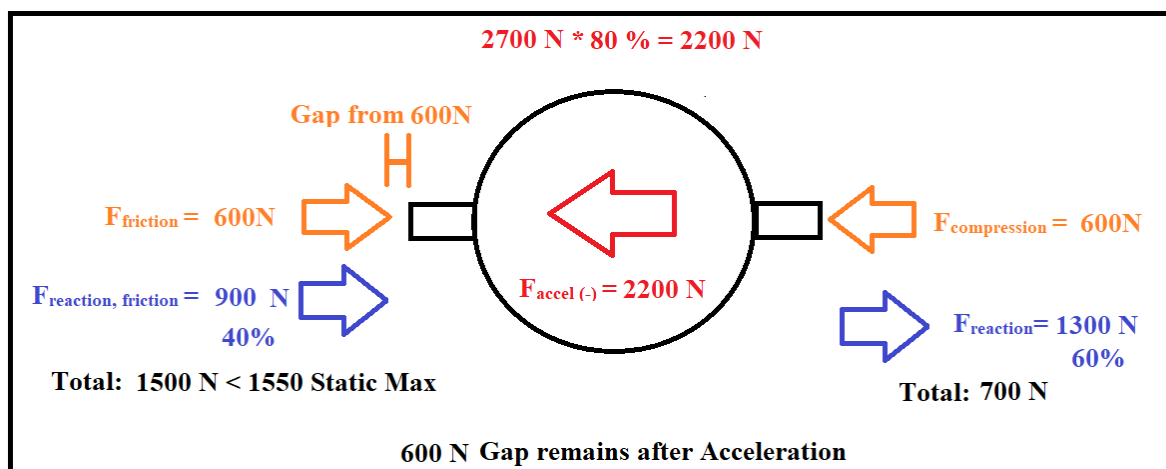
Equilibrium for +1.5G Accel

Figure B.0.12: Free Body Diagram Event A



Equilibrium between (+) and (-) Accel

Figure B.0.13: Free Body Diagram Event B



Forces during (-) Accel

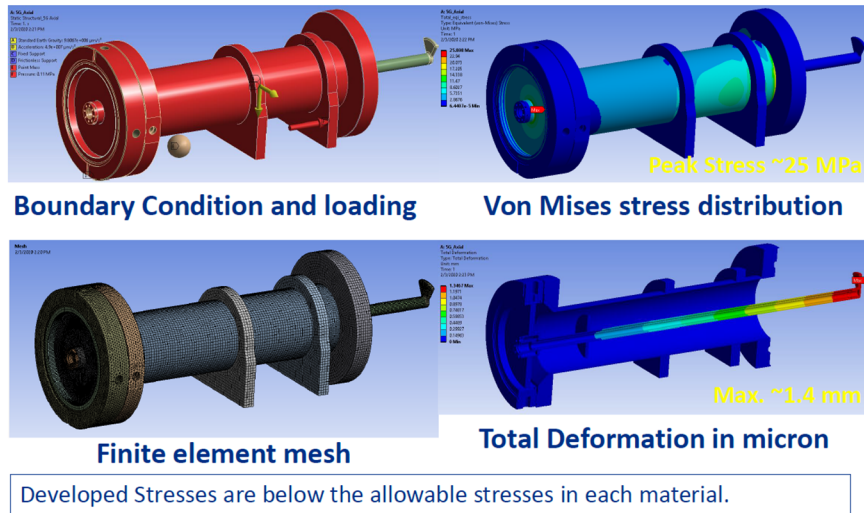
*Figure B.14: Free Body Diagram Event C*

**APPENDIX B**

**PREVIOUS ANALYSIS FOR REFERENCE AND  
COMPARISON**

# Coupler

## 650 MHz Coupler inside CM Transportation Analysis 5G along cavity axis

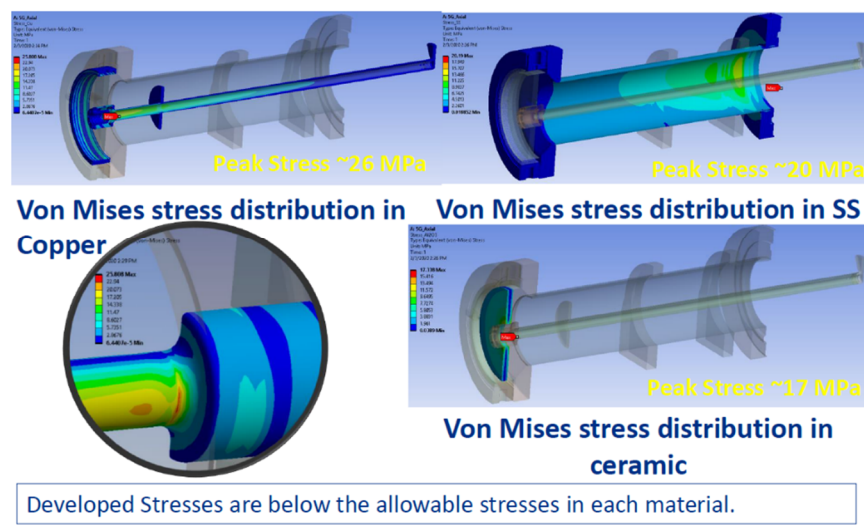


17 4-Oct-20 Nitin Nigam | 650 MHz Coupler Proto-FDR/PRR



Figure B.0.1: Coupler Previous Analysis Model and 5G Deformaiton [24]

## 650 MHz Coupler inside CM Transportation Analysis 5G along cavity axis

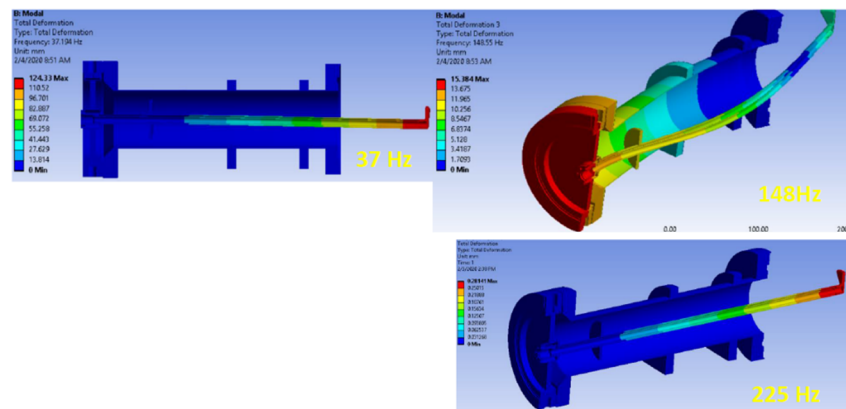


18 4-Oct-20 Nitin Nigam | 650 MHz Coupler Proto-FDR/PRR



Figure B.0.2 Coupler Previous Analysis 5G Stress Results [24]

## 650 MHz Coupler inside CM Modal Analysis with Cavity flange fixed



First Modal frequency is above 20 Hz and below 60 Hz

Figure B.0.3 Coupler Previous Analysis Mode Shapes [24]

Comparison: Results are nearly identical to analysis presented in report.

## B90 Cavity

### Analysis of dressed cavity for transport loading

A simulation was also performed for dressed cavity regarding transportation. Simulation was performed for 1 g load in all three directions (X, Y & Z) and maximum developed stresses were tabulated for cavity & bellows in each case. These simulations were performed for cavity with 40 kN/mm tuner stiffness. Similar analysis was also performed for cavity with safety bracket (without tuner stiffness) & results have been tabulated in table 12. The allowable stress for niobium in weld area is 15 MPa, based on the this & table 12 the dressed cavity is safe for acceleration up to 6 g.

Table 12: - Transportation loading results summary

Gravity loading direction	Maximum stress developed in cavity (MPa)		Maximum stress developed in bellows (MPa)	
	With tuner	With safety bracket	With tuner	With safety bracket
X (lateral)	2.4	2.4	7.9	12.2
Y (axial to cavity)	2.3	2.6	4.4	3.0
Z (along gravity)	2.4	2.4	7.9	12.2

Figure B.0.4: B90 Previous Analysis Results [25]

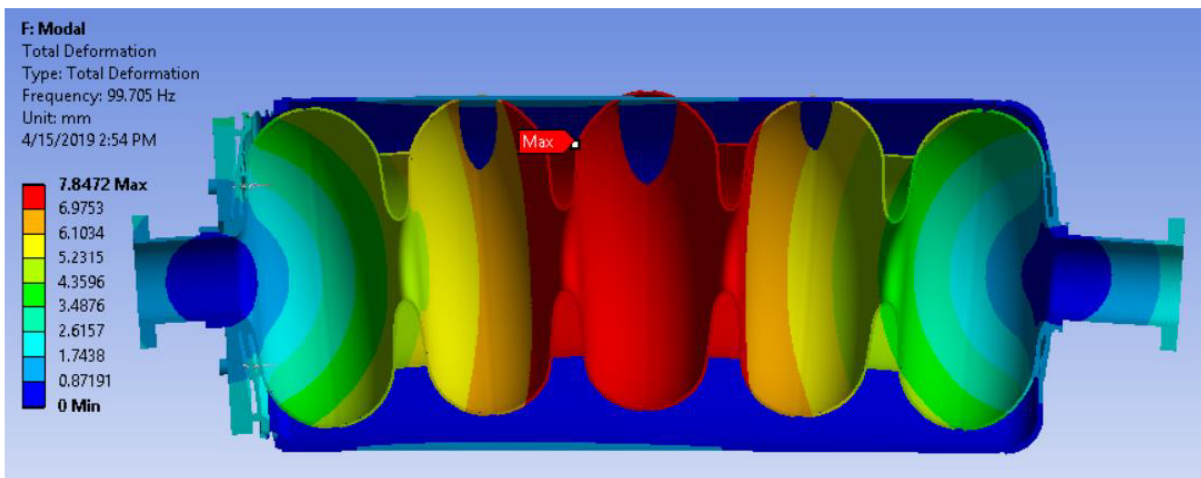
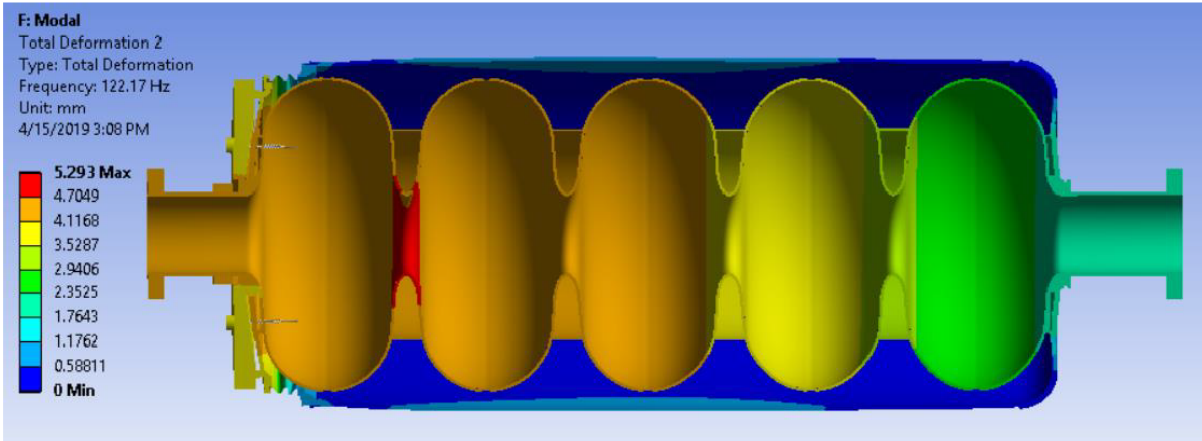


Figure 28 First mechanical mode of vibration (Bending mode)

Figure B.0.5: B90 Previous Analysis First Mode [25]



**Figure 29 Second mechanical mode of vibration (Axial mode)**

*Figure B.0.6: B90 Previous Analysis Second Mode [25]*

Comparison: Transverse mode of 100 Hz varies from 74 Hz in this report due to use of symmetric model in previous analysis. Axial mode of 122 Hz comparable to 123 Hz of this report. Structural results vary since the analysis of this report included the weight from the tuner, where previously only the axial stiffness was included.

## B92 Cavity

### Gravity Loading '3g' – Stress Plot



Figure B.0.7: B92 Previous Analysis 3G Stress [26]

### Gravity Loading '3g' – Deformation Plot

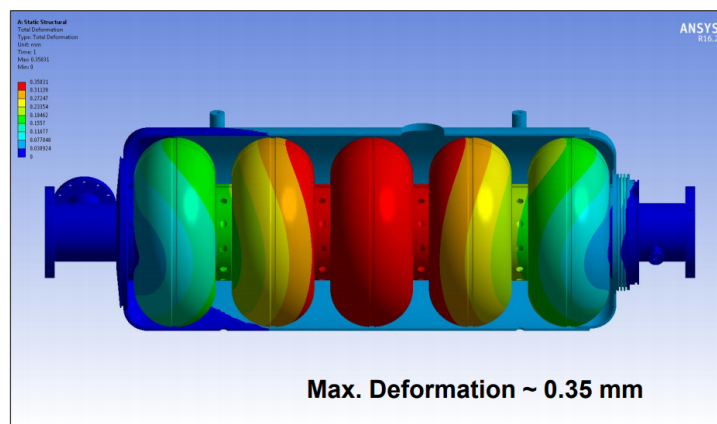
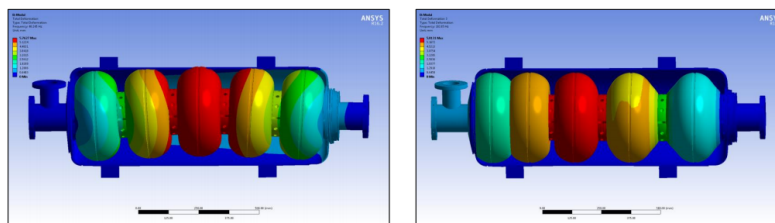


Figure B.0.8: B92 Previous Analysis 3G Deformation [26]

## Modal Analysis



First Mode Shape Frequency ~ 48 Hz  
(Transverse Mode)

Second Mode Shape Frequency ~ 103 Hz  
(Longitudinal Mode)

Longitudinal modes will result higher frequency detuning than transverse modes.



45

Navneet Kumar Sharma | Cavity Design

2/1/2019



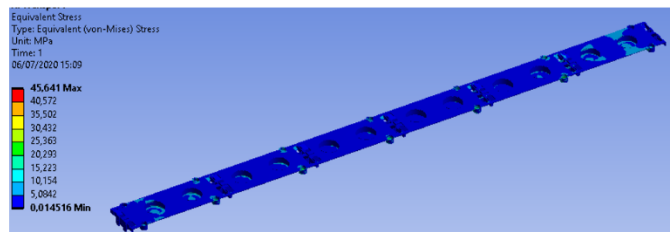
*Figure B.0.9: B92 Previous Analysis Modal Results [26]*

Comparison: Transverse mode of 48 Hz comparable to 50 Hz of this report, and likewise axial 103 Hz is comparable to 111 Hz. The deformation for 3G was compared to the model created, and the deformation matched within 10%. Stresses are lower in previous analysis, likely due to not including mass from the tuner which must be supported by the cavity jacket.

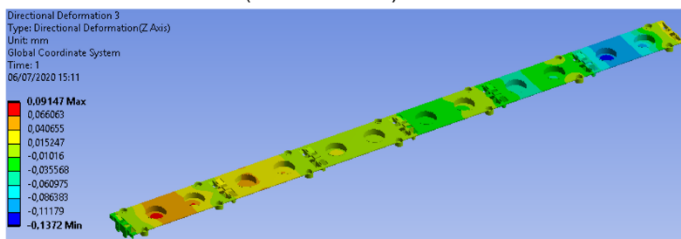
# Strongback

cea **5-STRONGBACK DURING TRANSPORTATION** PIP-II

- Transport: Axial 5g
  - Stress < 50 MPa < 150 MPa max admitted (316L yield strength = 190 MPa)



- Deformation < 0.23 mm (Delta=max-min)

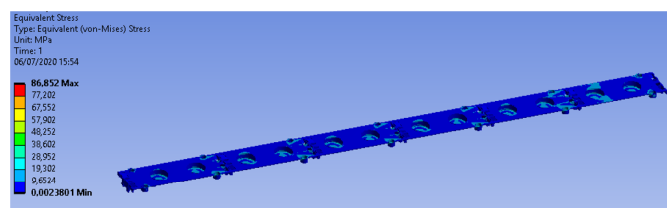


HB650 FDR 30 July 2020 Slide 19

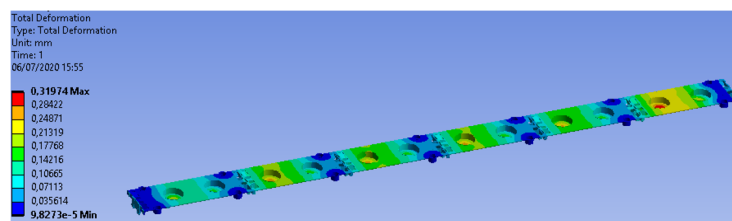
Figure B.0.10: Strongback Previous Analysis 5G Results [28]

cea **5-STRONGBACK DURING TRANSPORTATION** PIP-II

- Transport: Vertical 3g
  - Stress < 87 Mpa < 150 MPa max admitted (316L yield strength = 190 MPa)



- Deformation < 0.32 mm



HB650 FDR 30 July 2020 Slide 29

Figure B.0.11: Strongback Previous Analysis 3G Results [28]

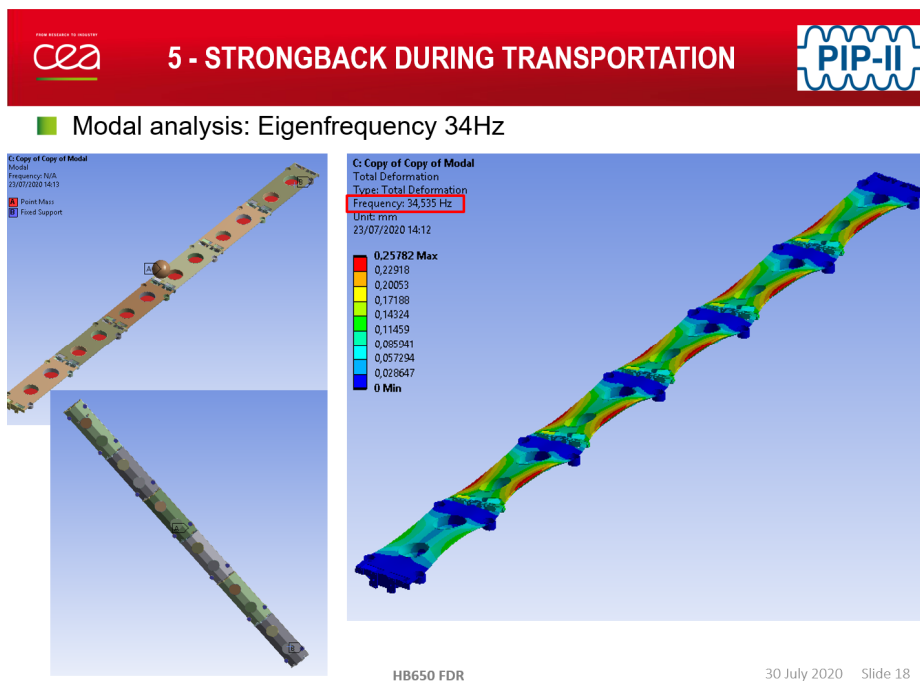
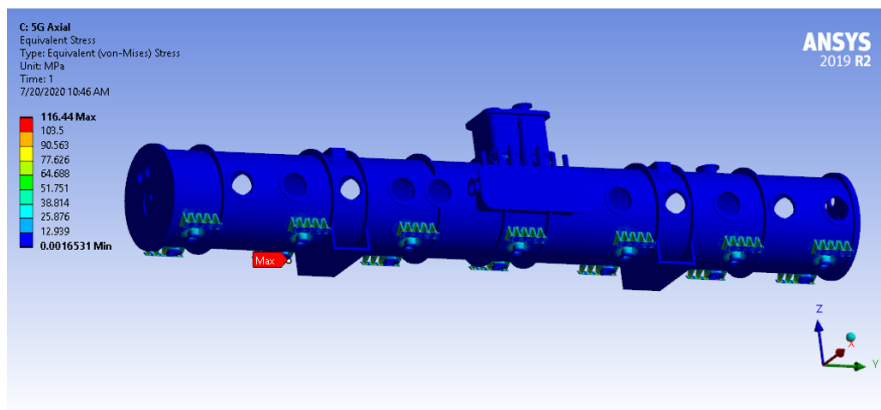


Figure B.0.12: Strongback Previous Analysis Modal Results [28]

Comparison: Deformation and mode frequencies are comparable to the analysis performed for this report. A noted difference: the deformation for the 1.5G/3G/5G load cases is near identical, only if the effects of gravity are neglected. Including gravity does not significantly affect stress or displacement, and so this difference can be largely ignored.

## Vessel

### Equivalent stress – 5G axial

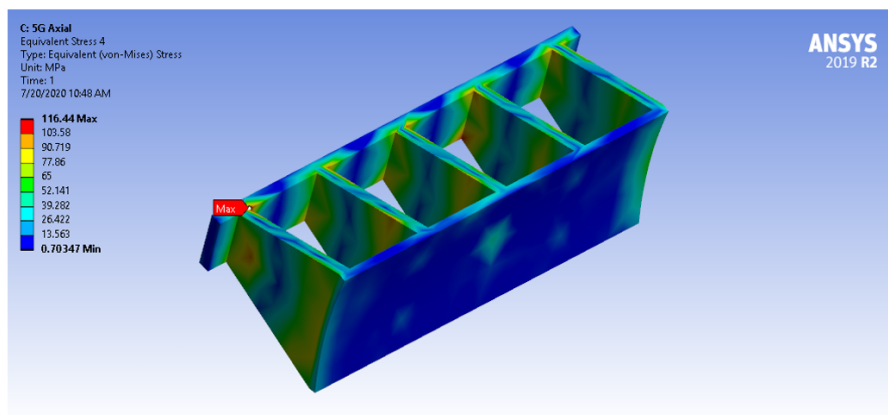


46 29 & 30 July 2020 M. Chen | 650 MHz High Beta CM Prototype FDR



Figure B.0.13: Vessel Previous Analysis 5G Stress [29]

### Equivalent stress on Mount plate – 5G axial



47 29 & 30 July 2020 M. Chen | 650 MHz High Beta CM Prototype FDR



Figure B.0.14: Vessel Previous Analysis 5G Stress Mount [29]

Comparison: Overall deformation and stresses are similar. Initial results showed different stresses at the transport supports during 5G. Further discussion with Meiyu clarified the issue and the converged results were deemed satisfactory per the requirements.